UC Santa Barbara
UC Santa Barbara Electronic Theses and Dissertations

Title

First-principles study of layered transition-metal oxides and sulfides for battery applications

Permalink

https://escholarship.org/uc/item/3c74172h

Author

Vinckeviciute, Julija

Publication Date

2020

Peer reviewed|Thesis/dissertation

University of California
Santa Barbara

First-principles study of layered transition-metal oxides and sulfides for battery applications

A dissertation submitted in partial satisfaction
of the requirements for the degree

Doctor of Philosophy

in

Materials

by

Julija Vinckevičiūtė

Committee in charge:

Professor Anton Van der Ven, Chair
Professor Samantha Daly
Professor Ram Seshadri
Professor Stephen Wilson

June 2020

The Dissertation of Julija Vinckevičiūtė is approved.

_____

Professor Samantha Daly

_____

Professor Ram Seshadri

_____

Professor Stephen Wilson

_____

Professor Anton Van der Ven, Committee Chair

June 2020

First-principles study of layered transition-metal oxides and sulfides for battery applications

Acknowledgements

A countless number of people have contributed to bringing me where I am today. I would be remiss if I did not mention at least a few of the colleagues, friends, and family members who guided and supported me along the way.

I will start at the beginning of my Materials journey–Northwestern University. If it were not for Slivka Residential College, it may have taken me many more years to learn of the existence of the study of Materials and to decide on that academic route. Tim Flavin and Raj Kumar, thank you for introducing me to MSE and for all the late nights working through homework and projects together. Thank you to the professors and mentors at NU who provided me with a solid foundation of materials theory, and thank you especially to Prof. Chris Wolverton and his lab for giving me the opportunity to grow and explore in a research setting.

After Northwestern, I joined the Materials Department at University of California, Santa Barbara. Thank you to my labmates for all the academic discussions and "coffee-talk" over the years. I cannot begin to express how thankful I am to Max Radin and Daniil Kitchaev for going above and beyond as mentors and collaborators; they have played an immense part in shaping the researcher I am today. Thank you to my experimental collaborators, especially Molleigh Preefer, Zachary Lebens-Higgins, and Nicholas Faenza, who brought a taste of reality to my theoretical work. Thank you, Prof. Anton Van der Ven, for being an exceptional teacher and advisor these past six years, instilling in me that we must always think critically about what is presented to us.

It has been an immense privilege to be a part of the UCSB academic community. Thank you to all the professors in the Materials Department for bringing world-class education to UCSB, which has allowed me to become a well-trained scientist while living in paradise. Thank you to my committee members for bringing new questions and

<h1 align="center">Curriculum Vitæ</h1>
<p align="center">Julija Vinckevičiūtė</p>

Education

2020	Ph.D. Materials, University of California, Santa Barbara, Santa Barbara, CA.
2014	B.S. Materials Science and Engineering & B.S. Environmental Engineering, Northwestern University, Evanston, IL.

Select publications

2019	M. D. Radin, **J. Vinckeviciute**, R. Seshadri, and A. Van der Ven, "Manganese oxidation as the origin of the anomalous capacity of Mn-containing Li-excess cathode materials," *Nat. Energy* **4** (2019) 639–646.
2019	**J. Vinckeviciute**, M. D. Radin, N. V. Faenza, G. G. Amatucci, and A. Van der Ven, "Fundamental insights about interlayer cation migration in Li-ion electrodes at high states of charge," *J. Mater. Chem. A* **7** (2017) 11996–12007.
2017	M. D. Radin, S. Hy, M. Sina, C. Fang, H. Liu, **J. Vinckeviciute**, M. Zhang, M. S. Whittingham, Y. S. Meng, and A. Van der Ven, "Narrowing the gap between theoretical and practical capacities in Li-ion layered oxide cathode materials," *Adv. Energy Mater.* **7** (2017) 1602888.
2016	**J. Vinckeviciute**, M. D. Radin, and A. Van der Ven, "Stacking-sequence changes and Na ordering in layered intercalation materials," *Chem. Mater.* **28** (2016) 8640–8650.

Select presentations

2019	**J. Vinckeviciute**, M. Radin, and A. Van der Ven, "Suppression of interlayer atom migration in layered transition-metal oxides," Materials Research Society Spring Meeting and Exhibit, Phoenix, AZ.
2019	**J. Vinckeviciute**, M. Radin, and A. Van der Ven, "Electronic structure implications for atom migration in layered cathode materials," Materials Research Outreach Program Symposium, Santa Barbara, CA.
2018	**J. Vinckeviciute**, M. Radin, J. Kaufman, M. Toriyama, and A. Van der Ven, "Unraveling phase transformation mechanisms in ceramic electrode materials of Li, Na, and K batteries," Materials

	Science & Technology Technical Meeting and Exhibition, Columbus, OH.
2018	**J. Vinckeviciute**, M. Radin, and A. Van der Ven, "Role of transition metal identity in suppression of interlayer migration in layered cathode materials," 233rd Meeting of the Electrochemical Society, Seattle, WA.
2016	**J. Vinckeviciute**, M. Radin, and A. Van der Ven, "Stacking-sequence changes and ordering in intercalating materials exhibiting O1, O3, and P3 hosts," Materials Research Society Fall Meeting and Exhibit, Boston, MA.

Abstract

First-principles study of layered transition-metal oxides and sulfides for battery
applications

by

Julija Vinckevičiūtė

Renewable energy sources are generally abundant but intermittent, with peak pro-
duction and peak demand occurring at different times. Therefore, storage and controlled
distribution of energy is an important component of the shift away from on-demand fuels
like petroleum and natural gas. Secondary electrochemical batteries are one convenient
method for closing the gap between energy supply and demand. Battery performance
and cost are largely restricted by the materials, especially those used for the electrodes.
Part of the problem is material instability upon cycling. As the battery is charged (and
discharged), the composition of the electrode changes, often resulting in reversible and
irreversible phase transitions which result in material degradation. Therefore, battery
capacity and lifetime can be limited by thermodynamic instabilities. We employ first-
principles methods like density functional theory and Monte Carlo to study phase stability
in layered electrode materials. We look at stacking-sequence changes, ion ordering, and
atom migration to better understand bulk degradation mechanisms in Li- and Na-ion
materials. We use Na_xTiS_2, Na_xTiO_2, and Li_xMO_2 (M = Co, Ni, Mn) as model systems
to explore phenomena present in a variety of layered transition-metal oxides and sulfides.
Our work aids in interpreting experimental observations and in generating design rules
for more robust electrode materials.

Contents

Chapter 1

Introduction

1.1 From global climate to quantum mechanics

Each year, the Oxford Dictionary chooses a word or expression to reflect the mood and preoccupations of the public in that year. In 2019, that expression was "climate emergency". Changing precipitation patterns have resulted in more frequent and intense storms, droughts, floods, and fires [1, 2]. The ocean is warming and acidifying [3], and biodiversity is threatened by rapid changes in environment [4]. Everything points toward anthropogenic climate change largely caused by greenhouse gas emissions from energy produced via combustion of fossil fuels [5] and amplified by massive deforestation [6,7]. A move away from fossil fuels toward renewable resources for energy production is necessary to curb further greenhouse gas accumulation in the atmosphere.

Renewable energy sources like sunlight, wind, and tides are generally quite abundant, and current technology is sufficient to harness it [8]. However, these sources are intermittent: sun only shines on clear days, wind blows harder during certain seasons, and tides are dependent on the moon's cycle. Moreover, renewable energy supply and electricity demand are often not in sync [9]. Therefore, storage and controlled distribution of energy
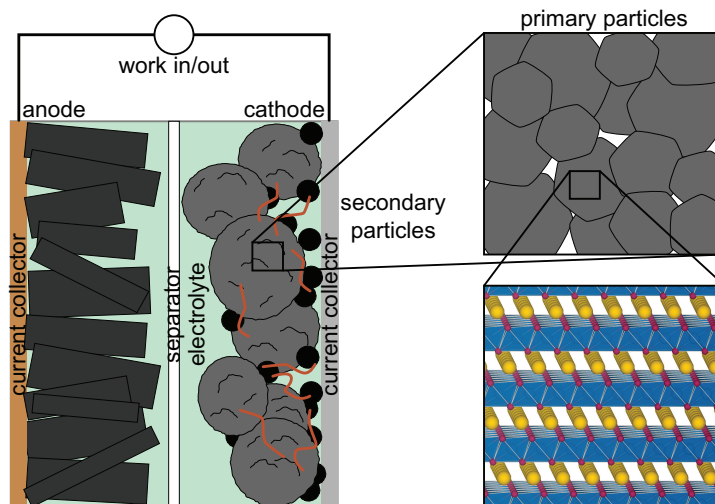
Figure 1.1: Schematic of a battery with graphitic anode and transition-metal (M) oxide cathode. Besides the layered M-oxide, the cathode also contains binders and carbon to promote conductivity. The secondary particles of the M-oxide are made up of primary crystals with a layered structure for ion intercalation. Portion of image made using VESTA software [10].

are an important component of the shift away from on-demand fuels like petroleum and natural gas. Secondary electrochemical batteries are one convenient method for closing the gap between energy supply and demand.

Let us begin with a very brief overview of how a secondary (i.e. rechargeable) battery functions. A schematic of a typical battery is illustrated in Fig. 1.1. Batteries consist of two electrodes, a cathode and an anode, and an electrolyte that conducts ions between the electrodes but is electrically insulating. The separator ensures that the anode and cathode do not interact inside the battery. As ions are shuttled from one electrode to the other, electrons must travel across the external circuit to maintain electroneutrality in the system. This provides a current at a certain potential that results in work.

We focus on batteries that utilize layered transition-metal oxides or sulfides as one or both of the electrode materials. There are many important criteria to consider when designing these batteries, some of which include:

Capacity Number of electrons that can be shuttled between the electrodes per unit

volume or unit mass. Determines amount of energy stored in a battery.

Voltage Electromotive force delivered by each electron. Alongside capacity, determines the amount of energy a battery can store.

Rate The amount of time to shuttle ions from one electrode to the other. Determines how quickly a battery can be charged and discharged, with high rates enabling fast charging and large power usage.

Stability Resistance to change of materials during battery cycling. Material degradation can reduce reversible capacity, decrease voltage window, and shorten battery lifetime.

Safety Likelihood of side reactions that can lead to short-circuiting and catastrophic failure.

Cost Consider price of materials and manufacturing, amount of energy stored, and longevity.

The ideal battery would optimize each of these (and other) properties to deliver the most cost-effective and convenient energy storage solution. However, despite decades of research since the first commercialized Li-ion battery in 1991, some studies report that overproducing energy to meet peak demand at the cost of wasted resources is more economical than installing sufficient storage [9]. Undoubtedly, there remains plenty of room for improvement in each of the categories listed above.

One of the challenges of studying batteries is their hierarchical structure, as illustrated in Fig. 1.1. The size of most batteries is on the scale of centimeters. The secondary particles that make up the cathode are often on the order of microns. Each secondary particle consists of primary particles on the order of hundreds of nanometers. These

primary particles are layered structures of transition metals, anions, and shuttling cations, with interlayer distances of a few angstrom. Effects at the various length scales can be difficult to disentangle and identify experimentally, which is where theoretical calculations can hold an advantage. Many properties of a full battery cell are limited by the bulk electrode material at the atomic scale. Therefore, we employ methods that rely on quantum mechanics to understand how bulk material properties change during charge and to then propose design principles for improving batteries.

1.2   Overview

The sections that follow detail first-principles studies of layered transition-metal oxides and sulfides for Li- and Na-ion applications. [1] Conclusions from each study mirror the unique chemistries of the materials and show that a fundamental understanding of electrodes can elucidate macroscopic observations.

We begin with a comprehensive overview of electrode properties and functionality followed by a description of the methods used throughout the remainder of the text. These chapters should provide the tools for interpreting the work that follows.

Our first study is inspired by TiS_2, one of the first reported battery intercalation compounds [11]. While this material was initially intercalated with Li, we study its Na analogue: Na_xTiS_2. One of the most striking differences between the two systems

---

is the formation of a specific stacking of the transition-metal layers called P3 in the Na compound. We show that the P3 phase is stable at intermediate compositions and analyze the distinct devil's staircase series of orderings of Na atoms. We suggest that the ordering could have significant effects on atom diffusion.

Next, we turn to the oxide of the above chemistry. Unlike most Na-ion layered materials, Na_xTiO_2 does not appear to stabilize the P3 stacking. Instead, the material retains the O3 stacking sequence that it is synthesized in over the first half of Na deintercalation. We discover an unexpected sequence of Na orderings which may explain the experimentally observed phase transition reported in literature.

Lastly, we turn to model systems of state-of-the-art Li-ion cathode materials with transition metals Co, Mn, and Ni. We seek to determine material behavior at high states of charge (when most of the Li has been removed) to provide design principles for increasing cathode capacity. We show that electronic structure is instrumental in understanding the difference between various transition metals in their role as hosts and speculate that certain elements may impede interlayer cation migration and thus reduce irreversible capacity loss.

These detailed studies reveal some of the capabilities of first-principles calculations and how they can be used to better understand and improve battery performance. The conclusions set forth by this work will aid in furthering the field toward the next generation of battery materials.

Chapter 2

Electrode structure and chemistry

2.1 Layered stacking

Layered transition-metal oxides and sulfides have A_xMX_2 stoichiometry, where A is the intercalating ion species with composition x, M is a transition-metal (for this work, first row $3d$ metal), and X represents sulfur or oxygen anions. The structure is made up of layers of two-dimensional, close-packed triangular lattices occupied by A, M, or X ions, as shown in Fig. 2.1. The sandwich of X-M-X layers are always offset from each other in an A-B-C type stacking, forming a sheet of edge-sharing M-X octahedra. The interlayer spacing between the octahedral MX_2 sheets allows for A intercalation.

Using the notation of Delmas [12], the structure illustrated in Fig. 2.1 is called O3 due to the stacking of the MX_2 sheets relative to each other. The "O" stands for octahedral, because the resultant A sites are octahedrally coordinated by the anions. The "3" indicates the number of layers in the unit cell when the c lattice parameter is perpendicular to the layer directions. However, the relative stacking can (and often does) change when the concentration of A changes. The different stackings that will be discussed in this work are illustrated in Fig. 2.2. Each of the host structures can

6
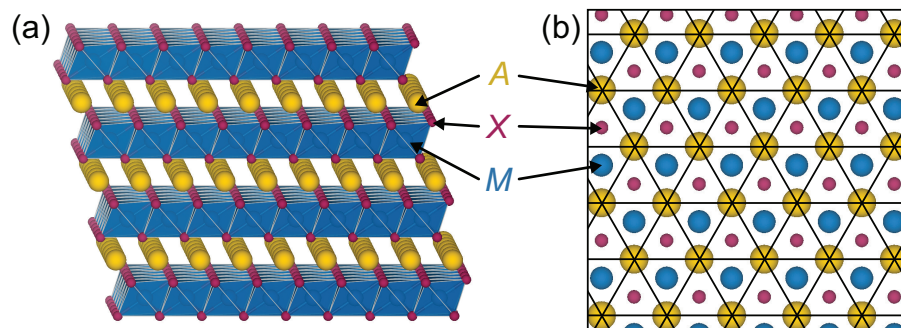
Figure 2.1: (a)Three-dimensional structure of a layered cathode material. (b) Looking down on a subset of three layers, each layer contains atoms on a triangular lattice. Image produced using VESTA software [10].

transform into one of the other without breaking any of the M-X bonds through a simple gliding of the MX_2 sheets.

The O1, O3, and P3 hosts belong to an important family of related layered compounds. In the O1 host, the X sublattice has A-B-A-B type stacking. This results in octahedrally coordinated A sites that share faces with the transition-metal octahedra. As discussed above, the O3 host has an A-B-C-A-B-C anion-sublattice stacking and octahedrally coordinated A sites; however, these do not share faces with the M-X octahedra. The P3 host exhibits A-B-B-C-C-A stacking, resulting in prismatic sites (hence the "P") in the A layer that each share one face with an M-X octahedron. The difference between octahedral and prismatic sites is illustrated in Fig. 2.3.

Besides the difference in A-X coordination, the P3 structure also has a different lattice that the A atoms can occupy. While the A sites of O1 and O3 form two-dimensional triangular lattices, in P3, the anion layers on either side of the A layer are directly on top of each other (C-C stacking), resulting in two trigonal prismatic sites (A and B) for A occupation (Fig. 2.4). The combination of all prismatic sites within a particular A layer of P3 generates a honeycomb lattice. The honeycomb lattice is, in fact, a triangular lattice with a two-atom basis. Each prismatic A site of P3 shares a face with one M-X octrahedron directly above or below it, depending on which sublattice it occupies, which
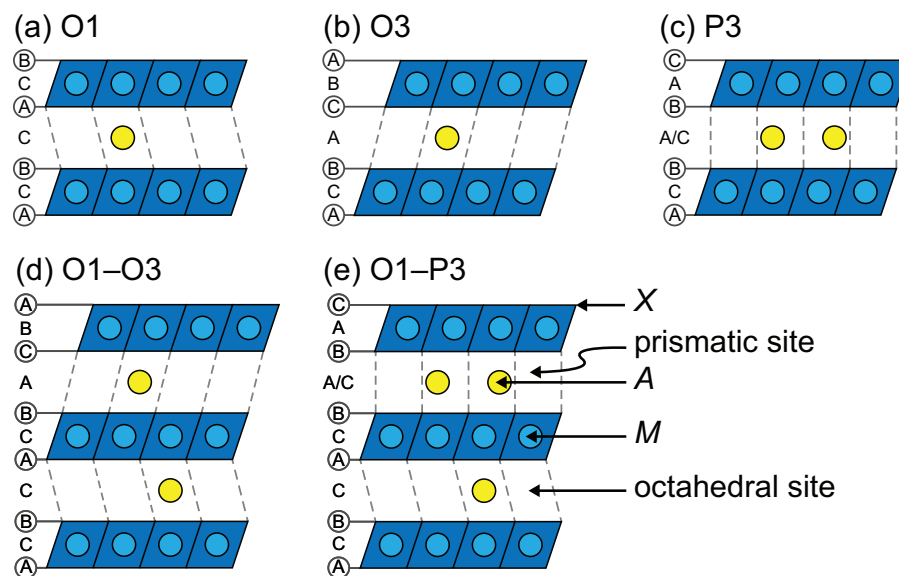
Figure 2.2: Side-view depiction of relative stackings of MX_2 octahedral sheets that result in (a) O1, (b) O3, and (c) P3 structures as well as hybrids (d) O1-O3 and (e) O1-P3. MX_2 octahedra are depicted as blue parallelograms with M in the center and X at the corners (not explicitly shown). A ions are yellow circles occupying an octahedral site or one of two symmetrically equivalent prismatic sites. Relative site positions are indicated using A, B, and C, with X positions circled.
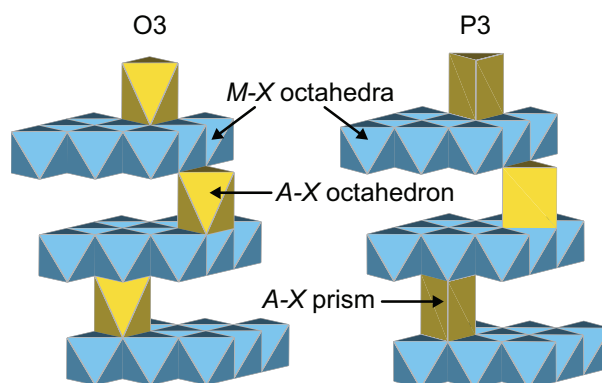
Figure 2.3: Three-dimensional models of the octahedral A sites in O3 and the prismatic A sites in P3. There are two unique prismatic sites in P3. X sites are not explicitly shown but occupy the corners of all polyhedra. Images produced using VESTA software [10].

8
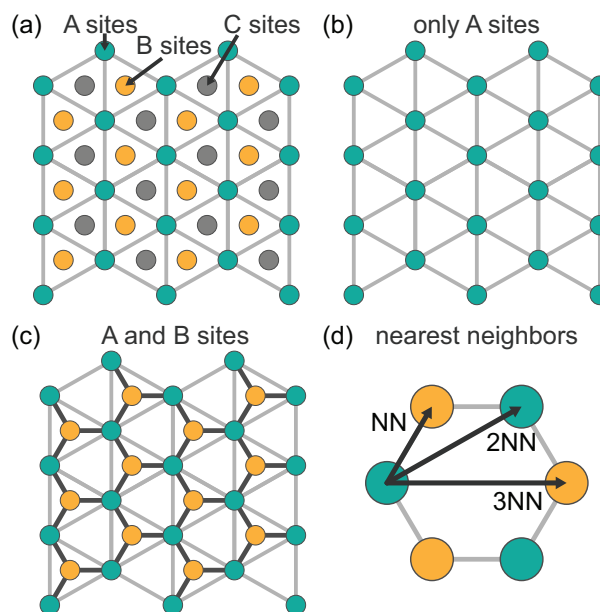
Figure 2.4: (a) A projection of the three different positionings of a triangular lattice. (b) In O3, the octahedral A sites form a simple triangular lattice. (c) In P3, the A ions can occupy one of two symmetrically equivalent trigonal prismatic sites per transition metal that collectively form a honeycomb lattice. (d) First-nearest-neighbor pairs (NN) are much closer in the honeycomb than in the triangular lattice and are unfavorable for simultaneous occupation. The second-nearest-neighbor pairs (2NN) on a honeycomb are the same as the NN of the triangular lattice.

makes the two prismatic sites symmetrically equivalent but unique. As illustrated in Fig. 2.4(d), the P3 honeycomb lattice contains A-A distances not available on the triangular lattices of O3 and O1, such as the pairs labeled NN (nearest-neighbor) and 3NN (third nearest-neighbor). We expect that the sites in the NN pair on the honeycomb lattice will not be simultaneously occupied due to large electrostatic and steric interactions.

The structure library can be extended to include a mixture of the pure stacking sequences (Fig. 2.2(d,e)). Such hybrids may become stable at low intercalant concentrations, as occurs in Li_xCoO_2, where a hybrid combining the stacking sequences of O1 and O3, named H1-3, forms at low Li concentrations [13, 14]; we refer to the H1-3 hybrid as O1-O3 in this text. In addition, we consider a hybrid that combines O1 and P3 hosts. Though Li-ion electrode materials generally do not exhibit P3 stacking due to the small

ionic size of Li, the larger size of Na ions stabilizes the P3 structure and makes an O1-P3 hybrid a likely host of ground-state configurations in Na_xMX_2 chemistries.

2.2   The rocking chair

As mentioned in the introduction, batteries rely on ions migrating from one electrode to the other to store and then release electrochemical energy. The A_xMX_2 is a popular cathode (and, less often, anode) chemistry because the fairly minimal layered MX_2 host allows the A atoms to migrate without large structural changes as opposed to materials that involve significant bond forming or breaking. Some structural changes like shifting in stacking-sequence do occur, and they are the subject of the following chapters. However, the materials are generally cycled in the composition range that avoids phase transitions and are therefore quite reversible [15].

The layered materials function on a rocking-chair principle, as illustrated in Fig. 2.5. The battery is usually first made in the discharged state, with all of the shuttling ions (yellow circles) in the cathode (blue), usually with composition AMX_2. When the battery is charged, energy is used to move A atoms into the anode (gray). A popular anodic material for Li-ion batteries is graphite, which also stores the shuttling ions between layers up to a composition of about LiC_6 [16]. To utilize the full theoretical capacity of the battery, the cathode would be charged to composition MX_2, but, practically, this capacity is never achieved due to drastic lattice parameter changes and phase transitions toward the end of charge [15]. Upon discharge, the A ions return to the cathode, which generates a current of electrons that can be used to power devices.

Ideally, the resulting fully discharged electrode would look like the pristine material, though that is usually not the case. Much like a rocking chair that is eventually settled by friction, the battery continuously loses capacity due to cracks, phase transitions, and side
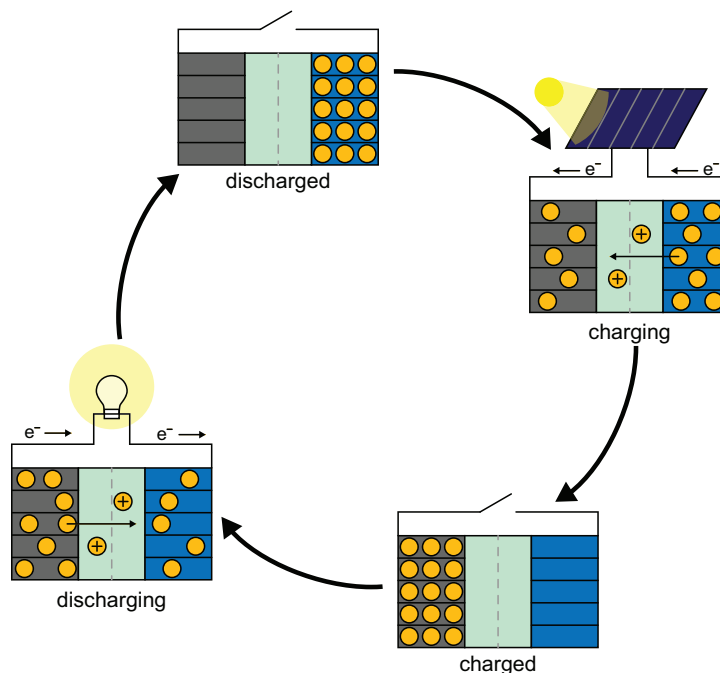
Figure 2.5: Illustration of a battery cycle. When charging, as by a solar cell, positive ions like Li^+ or Na^+ (yellow circles) migrate via electrolyte from the cathode (blue) to the anode (gray). Upon discharge, the process is reversed.

reactions. Nevertheless, the reactions in commercialized batteries are reversible enough to continue "rocking" for hundreds of cycles with only small losses of capacity.

2.3   Electronic structure

In the layered structures, the octahedral coordination of the transition metals by the six anions splits the five M d orbitals into two levels: e_g and t_{2g}, as illustrated in Fig. 2.6. The $d_{x^2-y^2}$ and d_{z^2} orbitals have e_g symmetry, with lobes that point toward the anions. The t_{2g} level contains d_{xy}, d_{xz}, and d_{yz} orbitals, which have lobes that point between the anions. The e_g states have a higher energy than t_{2g} due to the increased electrostatic repulsion from the coordinating anions. The M environment in layered compounds deviates slightly from that shown in Fig. 2.6 because the octahedra are slightly compressed along the principal axis of the crystal. This results in a small
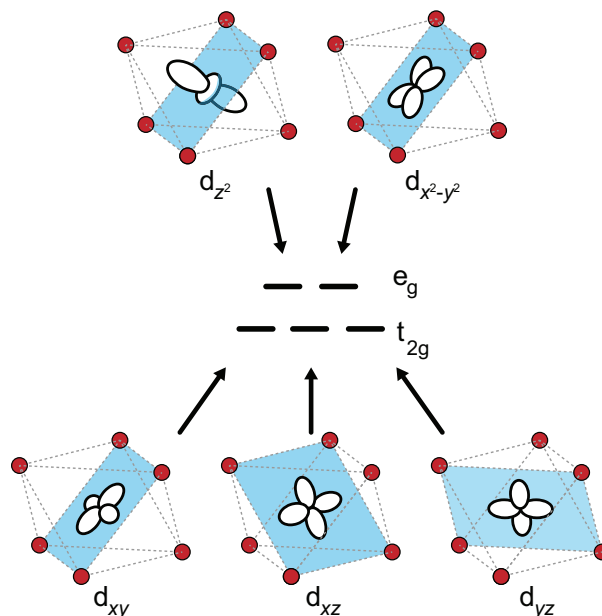
Figure 2.6: Crystal field spitting of d orbitals of a transition metal in an octahedral environment.

splitting of the t_{2g} states (not shown), which is often ignored because it does not strongly affect redox chemistry.

We use nickle oxide (NiO_2) to illustrate how crystal field splitting can be applied to understand electronic structure in MX_2 compounds. A simplified molecular orbital diagram for σ bonding in an isolated Ni-O octahedron is qualitatively illustrated in Fig. 2.7(a). It shows the M orbital splitting from Fig. 2.6 in the context of surrounding electron states and reveals important features about the electronic structure of layered intercalation compounds. The Ni $3d$, $4s$, and $4p$ atomic orbitals hybridize with the O $2p$ orbitals to form bonding and anti-bonding molecular orbitals. The six lowest bonding levels have predominantly O p character. These are followed by three t_{2g} levels derived from the Ni d_{xy}, d_{xz}, and d_{yz} orbitals that point between the O ions in the octahedron. While shown as non-bonding in Fig. 2.7(a), the Ni d_{xy}, d_{xz}, and d_{yz} orbitals actually interact with O p orbitals to form π bonding and anti-bonding states with t_{2g} symmetry. The lowest anti-bonding orbitals have e_g symmetry (referred to as e_g*) and

12
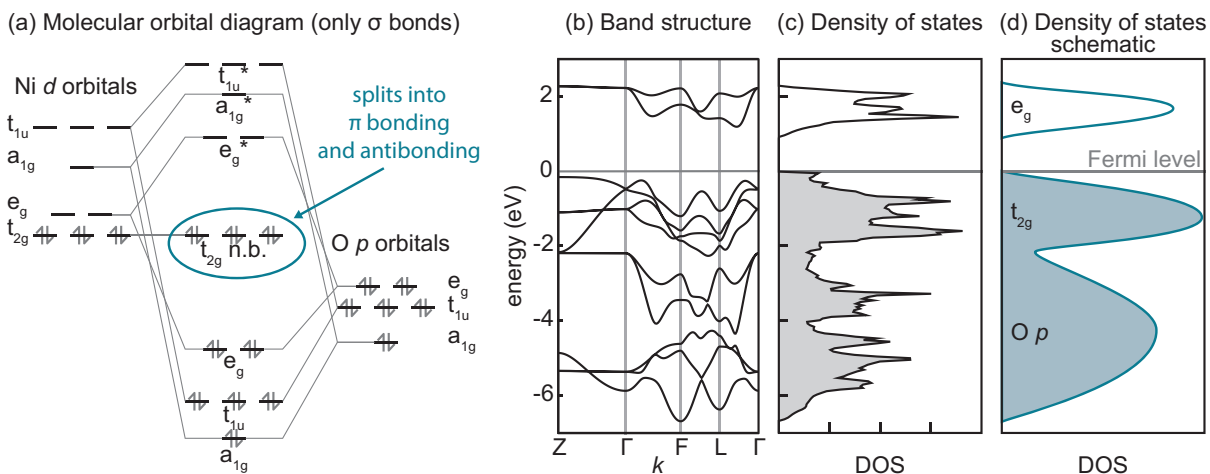
Figure 2.7: Electronic structure of transition-metal layered oxides, using O3 NiO_2 as an example. (a) The molecular orbital diagram of an isolated Ni-O octahedron; only σ bonding is included in this simplified model. (b) The band structure for layered bulk NiO_2. (c) The sum of the bands at each energy level results in the density of states plot. (d) Schematic of the DOS, identifying the bands as mainly O p, t_{2g}, and e_g.

are predominantly of $d_{2z^2-x^2-y^2}$ and $d_{x^2-y^2}$ character.

The molecular orbital levels of Figure 2.7(a) become bands when the Ni-O octahedra are brought together to form the periodic crystal structure of the layered intercalation compounds, as shown in Fig. 2.7(b). The density of states (DOS) plot of Fig. 2.7(c) exhibits three broad regions that coincide with the molecular orbital levels of the isolated Ni-O octahedron. Conventionally, these regions are referred to by their dominating character: O p, t_{2g}, and e_g states, as illustrated schematically in Fig. 2.7(d). The splitting is similar in layered sulfides, except that the weaker electronegativity results in more covalent M-S bonds, so we may expect greater overlap between the S p and M t_{2g} blocks.

In NiO_2, the Fermi level separating the filled from the unoccupied states falls between the t_{2g} and the e_g levels. More generally, the extent to which the states are occupied varies with the number of valence electrons. The intercalating A^+ ions do not hybridize with the bands near the Fermi level. Instead, they function as electron donors and interact ionically with the anions and transition metals.

13

The driving force behind the rocking chair is a difference in electrochemical potential of the electrons, η, between the cathode and anode, referred to as the electromotive force, and η is essentially the Fermi level at each of the electrodes. When the cathode is charged, electrons with the highest energy just below the Fermi level migrate to the anode. Since the top of the occupied states have largely M character, we approximate that the transition metals oxidize from M^{3+} to M^{4+}. We find that though the AMX_2 system is covalent, it is often helpful to think of each atom as having a specific charge: A^+, M^{3+}, and X^{2-}. Upon discharge, the high electrochemical potential of electrons in the anode drives a reverse reaction, whereby the electrons migrate to the cathode and reduce the transition metals back to M^{3+}.

We are often interested in the electronic structure of materials and which electrons are depleted upon charge because this can affect the structure of the material, and vice versa. Changes in geometry affect symmetry and the ionic environment, which can change electron level splitting and shift the relative energies of the levels. Therefore, electronic structure can be integral to understanding why certain geometries are preferred.

Chapter 3

Methods

3.1 Density functional theory

One of the most important tools used in this work is density functional theory (DFT). In theory, DFT allows us to calculate the energy of any crystal given the atom positions and identities. Practically, DFT is limited to systems of hundreds of atoms or less and the energy calculated is not exact. Nevertheless, the results are useful enough to deliver accurate predictions in many cases. It is useful to present a general overview [17, 18] of the DFT method to set a backdrop for some of the concepts discussed later on.

We begin with the time-independent, nonrelativistic Schrödinger equation [19]:

$$\hat{H} \left| \Psi \right\rangle = E \left| \Psi \right\rangle \tag{3.1}$$

where $\hat{H}$ is the Hamiltonian operator, $\left| \Psi \right\rangle$ is the state vector, and E contains the energy eigenvalues. We can express the position-space wave function as

$$\Psi(\vec{r}) = \left\langle \vec{r} | \Psi \right\rangle \tag{3.2}$$

where we have expanded the Hilbert space of the state vector into a complete basis of position unit vectors. This means that, given the correct Hamiltonian and a set of wave functions for the particles, we can exactly solve for the energy of the system.

For a simple system like a single nonrelativistic particle moving in an electric field, the Hamiltonian can be split into two terms:

$$\left[-\frac{\hbar^2}{2m} \boldsymbol{\nabla}^2 + V(\vec{r}) \right] \Psi(\vec{r}) = E\Psi(\vec{r}) \tag{3.3}$$

The term on the right represents the particle's kinetic energy, where $\hbar$ is the reduced Planck constant, m is the mass of the particle, and $\boldsymbol{\nabla}$ is the Laplacian. The second term, $V(\vec{r})$ is the potential energy of the electron due to a non-uniform electric field such that the energy is a function of the particle's position in space, expressed here as the vector $\vec{r}$. This leaves only the wave functions, which are related to the probability density, $P(\vec{r})$, of particles at location $\vec{r}$

$$P(\vec{r}) = \Psi^*(\vec{r})\Psi(\vec{r}) \tag{3.4}$$

This equation has been solved for systems like the H_2 molecule, but becomes intractable for more complex problems [18]. For systems with multiple particles, the wave function contains $3(n + N)$ degrees of freedom (DOFs), where n is the number of electrons, N is the number of atomic nuclei, and the multiple of 3 is for the three spacial dimensions. The Hamiltonian also becomes more complex, where terms for particle interaction with one another must be added.

A few useful approximations allow us to apply the Schrödinger equation to more practical systems and lead us to density functional theory. The Born-Oppenheimer approximation [20] states that since electrons are much smaller and lighter than nuclei, they

relatively instantaneously equilibrate to the local environment. Meanwhile, the sluggish nuclei are considered as point charges fixed in space, interacting with one another. Next, Hohenberg and Kohn [21] showed that the lowest energy state of the system (i.e. the ground state) is a unique functional of the electron density, $\rho(\vec{r})$, and that the electron density that minimizes the energy is the true ground-state electron density. Since the electron density is only a function of the positions of the nuclei, the DOFs for the wave functions is reduced to $3N$, which is especially significant when we consider that each atom contains a single nucleus but can have dozens of electrons. This shift from individual electrons to electron density is what lends DFT its name and its practicality.

The Hamiltonian must also be addressed. Kohn and Sham [22] proposed splitting the kinetic energy and the potential energy of electron-electron interactions into terms that could be solved exactly for non-interacting particles and an exchange-correlation term that captures the remaining quantum mechanical effects missing from the non-interacting particle approach. The result is the expression

$$E[\rho(\vec{r})] = T_S[\rho(\vec{r})] + V_{Nn}[\rho(\vec{r})] + V_H[\rho(\vec{r})] + V_{XC}[\rho(\vec{r})] \tag{3.5}$$

From left to right, the energy, $E[\rho(\vec{r})]$, consists of terms for non-relativistic kinetic energy of the electrons, electron-nuclei interaction potential energy, non-relativistic electron-electron potential energy, and the exchange-correlation correction. The exchange-correlation term accounts for electron self-interaction and the spin of electrons relative to one another, as described by the Pauli exclusion principle. The exact functional form of the $V_{XC}[\rho(\vec{r})]$ is not known [23], though multiple approximations are available and widely used in modern day. In this work, we use the generalized gradient approximation (GGA), which utilizes the local electron density and the local gradient in the electron density to calculate V_{XC}.

These approximations are combined in the Kohn-Sham equations, which showed that the ground state electron density can be found by solving a set of equations that each contain a single electron:

$$[T_S[\rho(\vec{r})] + V_{Nn}[\rho(\vec{r})] + V_H[\rho(\vec{r})] + V_{XC}[\rho(\vec{r})]]\psi_i(\vec{r}) = E_i\psi_i(\vec{r}) \qquad (3.6)$$

The systems calculated in this work are crystals, meaning that atoms are arranged on an infinite, periodic lattice. Therefore, the energy eigenstates can be described by Bloch waves of the form

$$\psi(\vec{r}) = e^{-i\vec{k}\cdot\vec{r}}u(\vec{r}) \qquad (3.7)$$

The exponential term is a plane wave, where $\vec{k}$ is the wave vector, and $u(\vec{r})$ is a function with the same periodicity as the crystal. This approach leads to electronic band structures, which play an important role in Ch. 6. In all sections we mention the density of k-points in reciprocal space and the limits imposed on the Bloch wave by the basis set energy cutoff used in the calculations. Even with a limited k-point density and energy cutoff, calculating the wave functions for all electrons would be very computationally expensive. The cost is reduced by only calculating the wave functions for valence electrons and treating the rest as a pseudopotential grouped with the nucleus. Since several pseudopotentials are usually available for each functional (e.g. different number of electrons treated as valence electrons), we specify which are used in our calculations.

Finally, the general approach to solving for the energy is to first make a guess at the energy density, solve the Kohn-Sham equations to find the wave functions, and then use those wave functions to calculate a new electron density:

$$\rho_{new}(\vec{r}) = \sum_i (\psi_i^*(\vec{r})\psi_i(\vec{r})) \qquad (3.8)$$

18

If the initial and final ground state energies are the same, then the ground state has been found. Otherwise, the electron density is updated and the process repeated iteratively until some convergence criterion is met. We use the method implemented in the Vienna Ab Initio Simulation Package (VASP) [24, 25]. In addition to minimizing energy relative to the electron density, we also minimize the forces relative to ion positions, allowing us to find the lowest energy geometry (or at least a local minimum along the energy surface). With this approach, we are able to find a local ground state with relaxed ion positions starting from an approximate atom arrangement.

3.2   Formation energy

In order to calculate the energy of a crystal, we must define a unit cell (u.c.) that contains the positions and identities of atoms and that represents the smallest repeat unit of the crystal. The resultant absolute energy on its own does not hold much meaning, but we can compare the relative energies of different atomic arrangements to understand thermodynamic equilibrium in the system. The lowest energy structure at a certain composition is thermodynamically most stable and we may expect it to be the most likely to form (at least at 0 K). However, we must be careful when comparing energies of different compounds; only energies of structures that contain the same species and number of atoms can be compared directly. In this work, we are interested in understanding structure evolution across a range of compositions (e.g. changes in a charging cathode), so we turn to formation energies. If we pick two (or more) references that span the composition range, we can calculate the relative energy of a compound in that composition range. For an intercalating material like A_xMX_2, we often want to calculate the formation energy of

19

compounds along the x axis relative to the endpoints MX_2 and A_yMX_2 (where $y \geq x$):

$$E_f(A_xMX_2) = E(A_xMX_2) - (x/y)E(A_yMX_2) - (1 - x/y)E(MX_2) \qquad (3.9)$$

We use E to refer to the energy from DFT, and E_f is the formation energy, all expressed per formula unit (f.u.). It must be noted that the DFT energies can be affected by choice of functional, k-point density, basis energy cutoff, pseudopotentials, and some other calculation settings, so care must be taken to ensure an apples-to-apples comparison.

A plot of formation energy as a function of composition, shown schematically in Fig. 3.1, is a useful tool for determining phase stability at 0 K. A negative formation energy indicates that the compound is more thermodynamically stable than a two-phase segregation of the references (remember that these are all bulk calculations so surface energies are not considered). Therefore, the envelope of the lowest energy structures (i.e. ground states) along a composition range indicates the progression of phase stability. Between each ground state is a two-phase region consisting of the two adjacent configurations.

Of course, we can only compare the energies of structures we calculate. At best, we can only rule out structures with high energies and we never know if we have found the true ground states. Cluster expansions and Monte Carlo methods, discussed below, can be useful tools in predicting low-energy structures.

3.3   Chemical potential and voltage

It may be helpful to compare calculated formation energies to experiments to get a sense of whether or not the calculated energy landscape captures observed phenomena, but experimentalists who study batteries do not typically measure formation energy
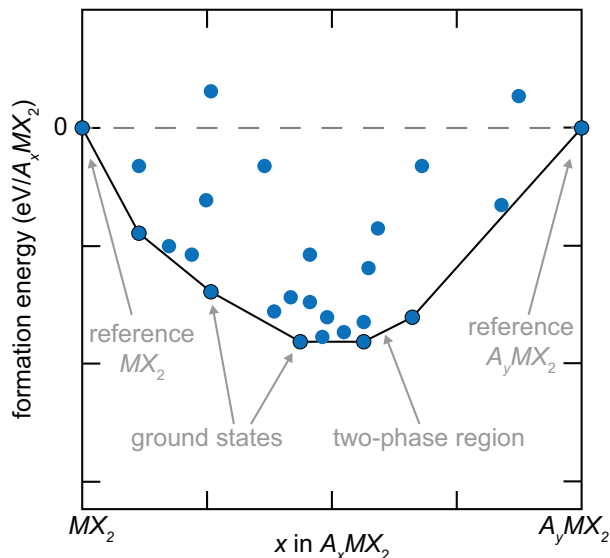
Figure 3.1: Schematic plot of formation energies as a function of composition. Each point corresponds to a different configuration.

directly. They do, however, measure current and voltage as they cycle the electrochemical cell, which can be related back to composition and formation energy. Many experimental papers report capacity in units of mAh/g, which can be directly converted to x in A_xMX_2 as long as the molar mass of the active cathode material is known. Voltage is related to chemical potential, which can be calculated from DFT energies. The derivation is shown below, split into two parts. First, we show the relationship between energy and chemical potential (Eq. 3.16), followed by the equation relating chemical potential to voltage (Eq. 3.21).

In an open circuit battery, equilibrium at constant temperature and pressure is determined by the minimization of Gibbs free energy. From the fundamental thermodynamics relation, the differential equation for Gibbs free energy is

$$dG = -SdT + VdP + \sum_i \mu_i dN_i \tag{3.10}$$

If we assume temperature, T, and pressure, P, are constant (they are in our DFT cal-

21

culations), we are left with a sum over all species, i, for the chemical potential of that species, μ_i, multiplied by the number of that species, N_i. Rearranging, we can express the chemical potential of species A as

$$\mu_i = \left(\frac{\partial G}{\partial N_i}\right)_{T,P,N_{j\neq i}} \tag{3.11}$$

For an interstitial solid such as an intercalation electrode material, the composition is defined by the concentration of the interstitial species:

$$x = \frac{N_A}{N_{MX_2}} \tag{3.12}$$

where N_A is the number of A atoms in the system and N_{MX_2} is the number of MX_2 units. (This is merely a more formal definition of the A_xMX_2 convention we have already been using.) We can set N_{MX_2} to be constant since it functions as a host for the intercalating ions. Therefore, in Eq. 3.11, $i = A$ and $j = MX_2$. The molar Gibbs free energy, g, is the Gibbs free energy, G, divided by the number of formula units:

$$g = \frac{G}{N_{MX_2}} \tag{3.13}$$

We can now rewrite Eq. 3.11 into a more useful equation, with T, P, and N_{MX_2} implied constant moving forward:

$$\mu_A = \left(\frac{\partial(gN_{MX_2})}{\partial N_A}\right)_{T,P,N_{j\neq i}} = N_{MX_2}\left(\frac{\partial g}{\partial N_A}\right) = N_{MX_2}\left(\frac{\partial g}{\partial x}\right)\left(\frac{\partial x}{\partial N_A}\right) \tag{3.14}$$

We can rewrite the right-most differential to remove dependence on N_A and N_{MX_2}.

$$\frac{\partial x}{\partial N_A} = \frac{\partial \left(\frac{N_A}{N_{MX_2}} \right)}{\partial N_A} = \frac{1}{N_{MX_2}} \frac{\partial N_A}{\partial N_A} = \frac{1}{N_{MX_2}} \tag{3.15}$$

such that, combining Eqs. 3.14 and 3.15, we find

$$\mu_A = \frac{\partial g}{\partial x} \tag{3.16}$$

To relate chemical potential to voltage [26], we briefly return to the Gibbs equation, this time for the electrochemical cell including the cathode and anode, adding degrees of freedom not only for the migrating species, A, but also for the concentration of excess electrons in the anode and cathode, e:

$$dG = \mu_A^c dN_A^c + \mu_e^c dN_e^c + \phi^c dq^c + \mu_A^a dN_A^a + \mu_e^a dN_e^a + \phi^a dq^a \tag{3.17}$$

where superscript c indicates cathode, superscript a indicates anode, ϕ is the electrostatic potential, and q is the charge. Due to mass and charge conservation, many variables can be rewritten in terms of dN_A^c. If we assume that charge of the shuttling ion is n,

$$n dN_e^c = dN_A^c$$

$$n q_e dN_e^c = -n dq^c = q_e dN_A^c$$

$$dN_A^a = -dN_A^c$$

$$n q_e dN_e^a = -n dq^a = -q_e dN_A^c$$

where q_e is the charge of the electron. Using the above equalities:

$$dG = \mu_A^c dN_A^c + n\mu_e^c dN_A^c - n\phi^c q_e dN_A^c - \mu_A^a dN_A^c - n\mu_e^a dN_A^c + n\phi^a q_e dN_A^c \tag{3.18}$$

To minimize Gibbs free energy, we set $dG = 0$ and simplify:

$$\mu_A^c + n\mu_e^c - n\phi^c q_e - \mu_A^a - n\mu_e^a + n\phi^a q_e = 0 \tag{3.19}$$

We define an electron electrochemical potential, η_e, as

$$\eta_e = \mu_e - \phi q_e \tag{3.20}$$

Substituting the new definition yields

$$\mu_A^c + n\eta_e^c - \mu_A^a - n\eta_e^a = 0$$
$$\eta_e^c - \eta_e^a = -\frac{\mu_A^c - \mu_A^a}{n}$$

The electromotive force, or voltage, V, is equal to the difference in electron electrochemical potential between the anode and cathode:

$$V = \frac{\eta_e^c - \eta_e^a}{q_e} = -\frac{\mu_e^c - \mu_e^a}{nq_e} \tag{3.21}$$

We will largely be dealing with positive monovalent ions (e.g. Li^+, Na^+) in the role of the shuttling ion, so $n = 1$ in most cases. For comparing with experimental results, the same anode material must be used as reference in calculating voltage. In most studies of electrode materials, the anode is the metallic phase of the shuttling ion because its composition and chemical potential do not change during cycling (i.e. Li added to more Li is still Li). For the calculation, the chemical potential of the anode is the DFT calculated energy of the anode material expressed per f.u., and q_e is already included when units of energy are in electronvolts (eV).

The relationship between energy, chemical potential, and voltage is illustrated in Fig.
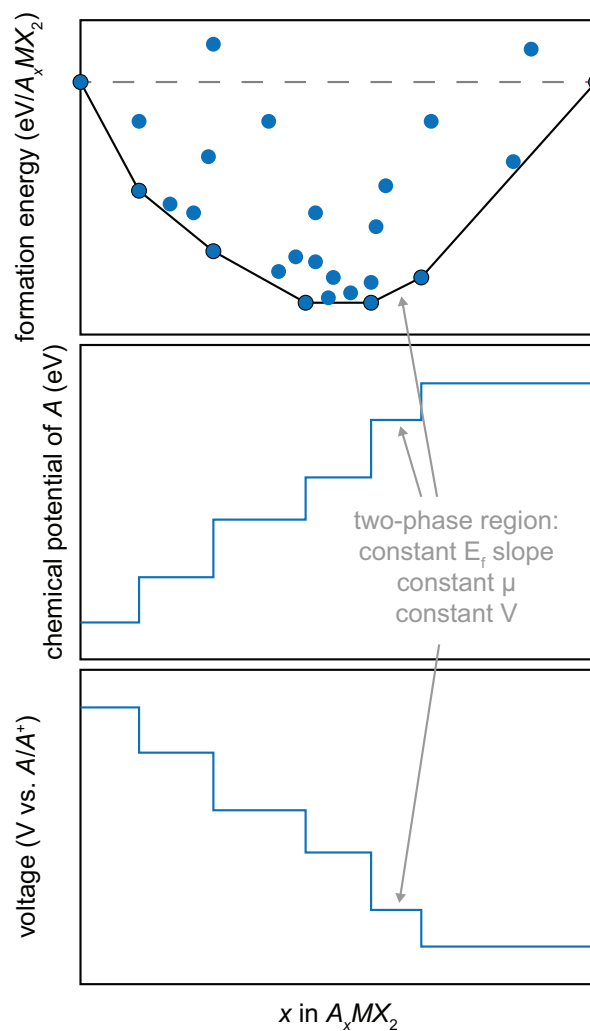
Figure 3.2: Schematic plots illustrating relationship between formation energy, chemical potential, and voltage.

3.2. The chemical potential is essentially the set of slopes along the energy convex hull. The negative of the chemical potential is the average voltage, which is then shifted to reflect voltage versus some anode.

One must be careful to use the correct set of energies (E versus Ef). The above derivations are for the absolute energies calculated with DFT, referred to as E in this work. If formation energies, E_f, with references MX_2 and $A_y MX_2$ are used instead, a

simple change of reference must be applied to Eq. 3.21:

$$V = -\frac{\mu_e^c - E(MX_2)/y + E(A_yMX_2)/y - \mu_e^a}{nq_e} \tag{3.22}$$

3.4 Cluster expansions

It becomes useful, at times, to be able to quickly approximate the energy of a large number of (large) supercells without having to use expensive methods like DFT. For instance, one may want to screen potential ground states from a large pool of candidate configurations or run Monte Carlo simulations that rely on the ability to almost instantaneously determine the energy difference between two configurations. A cluster expansion (CE) is a way to quickly approximate the energy of a system based on its atomic arrangement. It is essentially a best-fit polynomial to energy and configurational data in an n-dimensional space. To facilitate in gathering data, fitting cluster expansions, and running Monte Carlo simulations, our group utilizes an in-house software suite called Clusters Approach to Statistical Mechanics (CASM) [27–30].

Components of the cluster expansion method are illustrated in Fig. 3.3. A primitive cell is chosen that can be tiled to generate the crystal. In O3 A_xMX_2, for instance, the primitive cell contains four basis sites (a transition metal, two anions, and a site for the intercalating ion), and the lattice vectors reflect the A-B-C stacking of the crystal. In this work, we focus only on configurational degrees of freedom; in this case, the intercalating ion site can be occupied by a species A or a vacancy (Va).

The primitive cell is tiled to generate supercells. Each supercell allows for a range of compositions based on the number of available sites, N, for A or Va to occupy. Every unique arrangement of A and Va across the sites is a configuration which can be uniquely
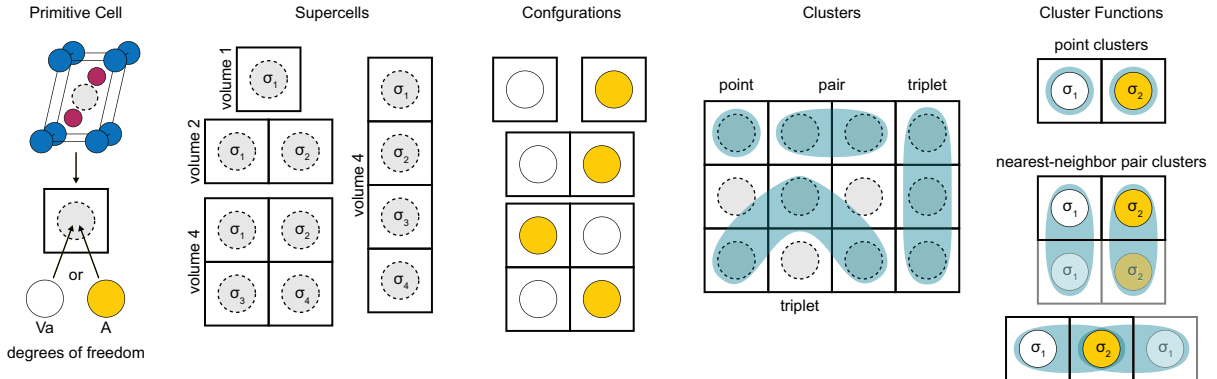
Figure 3.3: A schematic representation of the cluster expansion method. A primitive cell is used to generate supercells and enumerate configurations. Each configuration is described by a truncated set of site clusters. On the far right, dark borders indicate units in the unit cell while the lighter boxes illustrate how clusters can span across unit cells due to the periodic nature of the crystal.

identified by its occupation variables, σ_i:

$$\vec{\sigma} = \{\sigma_1, \sigma_2, \sigma_3, ..., \sigma_N\} \tag{3.23}$$

Since the atoms that make up the host (i.e. the MX_2 matrix) do not vary between the configurations, only the intercalating ion sites need be included.

We assume that each atomic arrangement (i.e. each configuration) has a unique energy and that this energy is the sum of energy contributions from A atom interactions (along with an energy contribution from the matrix that is the same for all of the configurations). The atom interactions are described by clusters. Clusters group sites into points, pairs, triplets, quadruplets, etc. and each cluster has sites that are a certain distance apart from each other. All of the clusters in a crystal (up to an infinite volume and site-site distance) should be able to exactly describe the energy for that system if the energy contribution from each cluster were known. Since infinities are not practical, we truncate cluster size and maximum site-site distance assuming that atoms far away from each other essentially do not interact. Mathematically, the cluster expanded energy,

E_{CE}, can be expressed as

$$E_{CE}(\vec{\sigma}) = V_0 + \sum_\alpha V_\alpha \phi_\alpha(\vec{\sigma}) \tag{3.24}$$

The V variables here are not voltage but rather effective cluster interactions (ECIs), with the V_0 term corresponding to the energy contribution from the host matrix. The energy contribution of each unique cluster, α, is V_α. Lastly, $\phi_\alpha(\vec{\sigma})$ is the cluster function, defined as

$$\phi_\alpha(\vec{\sigma}) = \prod_{i \in \alpha} \sigma_i \tag{3.25}$$

The occupancy of a site is assigned a basis (e.g. $\sigma(\mathrm{Va}) = 0$ and $\sigma(A) = 1$) and the product of these site occupancy variables is used as a proxy for the interactions in the crystal. An example of cluster functions is illustrated in Fig. 3.3. The volume two configuration has two point clusters, one for each site. The point clusters are equivalent due to crystal symmetry, so they have the same ECI. However, the occupancy of the two sites is different and, therefore, so is the energy contribution from each cluster:

$$E_{CE}(\phi_i) = V_{point} \cdot \sigma_1 = V_{point} \cdot \sigma(\mathrm{Va})$$

$$E_{CE}(\phi_j) = V_{point} \cdot \sigma_2 = V_{point} \cdot \sigma(A)$$

$$E_{CE}(\phi_{points}) = V_{point} \cdot (\sigma(\mathrm{Va}) + \sigma(A))$$

For clusters with more than one site, occupancies within each cluster are multiplied, as indicated in Eq. 3.25. As illustrated in Fig. 3.3, clusters can span across unit cells due to the periodic boundary condition.

ECI values are not inherently known; however, since we can calculate fairly accurate energies for a wide range of configurations with DFT, we can fit the unknown V values

to a set of $\vec{\sigma}$ and $E_{DFT}(\vec{\sigma})$ for the set of calculated configurations:

$$\vec{E}_{DFT} = \vec{X}\vec{v} \qquad\qquad (3.26)$$

In the above equation, $\vec{E}_{DFT}$ is a vector of calculated energy values, $\vec{X}$ is a matrix of correlation values with one configuration per row, and $\vec{v}$ is the vector of unknown ECIs. The n cluster functions form an orthonormal basis that generates an n-dimensional space, and the ECI values are projections onto that space. A limited number of dimensions is expected to contribute significantly to the energy, so the solution for the ECI is expected to be sparse, with many $V_\alpha = 0$, resulting in a problem that is overdetermined. We enumerate many clusters and allow a genetic algorithm to pick the best set to represent the system. For each set of clusters, a regression determines the ECI values to minimize some form of $(E_{CE}(\vec{\sigma}) - E_{DFT}(\vec{\sigma}))$, usually root-mean-square (RMS) or weighted-RMS (wRMS). While all configurations are treated equally with RMS, wRMS can be used to capture the energies of configurations along the hull more accurately than those with high energy. Once the $\vec{v}$ is known, the cluster-expanded energy, $E_{CE}(\vec{\sigma})$, can be quickly calculated for any configuration.

Symmetry considerations are employed along each step of the process. First, only symmetrically unique supercells of the primitive cell are enumerated. Supercells are enumerated at least up to a volume that contains the number of sites equal to the largest enumerated cluster to minimize self-interaction. Within each supercell, only symmetrically unique configurations are enumerated and calculated. The number of configurations calculated varies between projects and generally decreases with increasing supercell volume, but is on the order of hundreds per structure. Lastly, only symmetrically equivalent clusters are enumerated and included in the fit for the cluster expansion. As a starting point, somewhere between 100 to 200 clusters may be enumerated, ranging in size be-

tween point and quadruplet, with maximum length cutoffs around 10–15 Å. However, the genetic algorithm should only be allowed to fit to a small fraction of these at a time–about 10–20% of the number of calculated configurations.

A few last notes must be made regarding the cluster expansion method. First, atoms are assumed to lie on the lattice defined by the primitive cell. The enumerated clusters utilize sites on this ideal lattice, not the positions of the atoms in each relaxed configuration. Small perturbations away from lattice sites are assumed to be captured in the energy. However, calculations with large structural changes must be discarded or reassigned to a project with a more appropriate primitive cell. For instance, even though both the O3 and O1 structures have a triangular lattice for Na occupation, the change in layer stacking requires two different projects with O3 and O1 primitive cells, respectively, because the host contribution to the energy will be different in the two cases. Therefore, while winning on speed relative to DFT, the cluster expansion Hamiltonian lacks universality as it is limited to the single system it is fit to.

Second, we assume that each microstate (i.e. configuration) has a single energy value that is determined by $\vec{\sigma}$, following the same principles outlined by Hohenberg and Kohn [21]. In general, this assumption seems simple since for each unique configuration we calculate a single unique energy in DFT. However, we must recall that we are determining the energy based on clusters and, more importantly, a finite number of truncated clusters. Due to the limited number of clusters, some unique configurations may be mapped onto the same point in cluster space resulting in two real energy values but only one cluster-expanded energy value. This must be kept in mind when choosing clusters and configurations.

The cluster expansion formalism is not limited to configurational degrees of freedom nor only energy. Examples of other degrees of freedom include magnetism and strain. Any scalar property of the system, like volume, can be cluster expanded. However,

further extensions of the method will not be discussed in this work.

3.5   Grand canonical Monte Carlo

The macroscopic properties of a system, such as energy, are determined by the ensemble average of its microscopic states. At 0 K temperature, the system minimizes the free energy by occupying the lowest energy state–the ground state. However, as temperature increases, energy can be decreased by increasing entropy, such that sampling a variety of low-energy states becomes favorable. (This is why, at high temperatures, ground states on a phase diagram are surrounded by solid solutions and why solids melt at elevated temperatures.) The partition function, Z, determines how much each microstate contributes to the ensemble average.

$$Z = \sum_{\vec{\sigma}} \exp(-\beta \Omega(\vec{\sigma})) \tag{3.27}$$

$$\beta = \frac{1}{k_B T}$$

The variable $\Omega(\vec{\sigma})$ is a free energy of the microstate, the exact form of which depends on the constraints on the system. We can calculate the probability of a particular microstate, $P(\vec{\sigma})$, at a finite temperature using

$$P(\vec{\sigma}) = \frac{1}{Z} \exp(-\beta \Omega(\vec{\sigma})) \tag{3.28}$$

As stated earlier, a macroscopic thermodynamic quantity, X, can be determined from the microscopic thermodynamic quantities for each state:

$$X = \sum_{\vec{\sigma}} X(\vec{\sigma}) P(\vec{\sigma}) \tag{3.29}$$

If we are interested in the energy of the system, the energy values for each microstate can be calculated from the cluster expanded free energies. Remember, the purpose of the cluster expansion is to quickly approximate the energy as a function of $\vec{\sigma}$. We use the Metropolis–Hastings algorithm [31, 32], a type of Marcov chain Monte Carlo (MCMC), to determine the probability of microstates. The probability of sampling a state is based on the Boltzmann distribution.

The Marcov chain [33] dictates that the probability of transitioning into a state is determined only by the previous state, as opposed to some absolute value. In our case, the transition probability is a function of the change in energy between the initial, I, and final, F, states expressed as

$$\Delta\Omega^{I \to F} = \Omega(\vec{\sigma}_F) - \Omega(\vec{\sigma}_I) \tag{3.30}$$

If energy is lowered from the initial to the final state (i.e. $\Delta\Omega^{I \to F} < 0$), the transition occurs with probability 1. If $\Delta\Omega^{I \to F} > 0$, the transition occurs with probability

$$P^{I \to F} = \exp\left(-\Delta\Omega^{I \to F}\beta\right) \tag{3.31}$$

With sufficient sampling, Monte Carlo is able to generate converged ensemble averages.

The term grand canonical Monte Carlo refers to the constant μ, V, and T constraints imposed on the system. We can replace Ω with the grand canonical free energy, Φ:

$$\Omega(\vec{\sigma}) = \Phi(\vec{\sigma}) = E(\vec{\sigma}) - \mu_A N_A \tag{3.32}$$

We have removed the term that includes pressure as there is no imposed pressure in these calculations. We also do not consider the contribution to energy from the MX_2 matrix; since the matrix is the same for all configurations, it should have no affect on energy

differences between them.

3.6   Gibbs free energy

The output of grand canonical Monte Carlo provides the chemical potential (this is one of the fixed quantities), ensemble average composition, and ensemble average internal energy for each set of conditions. To calculate the Gibbs free energy, the energies must be integrated along a specific path in chemical-potential and temperature space, from a starting point with known g. In this work, integration traverses a constant chemical-potential path from close to 0 K (where entropy contribution is negligible) to the finite temperature of interest followed by a constant-temperature path with increasing (or decreasing) chemical potential starting at the end of the first path (illustrated in Fig. 3.4). Integrating over a phase transition accumulates errors, so a different chemical potential heating run should be used inside each of the single-phase regions to increase accuracy.

The grand canonical free energy, Φ, can be defined in terms of the partition function (Eq. 3.27) as

$$\Phi = -k_B T \ln Z = -\frac{1}{\beta} \ln Z \tag{3.33}$$

We integrate the grand canonical free energy from condition 0 (T_0, μ_0) to condition 1 $(T_1, \mu_1 = \mu_0)$ along temperature at fixed chemical potential:

$$\left(\frac{\partial(\Phi\beta)}{\partial\beta} \right)_\mu = -\left(\frac{\partial(\ln Z)}{\partial\beta} \right)_\mu = \frac{\sum_{\vec{\sigma}} \Phi \exp(-\beta(E(\vec{\sigma}) - \mu N))}{\sum_{\vec{\sigma}} \exp(-\beta(E(\vec{\sigma}) - \mu N))} = \langle E(\vec{\sigma}) - \mu N \rangle \tag{3.34}$$

$$\beta_1 \Phi_1 = \beta_0 \Phi_0 + \int_{T_0}^{T_1} \langle E(\vec{\sigma}) - \mu N \rangle \, d\beta \tag{3.35}$$
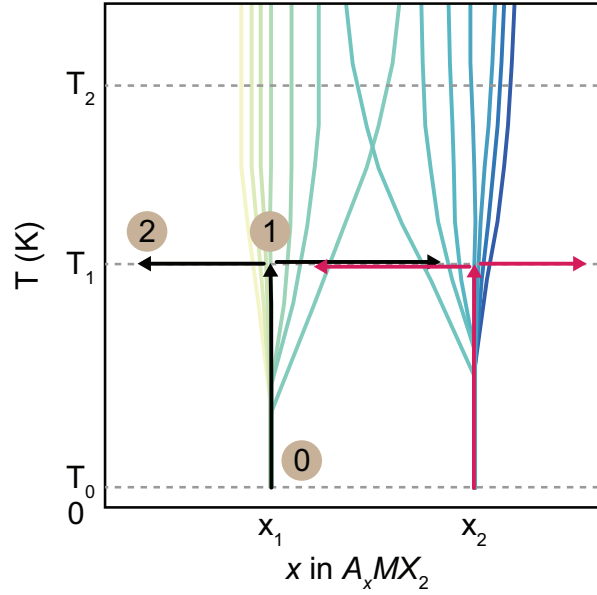
Figure 3.4: Illustration of MC constant μ, increasing T runs at different μ (lines ranging from yellow to blue). The black and magenta arrows indicate integration paths for g. At higher temperature, T_2, a single heating path could be chosen due to lack of phase transitions between compositions x_1 and x_2. Conditions 0, 1, and 2 for free energy integration are labeled for one of the paths.

The $\langle \rangle$ indicate the expectation value of the quantities as calculated with MC. Molar quantities can be obtained by dividing the resultant equation by the number of unit cells, N_{MX_2}:

$$\beta_1 \phi_1 = \beta_0 \phi_0 + \int_{T_0}^{T_1} \langle E - \mu x \rangle \, \mathrm{d}\beta \tag{3.36}$$

After the heating integration, a path from condition 1 (T_1, μ_1) to condition 2 $(T_2 = T_1, \mu_2)$ along chemical potential at fixed temperature must be integrated:

$$\left(\frac{\partial(\Phi)}{\partial \mu} \right)_T = -\frac{1}{\beta} \left(\frac{\partial(\ln Z)}{\partial \mu} \right)_T = -\frac{1}{\beta} \frac{\sum_{\vec{\sigma}} \beta N \exp(-\beta(E(\vec{\sigma}) - \mu N))}{\sum_{\vec{\sigma}} \exp(-\beta(E(\vec{\sigma}) - \mu N))} = -\langle N \rangle \tag{3.37}$$

$$\Phi_2 = \Phi_1 - \int_{\mu_1}^{\mu_2} \langle N \rangle \, \mathrm{d}\mu \tag{3.38}$$

Once again, dividing through by N_{MX_2} results in molar quantities:

$$\phi_2 = \phi_1 - \int_{\mu_1}^{\mu_2} x \mathrm{d}\mu \tag{3.39}$$

We can use an identity mentioned above to convert from ϕ_2 to g_2:

$$\phi = g - \mu x \tag{3.40}$$

$$g_2 = \phi_1 + \mu_2 x_2 - \int_{\mu_1}^{\mu_2} x \mathrm{d}\mu \tag{3.41}$$

Armed with Eqs. 3.36 and 3.41, the Gibbs free energy for any point in chemical-potential and temperature space can be calculated as long as paths are chosen carefully. Integration from low temperature can be skipped if the chemical potentials start at extreme values where configurational entropy is negligible, such as at the edges of $A_x MX_2$ composition where the layered cathode material is fully intercalated or the intercalant layers are completely empty. From Gibbs free energy, voltage can be calculated using Eq. 3.22, keeping careful track of references.

Chapter 4

Na_xTiS_2

The performance of Na-ion batteries is sensitive to the nature of cation ordering and phase transformations that occur within the intercalation compounds used as electrodes. In order to elucidate these effects in layered Na intercalation compounds, we have carried out a first-principles statistical mechanics study of Na ordering and stacking-sequence preferences in the model compound Na_xTiS_2 [34]. Our calculations predict a series of structural phase transitions at room temperature between O3, P3, O1, O1âĹŠO3 staged hybrid, and O1âĹŠP3 staged hybrid. We further explore the ordering of Na ions in P3 and O3 and find that these host structures favor very distinct Na-vacancy patterns. Low energy orderings on the honeycomb lattice in P3 consist of triangular island domains with vacancies coalescing at antiphase boundaries. This results in a devilâĂŹs staircase of ground-state Na orderings within P3 that are unlike the orderings possible in the triangular lattice of Na sites in O3. Lastly, we explore the role that antiphase boundaries play in mediating Na diffusion in the P3 host.

4.1   Introduction

Improvements in electrochemical energy storage are important in promoting renewable energy in transportation and grid storage. Increasing attention has been drawn to Na-ion intercalation materials as an alternative to Li-ion batteries [35,36]. Not only is Na more abundant than Li, but Na-ion electrode materials also behave differently from their Li-ion counterparts due to differences in ionic size and electronic structure. One stark contrast is the stability of prismatic coordination of Na in layered oxides and sulfides which is not observed in Li due to the latter's smaller ionic radius [37–40]. The crystal structure of the host plays a crucial role in determining electrochemical voltage profiles, cation diffusion mechanisms, and diffusion coefficients [41]. Layered Na intercalation compounds undergo phase transformation sequences that are distinct from those seen in Li-ion electrode materials and as yet not thoroughly explored [12, 42–55]. Such phase transformations can cause degradation as stresses accompanying changes in structure may induce crack initiation and growth [56,57]. Phase transformations can also lead to irreversibilities and hysteresis in the voltage profile due to asymmetries between the multiple kinetic processes required to affect an abrupt change in crystal structure and composition [58]. Phase transformations are generally avoided to increase the lifetime of the battery, which often limits the battery's capacity. It is, therefore, crucial to understand when structural changes occur, how they affect the properties of the battery, and whether they can be suppressed.

A large number of layered Na transition-metal oxides and sulfides have been studied experimentally [40], and many assume the O3 crystal structure [12] when synthesized as NaMX_2. The size and electronegativity of the anions and cations appears to play a decisive role in determining whether O3 undergoes a stacking-sequence change to a P3 host structure upon Na removal [37, 38, 59]. For example, the O3 forms of NaCoO$_2$,

NaNiO$_2$, and their alloys undergo a transformation to P3 during deintercalation [12, 42, 43, 48, 53], while NaTiO$_2$ maintains its O3 host at high levels of charge [55]. In some compounds such as Na$_x$VO$_2$, the transition from O3 to P3 requires thermal activation [60].

The large number of steps in the voltage profiles of many layered Na intercalation compounds suggests a prevalence of phase transitions associated with Na ordering and/or stacking-sequence changes [12, 43–45, 49–53]. The steps are usually more pronounced than in most layered Li-intercalation compounds. Ordering tendencies within the P3 host remain largely unexplored, especially at finite temperature. Diffusion mechanisms within the P3 host are also not fully understood [61], but experimental evidence for Na$_x$Co$_{0.6}$Ni$_{0.4}$O$_2$ suggests that Na mobility may be higher in P3 than in O3 [43]. A common property of many transition-metal oxides and sulfides is the importance of local interactions between the transition metal and Na. Local charge ordering and Jahn-Teller distortions, for example, have been shown to affect ordering preferences among Na within layered intercalation compounds [62].

In this study, we use the Na$_x$TiS$_2$ ($0 \leq x \leq 1$) system as a model to study phase stability and intercalating cation ordering in the O1/O3/P3 family of structures using first-principles statistical mechanics approaches. This system has been studied experimentally and found to exhibit O1/O3/P3 family stacking and staging phenomena [63–65]. The absence of localized charge ordering and Jahn-Teller distortions in Na$_x$TiS$_2$ makes it an ideal model to isolate the role of Na-Na interactions and host crystal structure on phase stability and Na ordering tendencies [66, 67]. We combine first-principles density functional theory with the cluster expansion formalism and grand canonical Monte Carlo simulations to predict phase stability, finite temperature ordering, and the equilibrium voltage curve at 300 K. We find that the P3 host structure is not only stabilized at intermediate Na concentrations but that hybrid staged structures with mixed O1-O3 and

O1-P3 stackings are also stable at low Na concentrations. In addition, we find that the Na ions and vacancies in the P3 host, due to its honeycomb lattice, organize into triangular islands of perfectly ordered domains separated by antiphase boundaries at high Na concentrations. This results in a devil's staircase of ground-state orderings [68, 69] that has not been previously explored in layered intercalation materials at finite temperatures. An analysis of migration pathways in P3 suggests that the diffusion mechanisms may be fundamentally different from those in O3, with antiphase boundaries serving as channels for Na transport. Our findings for Na$_x$TiS$_2$ shed light on structural stability, ordering tendencies, and diffusion mechanisms in other layered oxide and sulfide materials.

4.2 Methods

We investigated phase stability of Na$_x$TiS$_2$ as a function of Na concentration, x, at 0 K and at room temperature using first-principles statistical mechanics methods The equilibrium phases at 0 K are those that minimize the energy of the system. Energies of different structures having composition Na$_x$TiS$_2$ were calculated with first-principles density functional theory (DFT) using the Vienna Ab Initio Simulation Package [24, 25] with PAW pseudopotentials [70, 71] and the optB86b-vdW functional [72–75]. Based on convergence tests, the energy cutoff was chosen to be 530 eV and the k-point mesh density to be 30 Å. See Table 4.1 for details on number of calculations completed.

Equilibrium at finite temperature is determined by a minimum of the free energy, which has contributions from entropy arising from thermal excitations. Layered Na transition-metal intercalation compounds are stable in a variety of host crystal structures depending on their Na concentration and temperature. Since the candidate host structures have distinct symmetries, they can each be described thermodynamically by a separate free energy. Configurational degrees of freedom resulting from all the possible

ways of distributing Na and vacancies over intercalation sites are the dominant source of entropy for intercalation compounds at room temperature [76]. We calculated free energies as a function of composition and temperature for the O3, the P3, the O1-O3 hybrid (i.e. H1-3), and the O1-P3 hybrid host structures with a cluster expansion [77,78] (CE) approach and grand canonical Monte Carlo (MC) simulations.

The Clusters Approach to Statistical Mechanics (CASM) [27–30] software package was used to construct a CE for each host structure (except for O1) and to perform grand canonical MC simulations. A large number of Na-vacancy orderings were enumerated within each host structure. The fully relaxed energies of these orderings were calculated with DFT (optB86b-vdW) and were used to parameterize the ECI using a genetic algorithm [79]. In the present study, the clusters of each CE were limited to points, pairs, triplets, and quadruplets. The weighted root-mean-square (wRMS) (Table 4.1) was less than 4 meV in each CE, where the weights were assigned exponentially with respect to the distance from the local convex hull. Grand canonical MC simulations were applied to each CE to calculate the dependence of the Na concentration on chemical potential and temperature (supercell sizes for MC simulations are listed in Table 4.1). These relationships were integrated to calculate free energies for each host structure [80]. A grid of chemical potentials with increments of no more than 25 meV/atom was used at different temperatures. Cooling runs were performed for each chemical potential from 1000 K to 100 K at a 5 K interval.

As will be expanded on below, our DFT results predict that the O1 structure is only stable at composition $x = 0$. This is observed in many other intercalation materials, including Li$_x$CoO$_2$ [13]. Since there are no Na atoms to generate configurational entropy at this composition, we set the free energy of O1 equal to its energy. Likewise, the O1 layers in the O1-P3 and O1-O3 hybrids were assumed to remain vacant in the entire Na composition range. This results in staging, wherein every other Na layer is left completely

unoccupied.

structure	calculated	clusters in fit	wRMS (meV)	TiS$_2$ units in MC
O1	15	–	–	–
O3	193	21	2.1	9,600
P3	277	25	2.7	8,192
O1-O3	91	17	0.9	5,400
O1-P3	60	16	3.9	7,776

Table 4.1: First column: host structure. Second column: number of symmetrically distinct Na-vacancy orderings that converged and did not relax to a different structure during DFT energy minimization. Third column: the number of non-zero expansion coefficients in the cluster expansion. Fourth column: weighted RMS error, which indicates how well the CEs fit the DFT data. Fifth column: number of Na$_x$TiS$_2$ unit cells in supercells used in MC simulations.

4.3   Results

4.3.1   DFT calculations

Fig. 4.1 shows the DFT formation energies of the ground-state Na-vacancy orderings within each host structure. The formation energies in Fig. 4.1 are calculated relative to O1 TiS$_2$ at $x = 0$ and O3 NaTiS$_2$ at $x = 1$. The ground-state orderings were determined by finding the convex hull of the fully relaxed energies of all Na-vacancy orderings considered within the different hosts. While the energies of a large number of Na-vacancy orderings were calculated (Table 4.1), there may be lower energy orderings in large supercells that were not considered in this study. This is especially true for the P3 host since previous studies of low-energy orderings on the honeycomb lattice using short-range lattice model Hamiltonians [68] have predicted a sequence of ground-state orderings requiring supercells that are substantially larger than can be treated with current DFT methods.

The global convex hull of all orderings (solid black line in Fig. 4.1) shows that the
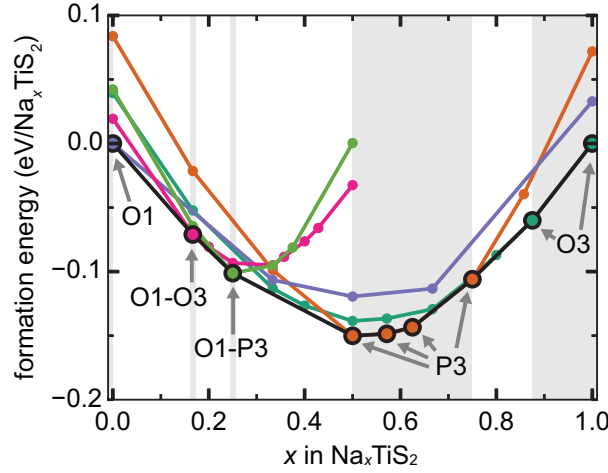
Figure 4.1: Calculated formation energies of configurations on the convex hull for each host structure. Configurations with energies above the hull are not shown. The global convex hull is outlined in black.

relative stability among the different hosts is very sensitive to Na concentration. At high Na concentrations ($7/8 \leq x \leq 1$), O3 is predicted to be stable. The P3 host becomes stable at intermediate Na concentrations ($1/2 < x < 3/4$), with a small two-phase region $3/4 < x < 7/8$ separating O3 from P3, consistent with experimental studies that observe P3 stacking in deintercalated Na$_x$TiS$_2$ [52,81]. Below $x = 1/2$, the hybrid phases O1-P3 and O1-O3 are stable with ground state orderings at $x = 1/4$ and $x = 1/6$, respectively. In these structures, the O1 layers are empty, and the lowest energy configurations of the P3 and O3 layers are similar to those on the hulls of their respective non-hybrid structures. Finally, at $x = 0$, the O1 host becomes stable.

It is instructive to inspect the low-energy Na-vacancy orderings in the P3 host and compare them to orderings in O3. At $x = 1$, there is only one Na configuration possible in O3 as all sites of the triangular lattice are occupied at this composition. In P3, the lowest energy ordering at $x = 1$ has Na occupying exclusively one of the triangular sublattices as shown in Fig. 4.2(a). Any other ordering in P3 at this composition would require the simultaneous occupation of a nearest-neighbor pair, which would lead to a very large
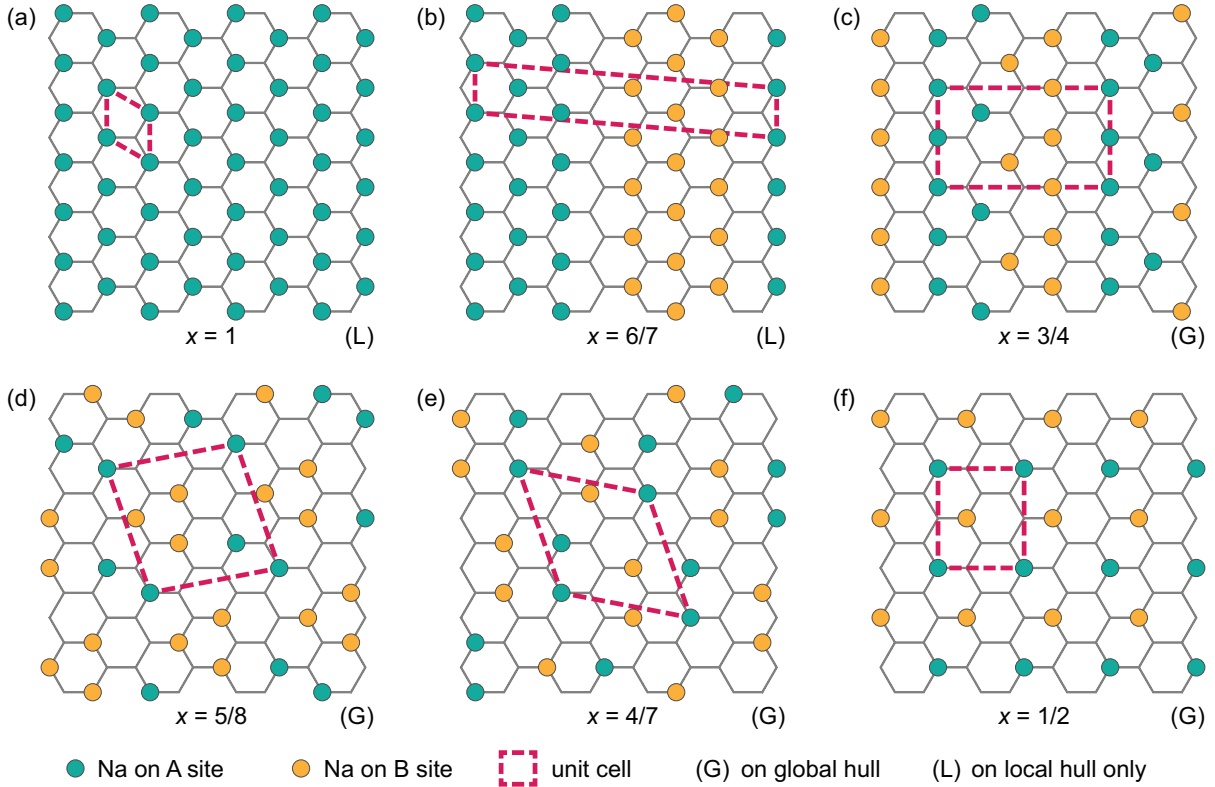
Figure 4.2: Na-vacancy orderings on the convex hull of enumerated configurations within P3. Occupancy of the two sublattices on the honeycomb lattice of P3 is distinguished with different colors (green and yellow).

energy penalty due to strong electrostatic and steric repulsion through the shared face of a pair of nearest-neighbor trigonal prismatic sites.

Below the composition of $x = 1$, vacancies are incorporated differently in P3 than in O3. In O3, which has a single triangular lattice, any ordering can be achieved by simply removing Na atoms. Although this mechanism can occur in P3, it is more favorable to remove Na atoms while rearranging others to occupy a mixture of the two available sublattices in a honeycomb lattice. This can result in domains that consist of Na atoms that occupy a single triangular sublattice as at $x = 1$. These domains are separated by antiphase boundaries (APBs), which accommodate the vacancies that are introduced as Na is extracted. For instance, the lowest-energy ordering enumerated in P3 at $x = 6/7$

(Fig. 4.2(b)) consists of alternating, linear strips of A domains and B domains (two colors are used to highlight the difference in sublattice occupation). APBs separate the strips and concentrate the vacancies introduced upon removal of Na. This leads to a reduction in energy as the APBs allow an increase in the distance between neighboring Na ions. The ground states at $x = 3/4$, 5/8, and 4/7 (Fig. 4.2(c-e)) accommodate vacancies in a similar way. The total length of APBs must increase as the vacancy concentration increases (Na concentration decreases). This is achieved by reducing the size of A and B domains. The orderings at $x = 5/8$ and $x = 4/7$ consist of isolated two-atom and three-atom islands as can be seen in Fig. 4.2(d,e).

The low-energy orderings in P3 shown in Fig. 4.2(a-e) are consistent with past studies of ground state orderings on the honeycomb lattice. Using simple lattice model Hamiltonians, Kanamori [68] showed that repulsive nearest- and second-nearest-neighbor pair interactions on the honeycomb lattice result in a devil's staircase of a countably infinite number of ground state orderings consisting of APBs. The devil's staircase starts with full occupancy on one sublattice as in Fig. 4.2(a) and continues with orderings having triangular A and B island-like domains separated by APBs, such as the ordering illustrated in Fig. 4.3. The A and B domains correspond to perfectly ordered regions with Na occupying exclusively one sublattice. The APBs that separate the domains are indicated by solid black lines. Such large triangular islands are not present in enumerated orderings calculated using DFT as these orderings require large supercells.

At $x = 1/2$, the lowest energy ordering in the P3 host does not consist of domains separated by APBs; instead, Na atoms uniformly distribute themselves over the two available sublattices of the honeycomb (Fig. 4.2(f)). This configuration is compared to $x = 1/2$ orderings in the O3 host in Fig. 4.4. We found two nearly degenerate, low-energy orderings for O3 at $x = 1/2$. One, shown in Fig. 4.4(a), is the zig-zag line ordering that is a common ground state in Na transition-metal oxides having the O3 structure [82].
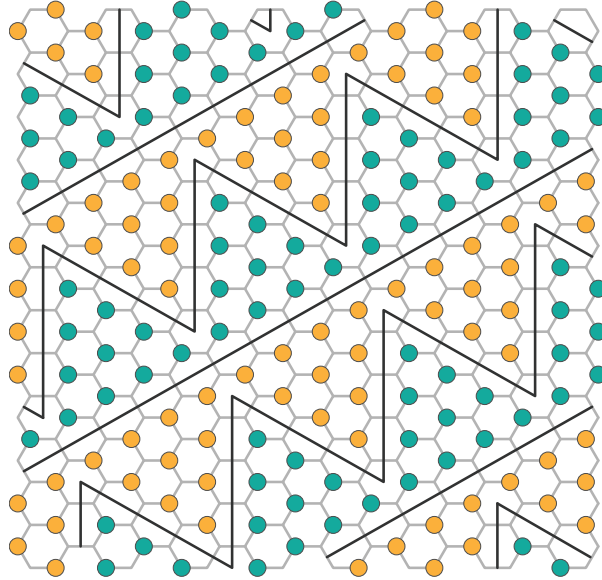
Figure 4.3: An example of a ground state ordering on a honeycomb lattice belonging to the devil's staircase discovered by Kanamori [68]. Occupancy of the two sublattices on the honeycomb lattice is distinguished by use of green and yellow circles. Triangular island-like domains are separated by antiphase boundaries (black lines).

The second ordering (Fig. 4.4(b)), which is the ground state of O3 Na$_x$TiS$_2$ at $x = 1/2$, consists of clusters of four Na atoms and is less than 1 meV/atom more stable than the zig-zag ordering of Fig. 4.4(a). A comparison of the low energy O3 orderings of Fig. 4.4(a) and (b) with the $x = 1/2$ ground state in P3 (Fig. 4.4(c)) reveals that the Na ions in P3 have more flexibility as to how they can order due to the availability of two triangular sublattices. While nearest neighbors cannot be avoided in the O3 structure at this composition, the additional available sites on the honeycomb of the P3 host enable Na atoms to be spaced farther apart from each other. This ability to increase the distance between neighboring Na ions within P3 relative to O3 is likely a dominant factor making P3 more stable than O3 at intermediate Na concentrations, despite the unfavorable face-sharing repulsive interactions between prismatic Na sites and the Ti-S octahedra in P3.
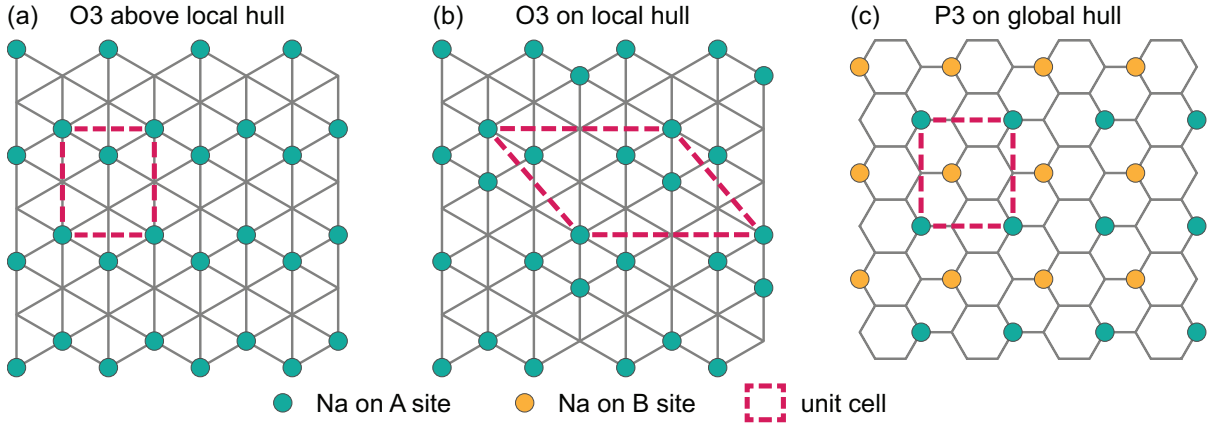
Figure 4.4: Comparing O3 (a,b) and P3 (c) orderings at $x = 1/2$ shows that while nearest-neighbor pairs cannot be avoided in O3, the 3NN sites on the honeycomb lattice allow the Na atoms to be more spread out.

4.3.2 Finite temperature

First-principles DFT energies of different Na-vacancy orderings were used to parameterize cluster expansions for each host, which were subsequently subjected to grand canonical Monte Carlo (MC) simulations to calculate finite-temperature thermodynamic properties. Fig. 4.5(a) shows the calculated free energy curves as a function of Na concentration at 300 K for the different host structures. Application of the common-tangent construction reveals that all of the stacking sequences that were on the DFT global hull are still stable at 300 K, starting with O1 at $x = 0$ and continuing to O1-O3, O1-P3, P3, and O3 upon Na intercalation. At temperatures slightly above 300 K, the O1-O3 phase is no longer stable relative to O1 and O1-P3. The MC simulations predict that most ground-state orderings undergo an order-disorder transition below room temperature. One exception is the ground state ordering at $x = 1/2$ in P3. It is predicted to disorder slightly above room temperature.

Fig. 4.5(b) shows the predicted voltage curve at 300 K, which is related to the slope of the free energy curves in Fig. 4.5(a). Sloping regions in voltage signify single phase regions while plateaus, which arise from a constant chemical potential along a
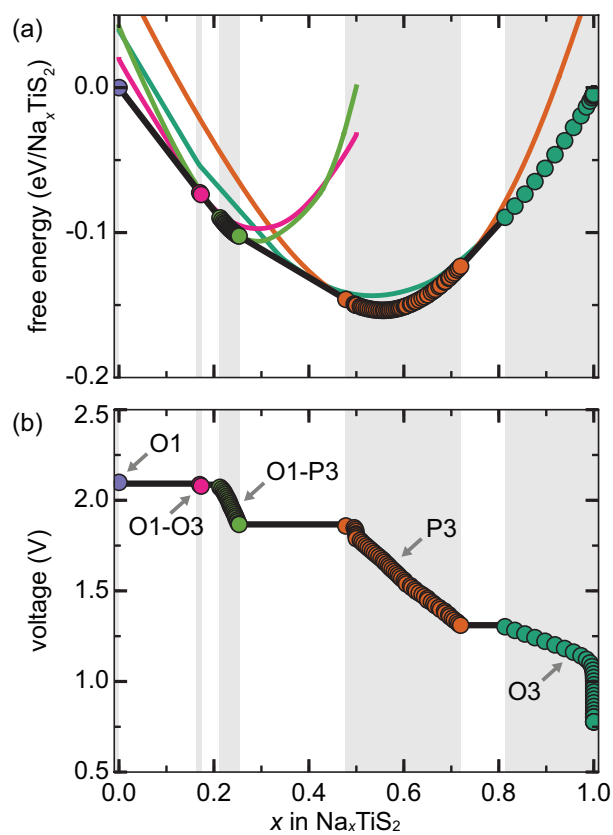
Figure 4.5: The calculated (a) free energy and (b) equilibrium voltage curve at 300 K. Each host structure (i.e. O3, P3, P3-O1, O3-O1 and O1) has a separate free energy curve. A common tangent construction (black solid line) determines global equilibrium. Gray background indicates single-phase regions, white background is used for two-phase regions.

common tangent, indicate a coexistence between two phases. The predicted voltage curve also exhibits a small step at $x = 1/2$ due to the stability of Na ordering at that composition at 300 K. The O1-P3 hybrid phase appears as a large step while O1-O3 is predicted to be stable in a very narrow voltage window. Our results align closely with the features observed experimentally [52, 63–65]. These experiments show a region at high Na concentrations of octahedral coordination, a first-order phase transformation to prismatic coordination around $x = 0.8$, and transformations to staged phases at lower Na compositions. In addition to the stage two ordering that is seen in our calculated voltage curve associated with O1-P3, there is also experimental evidence for a stage three ordering wherein only every third layer contains Na atoms [65]. Higher-order hybrids (e.g. orderings with O1-O1-P3 layer repeat unit) were not included in our analysis. The sharp step at $x = 0.5$ in the calculated voltage curve, which is due to Na ordering, is shifted to a slightly lower concentration in the voltage curve measured by Winn, et al. [64] but to a higher concentration in the voltage curve measured by Lee, et al. [52] The shifts may be due to experimental uncertainty in the state of charge [83].

Microstates from MC simulations of P3 illustrate the importance of APBs even at elevated temperature. Fig. 4.6 shows selected Na layers from several MC sampled microstates for a range of Na concentrations. Different colors are used to distinguish occupancy of the two triangular sublattices of the honeycomb lattice. At $x \approx 1$, Na orders on a single sublattice consistent with 0 K ground states predicted by DFT. Vacancies at lower Na concentrations are accommodated through the formation of APBs that separate A and B domains. Due to the finite size of the MC supercells and finite chemical potential grid, APBs first appeared around $x = 0.96$. At this Na concentration, the domains are large and triangular, with well-defined APBs separating extensive A and B domains. As the Na concentration decreases further, more APBs must form, and the domains become smaller. While triangular domains are still easily discernible in Fig. 4.6
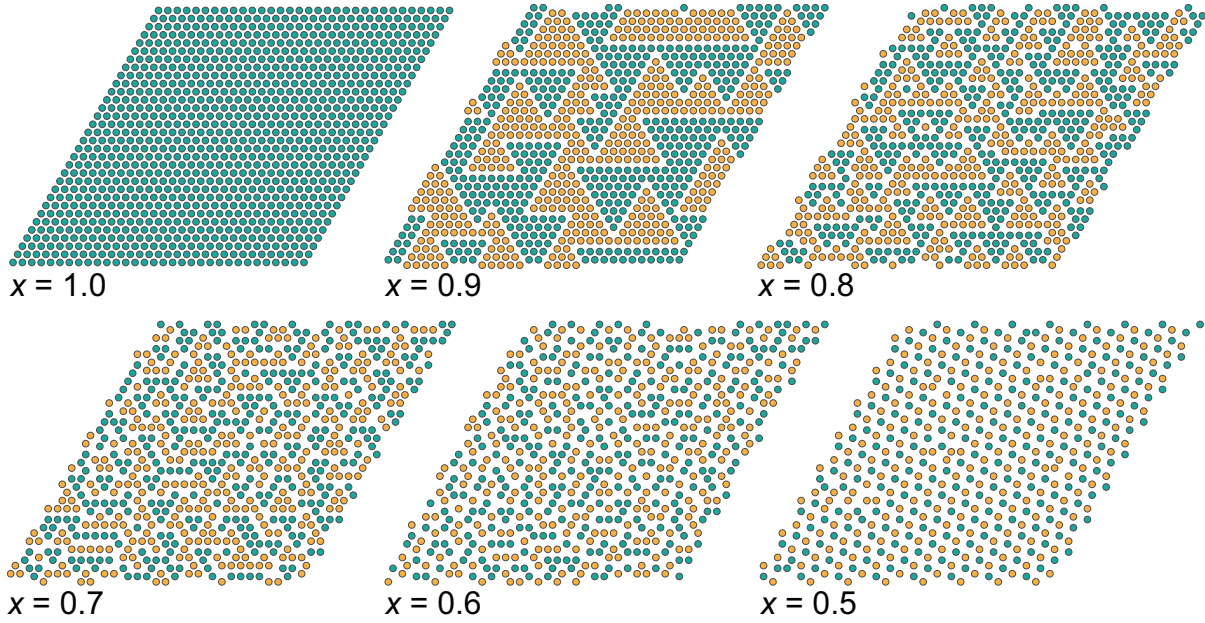
Figure 4.6: Snapshots from constant chemical potential, decreasing temperature grand canonical Monte Carlo runs for the P3 structure at 300 K, looking down on one of the Na layers. The two different available sites on the honeycomb lattice are shown in green and yellow. Approximate Na concentration at each snapshot is indicated below the snapshot.

in the microstates sampled at $x = 0.9$ and $x = 0.8$, more disorder is observed as the Na concentration approaches $x = 0.7$. Triangular domains are still distinguishable around $x = 0.7$, but there are also many linear chains of Na occupying the same sublattice (A or B). Short-range order persists at $x = 0.6$, although at this concentration short chains of A or B sublattice occupation seem to be preferred. The Na ions order in their DFT ground state pattern at $x = 0.5$, exhibiting occasional defects due to thermal excitations. They disorder at temperatures slightly above that of room temperature. The in-plane Na ordering at $x = 0.5$ (Fig. 4.2(f) is also stable in the P3 layers of O1-P3 at $x = 0.25$ and matches the ordering inferred from single-crystal diffraction data by Hibma [65]. Hibma also reports on the existence of diffraction superlattice spots together with rings above $x = 0.5$. Our MC simulations predict a solid solution at room temperature above $x = 0.5$.

The MC snapshots of Fig. 4.6 illustrate that Na extraction from P3 occurs very differently from other host structures such as O3 and O1. A sloping voltage profile usually signifies a solid solution characterized by uniform disorder among cations and vacancies. In contrast, the sloping voltage profile of P3 is produced by Na arrangements consisting of ordered nano-sized domains separated by APBs, where changes in Na concentration lead to an overall increase in total APB length. Fig. 4.5(b) shows that the voltage profile of the P3 phase is steeper than that of O3. This qualitative behavior is similar to that exhibited by many other layered Na intercalation compounds with O3/P3 transformations [42–44, 49, 53].

4.4 Discussion

Our first-principles study shows that intercalation in Na$_x$TiS$_2$ is very different from that in the traditional Li-ion battery materials in at least two ways. First, stacking-sequence changes are much more prevalent in Na$_x$TiS$_2$ due to the stability of P3 and its hybrids at intermediate compositions. Second, the devil's staircase of triangular domains on the Na honeycomb lattice of P3 is fundamentally unlike the types of orderings seen in Li layered oxides.

We hypothesize that the behavior of Na$_x$TiS$_2$ may be representative of many other intercalated layered oxides and sulfides. This is supported by the observation of transformations from O3 to P3 upon desodiation in a wide range of compounds, including Na$_x$VS$_2$ [52, 84], Na$_x$CoO$_2$ [42, 48], Na$_x$NiO$_2$ [53], Na$_x$Ni$_{0.5}$Mn$_{0.5}$O$_2$ [44, 46], Na$_x$CrO$_2$ [42, 44, 49], Na$_x$Mn$_{1-y}$Fe$_y$O$_2$ [47], and Na$_x$Fe$_{0.5}$Co$_{0.5}$O$_2$ [48]. Furthermore, many Na compounds (e.g., Na$_x$CoO$_2$, Na$_x$CrO$_2$, and Na$_x$VS$_2$) exhibit voltage curves strikingly similar to that predicted for Na$_x$TiS$_2$. The general pattern seems to be:

1. As deintercalation begins, the voltage curve exhibits a relatively flat region around

$0.7 < x < 1$ associated with the deintercalation of O3 and transformation to P3.

2. The $0.4 < x < 0.7$ composition range is typically a P3 single-phase region that exhibits a steep slope. The steepness of the slope is a consequence of the high curvature of the P3 free energy, as can be seen in Fig. 4.5(a). The high curvature can be attributed to the strong stabilization of the honeycomb lattice at intermediate concentrations.

3. Around $x = 0.5$, a sharp voltage step occurs, possibly corresponding to a zig-zag ordering like that shown in Fig. 4.2(d). (This step is often reported at Na contents somewhat above $x = 0.5$, which may be due to the experimental uncertainties in estimating the Na content or the thermodynamic stability of another ordering having a slightly higher Na concentration. [83])

4. Deintercalation beyond $x = 0.5$ exhibits a plateau associated with the transformation of P3 to another stacking sequence. While we are not aware of any experimental observations of staged O1-P3 hybrids at high states of charge in oxides, the results of this study suggest that their occurrence in Na transition-metal oxides could be a possibility at low Na concentrations when the P3 host is also stable at intermediate Na concentrations. Furthermore, stacking sequences at very low Na concentrations may include higher-ordered staged phases as suggested by experiments of Na$_x$TiS$_2$ [63, 65].

Although many of these materials exhibit additional phase transformations associated with Na/vacancy ordering, the similarities in the structural transformations and overall shape of the voltage curve suggests that these materials share the same basic intercalation physics as Na$_x$TiS$_2$. Furthermore, although Li and Mg are unstable in prismatic coordination due to their small ionic sizes, larger intercalating ions such as K$^+$ and Ca^{2+}

may behave similarly to Na in layered compounds. Nevertheless, some Na oxides do not transform to P3 even when their equivalent sulfides are stable in the P3 host. For instance, NaTiO$_2$ is more stable in O3 than P3 even upon deintercalation [55]. This may be a result of increased ionicity in oxides due to higher electronegativity of oxygen versus sulfur [38,85].

Transformations between O1, O3, P3, and hybrid phases requires stacking-sequence changes during cycling and likely affects battery performance. As was pointed out by Gabrisch et al. [86], partial dislocations are one mechanism to mediate stacking-sequence changes in layered intercalation compounds. Stresses generated by an array of partial dislocations and by a lattice mismatch across interfaces can contribute to fracture and mechanical degradation. Hybrid phases that nucleate separately and grow into each other may be misaligned, leading to additional sources of stress at their interface.

The honeycomb lattice of Na sites within P3 leads to several interesting properties. At high Na concentration, narrow bands of A and B domains appear in the P3 ground-state orderings calculated with DFT (Fig. 4.2(g,h)). We can distinguish between three unique Na coordination environments along the APBs in these orderings. Type I APB, shown in Fig. 4.7(a), consists of third-nearest-neighbor Na pairs perpendicular to the APB. The APBs that make up the edges of the triangular domains in the MC simulations are type I. Triangles are formed because this type of APB has three symmetrically-equivalent orientations. Type II APBs are made up of fourth-nearest-neighbor pairs (Fig. 4.7(b)), but this type of boundary is not seen in MC snapshots and is therefore not thermodynamically favorable. When every other atom along a type II APB hops across the boundary, a type III APB forms (Fig. 4.7(c)). The local Na environment along a type III APB is similar to that observed at corners of triangular domains in MC snapshots.

Others have studied ground states of the devil's staircase on a honeycomb. Kanamori
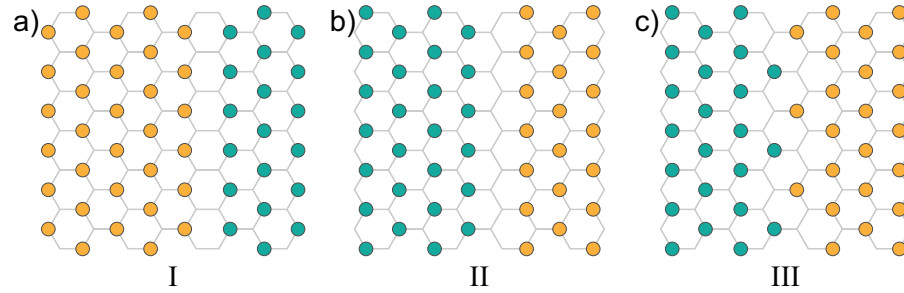
Figure 4.7: Different types of Na coordination observed along APBs in low-energy orderings found using DFT. (a) Type I ordering is observed along APBs in MC simulations. (b) Type II ordering is not observed in MC simulations. (c) Type III ordering is similar to that observed at corners of triangular domains in MC simulations.

used a simple lattice model Hamiltonian and discovered an infinite series of ground states on a honeycomb lattice with repulsive pairwise interactions [68]. More recently, Wang et al [69] used a short-range pair Hamiltonian to describe ground states in Na$_x$CoO$_2$, where they suggest two different patterns for arranging the triangular domains. Our MC snapshots most closely match the T series suggested by Kanamori. In all of these cases, however, only type I APBs are predicted as separating perfectly ordered domains.

Diffusion mechanisms in the P3 host are qualitatively different from those in other layered intercalation compounds. While the O3 and O1 hosts have a network of inter-connected octahedral and tetrahedral sites within the intercalation layer, the P3 host only provides trigonal prismatic sites. A cation in O3 or O1 migrates between two adjacent octahedral sites by passing through an intermediate tetrahedral site [41]. In P3, cations hopping between nearest-neighbor sites on the same triangular sublattice of the honeycomb lattice (e.g. nearest-neighbor pairs on the A sublattice) will pass through a nearest-neighbor prismatic site on the other sublattice (i.e. the B sublattice) [61] as illustrated in Fig. 4.8(a).

Vacancies are crucial in facilitating ionic transport in layered intercalation compounds. In fact, in many intercalation compounds, both the qualitative nature of the hop mechanism and the hop rate itself are very sensitive to the local concentration and

arrangement of vacancies [41]. A Na ion that migrates into an isolated vacancy within a single-domain region within P3 must pass through the intermediate prismatic site that shares a face with another occupied prismatic site, as illustrated in Fig. 4.8(a). This leads to a high-energy nearest-neighbor repulsion along the hop path, making single vacancy hops less favorable than hops in local environments where such nearest-neighbor Na-Na interactions can be avoided.

Unlike in the O1 and O3 hosts, where divacancies are essential for fast diffusion, the presence of a pair of vacancies within perfectly ordered triangular islands in P3 is unlikely to be much more effective than isolated vacancies in mediating long-range Na diffusion. As illustrated in Fig. 4.8(b) a divacancy on a honeycomb lattice is essentially pinned spatially and requires single-vacancy-type hops involving nearest-neighbor Na-Na interactions to redistribute Na ions over long distances. Due to the topology of the honeycomb lattice, only one Na can hop into a divacancy without passing through a site that involves a Na-Na nearest-neighbor interaction (Fig. 4.8(b)(i)). Upon completion of this hop, only that same Na can perform a subsequent hop that does not involve a Na-Na nearest-neighbor interaction. It has two options then. It can either migrate to the second vacancy (as illustrated in Fig. 4.8(b)(ii)) or it can hop back to its initial position. If limited to migration paths that avoid nearest-neighbor Na-Na interactions, the divacancy twirls around a single axis without mediating long-range transport of the migrating Na. It is only after another Na performs a hop that requires a nearest-neighbor Na-Na interaction, similar to that encountered in an isolated vacancy hop, that the divacancy can break away and spatially move.

It must be noted, though, that it is very unlikely that divacancies are long-lived within a single domain region as they can facilitate the nucleation of new islands. This is illustrated in Fig. 4.8(c). At least two vacancies are required for a Na atom to move from an A site to a B site in a single-domain A region without producing nearest-neighbor

pairs. Once initiated, a single point vacancy can be used to grow the B domain at the expense of shrinking the A domain and increasing the total length of APBs.

While Na hops in single-domain regions of P3 generally require passage through high energy sites that involve nearest-neighbor Na interactions, diffusion along APBs can avoid such sites. One possible diffusion mechanism along a domain edge is illustrated in Fig. 4.8(d). When no point vacancies are present, Na at the corner of a triangular island can easily migrate onto the other sublattice, allowing the subsequent Na atoms along the APB to migrate across the APB. One domain region then grows at the expense of the other and the total length of APBs decreases. This results in a point vacancy forming within a single-domain region to retain the same overall Na concentration.

At this point, the vacancy can take one of three paths. It can move back along the APB in a chain of low-energy steps to reverse the process (the reverse of the process that is illustrated in Fig. 4.8(d)). Alternatively, a single high-barrier hop would be required to move the vacancy around the corner of the perfectly ordered domain such that it can propagate along an adjacent APB on the same island. Lastly, the vacancy can migrate through a single-domain region via a series of high-energy hops to reach the edge or corner of another APB. Diffusion of the vacancy through a single-domain region may be slow if the domains are large. In all cases, the point vacancy at a corner or an edge of a triangle can quickly travel along the APB and be consumed as the total length of APBs increases. In this way, triangle islands can shrink and expand, and APBs can serve as sources and sinks for vacancies.

As the Monte Carlo microstates illustrate in Fig. 4.6, a decrease in the Na concentration within P3 results in the elongation of the total APB length, which is achieved by an increase in the number of single domain islands. The removal of Na therefore requires the nucleation of new islands and a decrease in the size of the existing islands. These are highly non-local readjustments to the overall Na arrangement. It is, therefore,

(a) Single vacancy
(b) Divacancy
(c) Island nucleation
(d) Diffusion along APB

● Na on A site   ● Na on B site   ☐ Na vacancy   ➤ Na migration path   ▮▮▮ Na nearest-neighbor pair
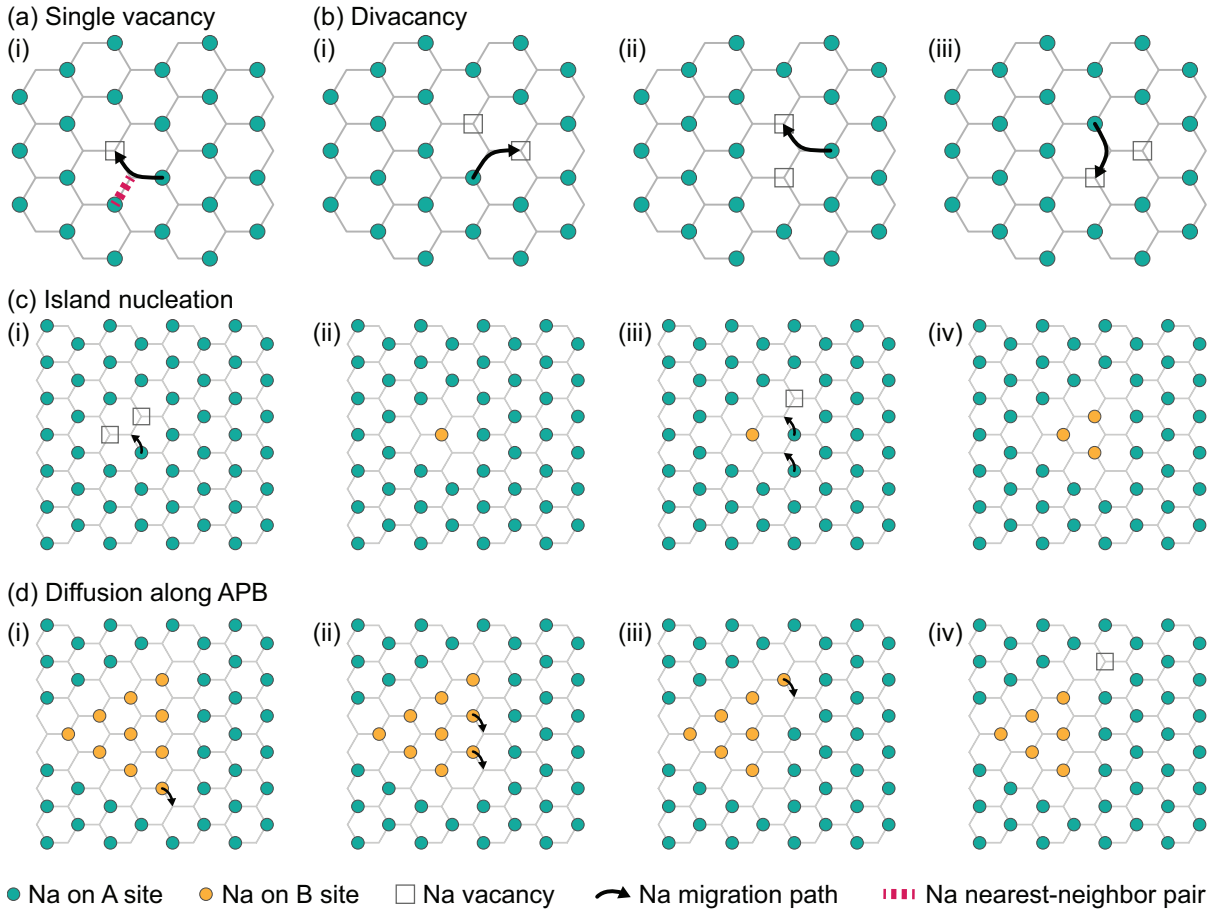
Figure 4.8: Various migration mechanisms of Na within the P3 host. (a) With an isolated vacancy, an atom must pass through an adjacent trigonal prismatic site that is next to an occupied Na site leading to an unfavorable nearest-neighbor Na-Na repulsive interaction. (b) A divacancy allows for one atom to hop around an axis, but it cannot migrate over an extended distance without invoking high-barrier hops through sites that have an occupied nearest neighbor. (c) A divacancy can aid in new island nucleation, and the island can then easily grow by absorbing isolated vacancies from the surrounding single domain region. (d) Domains can redistribute atoms by shifting antiphase boundaries. This mechanism generates (i → ii → iii → iv) or consumes (iv → iii → ii → i) a vacancy.

likely that metastable states that are kinetically more expedient are frequently accessed, especially during high rates of charge and discharge. This could lead to path hysteresis and polarization in the voltage profile; however, a kinetic study involving kinetic Monte Carlo would be necessary to elucidate these tendencies.

4.5   Conclusions

In this study, we used a first-principles statistical mechanics approach to examine two properties of the O1/O3/P3 family of Na-ion electrode materials: (i) the relative stability among different stacking sequences that include staged hybrid host structures and (ii) Na ordering tendencies in the P3 host. Using Na$_x$TiS$_2$ as a model system, we found that O1-O3 and O1-P3 hybrid structures are both stable at low Na concentration. The stability of these staged phases in Na$_x$TiS$_2$ suggests that they are likely to occur in other layered Na oxide and sulfide intercalation compounds, with important consequences for cycleability and charge/discharge rate capability. Our study also showed that ordering on the honeycomb in P3 not only allows this phase to be more stable than O3 at Na concentrations around $x = 1/2$ but also results in a devil's staircase of ground states at high Na concentrations (including regions where P3 is stable). These ground states consist of perfectly ordered triangular islands separated by antiphase boundaries. Elementary considerations show that the antiphase boundaries may play a crucial role in mediating long-range Na diffusion within the P3 host.

Acknowledgments

Chapter 5

$Na_x TiO_2$

Having thoroughly explored Na orderings in the $Na_x TiS_2$ system, we turn to its oxide counterpart and find that the change in anion has monumental impact on phase stability. $Na_x TiO_2$ has been proposed as an anode material for Na-ion batteries since graphite, which is often used in Li-ion batteries, does not reversibly intercalate Na. Experimental studies have shown good reversibility within the $1/2 < x \leq 1$ limit, which may be due to the lack of O3 to P3 phase transitions that usually plague Na-intercalating transition-metal oxides around the $x = 1/2$ composition. We use density functional theory and grand canonical Monte Carlo methods to explore Na orderings in the O3 $Na_x TiO_2$ system. We find a series of unique orderings that can explain the features observed in previous experimental studies. We also find that the P3 structure may be stable at low Na compositions. The unique orderings and surprising P3 stability region could have implications for alloying Ti into other transition-metal oxide systems.

5.1 Introduction

The anode of a Na-ion battery requires some attention. While Na metal is often used as the anode to test Na-ion battery electrodes, it is not a good candidate for commercial applications due to formation of dendrites, high reactivity with water, and fairly low melting temperature [87]. Furthermore, Na does not readily intercalate into graphite [88,89], a common anode material in Li-ion batteries. Other forms of carbon have been explored but can suffer from low energy density and voltage approaching 0 V vs. Na/Na$^+$ [87,90], which could result in Na-metal dendrite formation.

Fortunately, Na deintercalation from O3 NaTiO$_2$ (first synthesized by Hagenmuller, et al. [91]) occurs in the voltage window between 0.6 V and 1.6 V versus Na metal to make it a promising anode material. Previous experimental work has shown up to 150 mAhg^{-1} reversible capacity, though the material is limited to about half of its theoretical capacity by an irreversible phase transition just above 1.6 V [55, 92, 93]. The good reversibility at high concentrations of Na is partially due to a lack of significant structural phase transitions and small volume changes in this composition range [55]. Unlike many other Na-intercalating O3-type layered transition-metal oxides and sulfides (e.g. Na$_x$TiS$_2$ [34] or Na$_x$CoO$_2$ [94]), Na$_x$TiO$_2$ does not transition into the P3 stacking sequence at intermediate Na concentrations. At the same time, *in situ* results from Wu, et al. [55] show a prominent, reversible hexagonal to monoclinic phase transition, which may be a result of Na ordering.

We have found that there is variability in capacities reported in literature. The earliest experiments by Maazaz, et al. [92] show a step in the voltage at around $x = 0.87$ with reversible cycling between $0.7 < x < 1$. More recent experiments show a similar step around $x = 0.69$ [93] or $x = 0.66$ [55]. Furthermore, Pérez-Villa, et al. [93] noted that the capacity obtained is highly sensitive to the amount of excess Na present during

synthesis as this dictates the amount of NaTiO$_2$ formed. Deviations in the amount of product synthesized can make it difficult to determine the amount of active material in the electrode, making estimates of the amount of Na deintercalated unreliable. Therefore, identifying the members of the phase transition and orderings formed during cycling would aid not only in better understanding this material but also in more accurately quantifying the synthesis of the active material.

In this regard, computation can be a useful tool. While there have been many computational and experimental studies to describe the high to low temperature phase transition in the NaTiO$_2$ end member [95–97], there have been no thorough studies of Na deintercalation from this material. Toumar, et al. [82] completed a high-throughput study of Na orderings in seven first-row transition-metal oxides, including Ti. However, their ground-state orderings do not show clear candidates to describe the experimental voltage curves. A different computational study [98], focusing largely on Na intercalation into TiO$_2$ hollandite, included a very limited set of calculations on layered O3 Na$_x$TiO$_2$, but, once again, the results did not conclusively explain experimentally observed behavior.

In this work, we conduct a thorough computational analysis of O3 Na$_x$TiO$_2$, both via DFT at 0 K and Monte Carlo with added configurational entropy to simulate finite temperatures. We discover a surprising set of previously unreported ground-state Na orderings for this system. Two orderings stand out as stable phases even at simulated room temperatures, one at $x = 3/4$ and another at $x = 7/12$. Furthermore, an interesting set of orderings emerge during the transition between $7/12 \leq x \leq 3/4$. To put the orderings on the O3 structure into context, we also calculate a number of other low-energy structures and a limited set of potential orderings along the P3 Na$_x$TiO$_2$ hull. We find that while the P3 stacking sequence is slightly less stable than O3 for $x \geq 1/2$, it may become more stable at lower compositions if the layered structure could be maintained at higher voltage.

5.2   Methods

The energies of different Na$_x$TiO$_2$ structures were calculated using density functional theory (DFT) as implimented in the Viena Ab initio Simulation Package (VASP) [24,25]. We used the Na_pv, Ti_sv, and O PAW_PBE pseudopotentials [70,71] and the optb86b-vdw functional [72–75]. A fully automatic 38 Å k-point mesh density was applied, and the energy cutoff was set to 530 eV. Energies are reported per formula unit (f.u.), which we define as Na$_x$TiO$_2$.

The energies of multiple structures were calculated in this work, as shown in Fig. 5.1. For the O3 and P3 structures, configurations at various Na concentrations were calculated, in the range of $0 \leq x \leq 1$ in Na$_x$TiO$_2$. At composition $x = 0$, the O1, anatase, and rutile structures were calculated. For the $x = 1/2$ composition, the two lowest energy structures from the Materials Project [99] at this composition were calculated, namely the spinel structure and the CaV$_2$O$_4$-type structure (Pnma spacegroup, as first reported by Akimoto and Takei [100]).

For the O3 system, we calculated all configurations in supercells up to volume six of the Na$_x$TiO$_2$ primitive cell. For supercells above volume six, we used a recursive method of fitting a cluster expansion to our data and calculating configurations that had predicted energies below or close to the cluster expanded hull. This resulted in almost 200 configurations between volumes six and sixteen, focusing on the composition range $1/2 \leq x \leq 1$. During ionic relaxation, some configurations underwent drastic structural distortions. When possible, these configurations were reassigned to the appropriate host structure; otherwise, they were discarded. We found that many configurations that contained empty Na layers often underwent drastic distortions during relaxation or did not reach set convergence criteria. Since the cluster expanded energies of the unconverged configurations were more than 50 meV/f.u. above the hull, we left them out of our
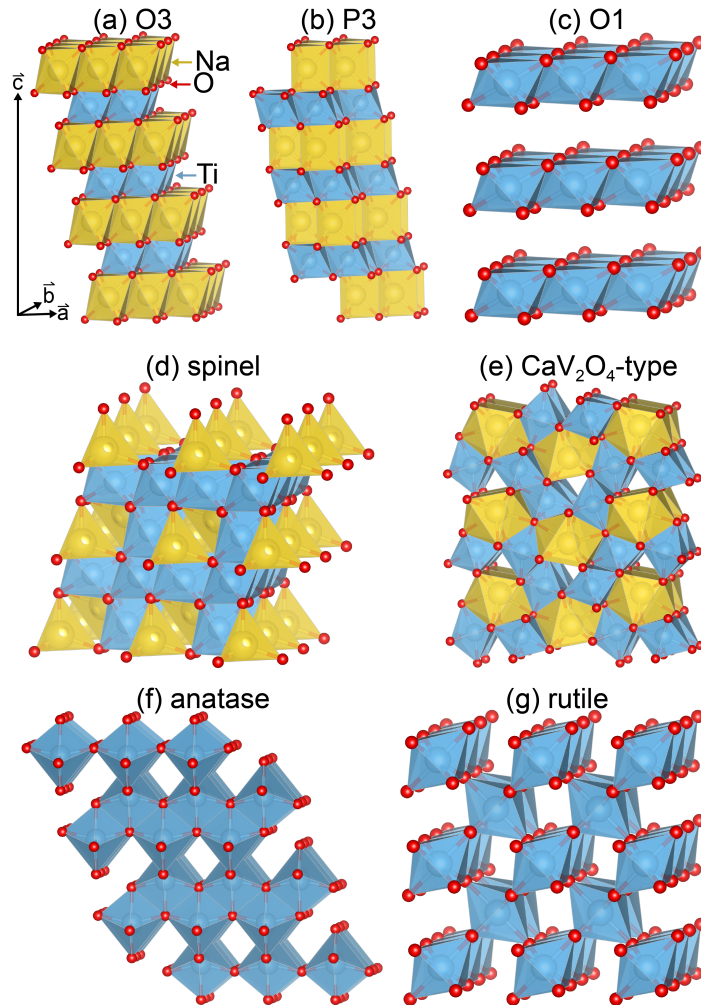
Figure 5.1: Na$_x$TiO$_2$ structures calculated in this work. Red circles depict O atoms; yellow and blue polyhedra show Na-O and Ti-O coordination, respectively. Images produced using VESTA software [10].

analysis.

A cluster expansion was fit to 447 calculated O3 configurations using Clusters Approach to Statistical Mechanics (CASM) [27–30] software. The cluster expansion has the basis set $\sigma_{Va} = -1$ and $\sigma_{Na} = 1$ and consists of 25 terms with up to four points per cluster. The goodness of fit parameters for the cluster expansion are as follows: the root-mean-square (RMS) of the data set for the entire composition range is 12 meV/f.u. The weighted RMS (wRMS), where configurations near the hull and in the range $1/2 \leq x \leq 1$ have larger weights, is 3 meV/f.u.

A dense grid of constant μ, increasing T MC simulations were run in the chemical potential range $1/2 \leq x < 1$ to determine the single phase and solid solution regions, followed by constant T, changing μ MC simulations. To obtain the energies of configurations in the solid solution regions, at least one ground state within the region was integrated from 10 K to 300 K, 400 K, or 500 K. We used the energy integration method described in Ch. 3 to obtain Gibbs free energies and finite temperature voltage curves at finite temperatures.

5.3 Results

5.3.1 DFT calculations

The formation energies for O3 configurations relative to the $x = 0$ and $x = 1$ O3 endpoints are shown as blue circles in Fig. 5.2. The black line is the convex hull and indicates the O3 ground-state configurations along the composition range. To put the O3 structure into perspective with the global energy landscape, we calculated two other common stacking sequences in the O3 family, O1 and P3, as wells as some non-layered, low-energy structures with Na$_x$TiO$_2$ composition.
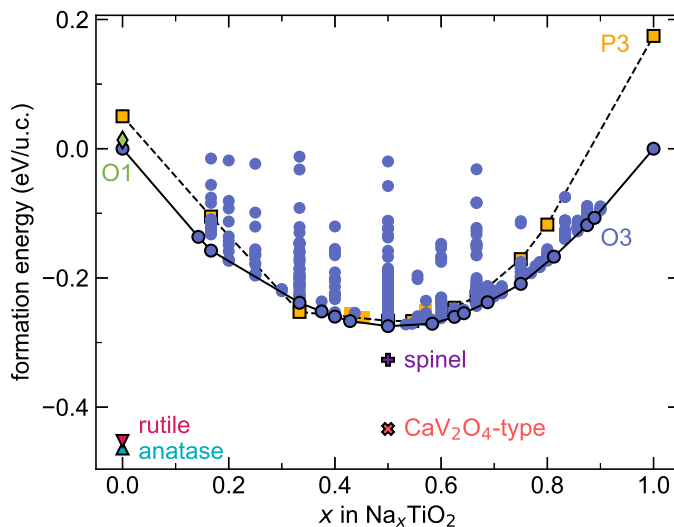
Figure 5.2: Calculated DFT energies of Na$_x$TiO$_2$ where formation energy is relative to the O3 configurations at $x = 0$ and 1. Each point corresponds to a configuration. The hulls of O3 and P3 are shown in solid and dashed black lines, respectively.

A limited number of configurations were calculated for the P3 structure, including most ground states previously found for Na$_x$TiS$_2$ [34], Na$_x$CoO$_2$ [94], and K$_x$CoO$_2$ [101]. As predicted by experiment [55, 92], the P3 structures are not stable at compositions $x \geq 1/2$, though the energies are close to the hull at intermediate Na concentrations. Surprisingly, there appears to be a P3 configuration below the O3 hull at $x = 1/3$. This configuration has a $\sqrt{3} \times \sqrt{3}$ in-plane ordering of Na atoms and a two layer unit cell such that each Ti atom is face-sharing with no more than one Na atom. This is in contrast to the lowest energy O3 configuration at this composition, which has pairs of Na in a $\sqrt{3} \times \sqrt{3}$ grid. Configurations with evenly distributed Na atoms in the O3 structure are at least 11 meV/f.u. above the O3 hull. The number of O3 configurations calculated in the low composition region is not as extensive as for $x \geq 1/2$, so there may be other O3 structures with lower energies. While layered Na$_x$TiO$_2$ has been found to irreversibly transform to other structures outside the O3 family at low Na compositions, the theoretical stability of P3 over O3 at low Na concentrations may be indicative that

alloying other layered oxides with Ti may increase the stability of the P3 structure at low compositions.

There are other structures that compete with the O3 and P3 layered phases as Na is removed from the structure. We have plotted several candidate structures in Fig. 5.2. The O1 structure, a common phase at $x = 0$ for many layered transition-metal oxides, is not stable for TiO$_2$. However, rutile and anatase are considerably lower in energy at this composition, as may be expected. As for many oxides, the spinel structure with Na in tetrahedral sites is below the O3 convex hull at $x = 1/2$. Even lower in energy is the orthorhombic CaV$_2$O$_4$-type structure. Although the global convex hull would suggest that a phase transition to the CaV$_2$O$_4$-type structure should occur at the very beginning of Na deintercalation from NaTiO$_2$ based on thermodynamics, the material has been shown to cycle reversibly across about half of the composition range, suggesting that kinetic limitations may prevent phase transitions that require significant atomic rearrangement. Once much of the Na is removed, however, interlayer migration of Ti could occur, facilitating irreversible transitions to non-layered structures.

5.3.2   Na ordering in O3

The in-plane Na orderings of configurations along the O3 hull for $x \geq 1/2$ are shown in Fig. 5.3. Looking down on the Na layer, the Na atoms, yellow circles, are shown in the idealized positions on the triangular lattice. The positions of the Na atoms in the relaxed structures are slightly shifted within the Na-O octahedra, which is not reflected in this figure.

At high Na compositions, Na vacancies are accommodated as point vacancies. As composition decreases, the ground states between $3/4 \leq x \leq 7/8$ appear to have a distinctive row ordering. The $x = 3/4$ row ordering was previously calculated to be the
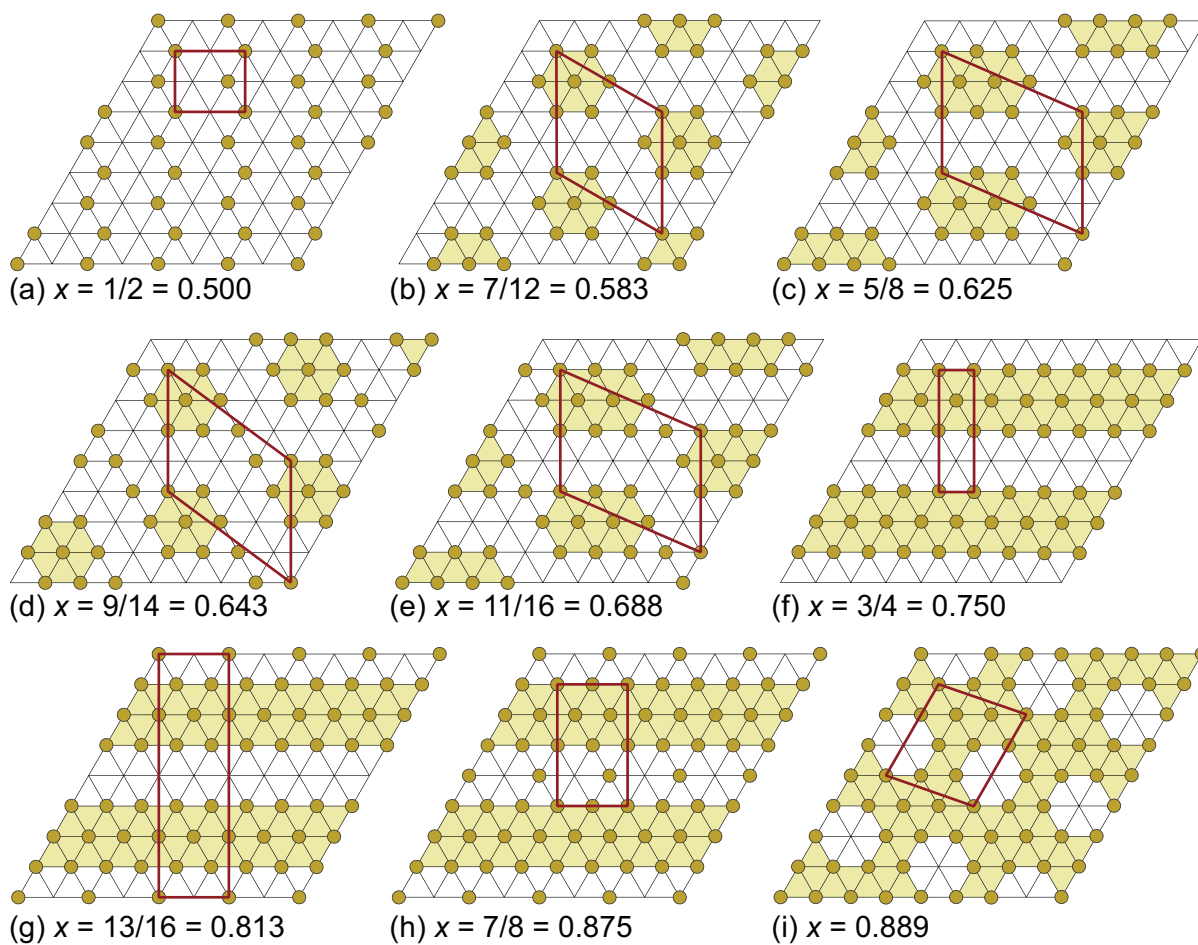
Figure 5.3: In-plane Na orderings along the O3 Na$_x$TiO$_2$ convex hull, looking down on the Na layer. The yellow circles are Na atoms and the red lines indicate in-plane repeat unit. The yellow background is used as a guide for the eye.

ground state by Toumar, et al. [82] For $7/12 \leq x < 3/4$, we find a set of new ground states that appears to have a perpetuating theme of Na ordered into hexagons.

There is no clear ground state at $x = 2/3$, but a configuration with Na in a hexagonal pattern (Fig. 5.4(a)) is only 0.2 meV/f.u. above the hull, which can be considered on the hull within our DFT margin of error. Surprisingly, the common $\sqrt{3} \times \sqrt{3}$ ordering (Fig. 5.4(b)) is 13 meV/f.u. above the hull, and the row ordering reported as the ground state at $x = 2/3$ by Toumar, et al. [82]) (Fig. 5.4(c)) is 22 meV/f.u. above the hull based on our calculations.

(a) $x = 2/3 = 0.667$
2 meV/u.c. above hull

(b) $x = 2/3 = 0.667$
13 meV/u.c. above hull

(c) $x = 2/3 = 0.667$
22 meV/u.c. above hull

(d) $x = 1/2 = 0.500$
2 meV/u.c. above hull

(e) $x = 1/2 = 0.500$
3 meV/u.c. above hull
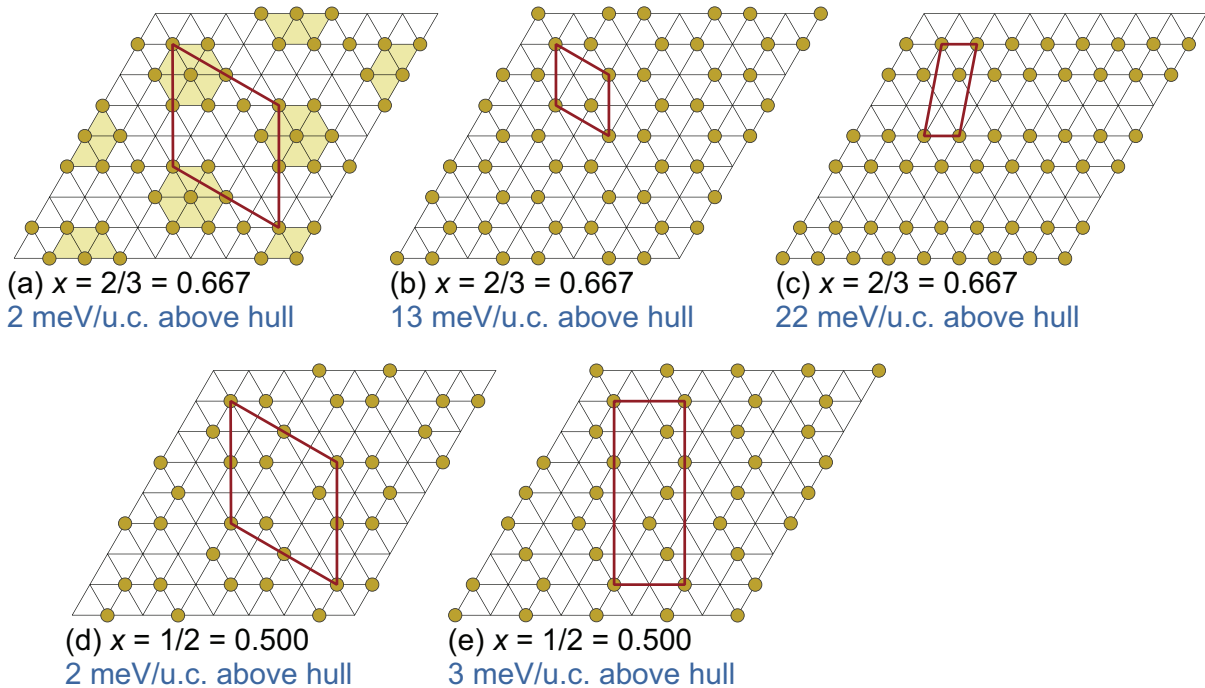
Figure 5.4: In-plane Na orderings for select O3 configurations. Energy above the O3 hull is indicated below each configuration. The yellow circles are Na atoms and the red lines indicate in-plane repeat unit. The yellow background is used as a guide for the eye.

The expected zig-zag ordering is stable at $x = 1/2$. There were two other O3 configurations at this composition close to the hull, illustrated in Fig. 5.4(d) and (e). The lower energy configuration consists of hexagonally ordered Na and is less than 2 meV/f.u. above

the hull. The second configuration has a pattern similar to the zig-zags of the ground state and is 3 meV/f.u. above the hull.

The unique ground states of the O3 Na$_x$TiO$_2$ system can be partially explained by examining Na-Na interactions. We noticed that upon relaxation, Na in many of the configurations shifted slightly off the ideal triangular lattice sites away from neighboring Na atoms. For a few select configurations, we have illustrated the direction of the Na atom displacement away from the ideal triangular lattice with red arrows in Fig. 5.5. For the structures on the hull, all nearest-neighbor Na-Na bond lengths are increased by the displacement of the Na atoms, and the effect on bond length can be significant. Compared to the ideal lattice sites, the average nearest-neighbor Na-Na bond length after displacement is between 7% and 12% longer in the ground state configurations for compositions $1/2 \leq x \leq 3/4$ compared to the ideal lattice. On the other hand, the symmetry of the $\sqrt{3} \times \sqrt{3}$ ordering at $x = 2/3$ does not allow for displacement off the lattice sites since the in-plane forces (shown as dashed green arrows in Fig. 5.5) are evenly distributed around each Na. The in-plane lattice parameters of NaTiO$_2$ are generally larger than other first-row transition-metal oxides [45, 50, 55, 102–105]. As a result, the Na-O octahedra are larger and may allow for larger Na displacement. This could mean that systems with larger in-plane lattice parameters may stabilize configurations that allow for larger Na displacements, though this effect remains to be investigated.

5.3.3 Monte Carlo simulations

We used grand canonical Monte Carlo (MC) to simulate voltage curves at temperatures 300 K, 400 K, and 500 K. Fig. 5.6 shows previously reported first charge experimental voltage curves alongside our calculations. The experimental results from Wu, et al. [55] and Pérez-Villar, et al. [93] both show a single broad step around composition

(a) x = 1/2
on hull

(b) x = 7/12
on hull

(c) x = 2/3
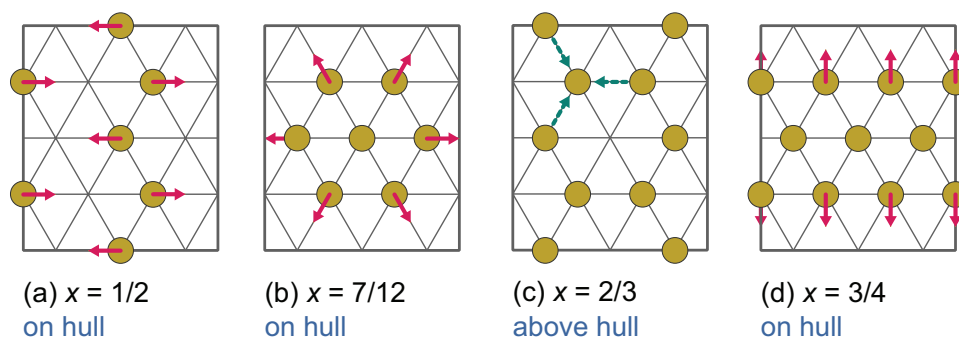above hull

(d) x = 3/4
on hull

Figure 5.5: In-plane Na ordering of select configurations. Ideal positions of Na atoms are shown as yellow circles, and the direction of their displacement upon relaxation is indicated with red arrows. The blue arrows in panel (c) show that the symmetric forces exerted on each Na atom by the others does not allow Na to displace away from their neighbors, resulting in close nearest-neighbor bonds.

$x = 0.64$ to $x = 0.68$, with a plateau around 1 V. The voltage curve from Maazaz, et al. [92] appears quite different with two plateaus: one around 1 V, another around 1.6 V. The voltage step at high sodium composition likely corresponds to the step observed in the other two experiments, as they all report a hexagonal to monoclinic phase transition at that point. This would correspond to measuring lower capacity per active material, which could be due to synthesizing less product than expected. The second step at high voltage may be the irreversible phase transition that limits practical capacity.

At low simulated temperatures, our curves contain several features. At 300 K and 400 K, two steps appear to be most dominant: one at $x = 7/12$ and one at $x = 3/4$. The orderings at these steps resemble the ground-state configurations depicted in Fig. 5.3. Between the two steps there is a solid solution region and a plateau. Monte Carlo snapshots (Fig. 5.7) reveal that there exists an interesting pathway of transformation between configurations at $x = 7/12$ and $x = 3/4$. The sloping region from $x = 7/12$ to $x = 2/3$ accommodates increasing Na content by filling in sites between the isolated hexagons of the $x = 7/12$ configuration (Fig. 5.7(a) to (b)). Beyond the $x = 2/3$ composition, the hexagons appear to "expand", resembling small regions of the row ordering
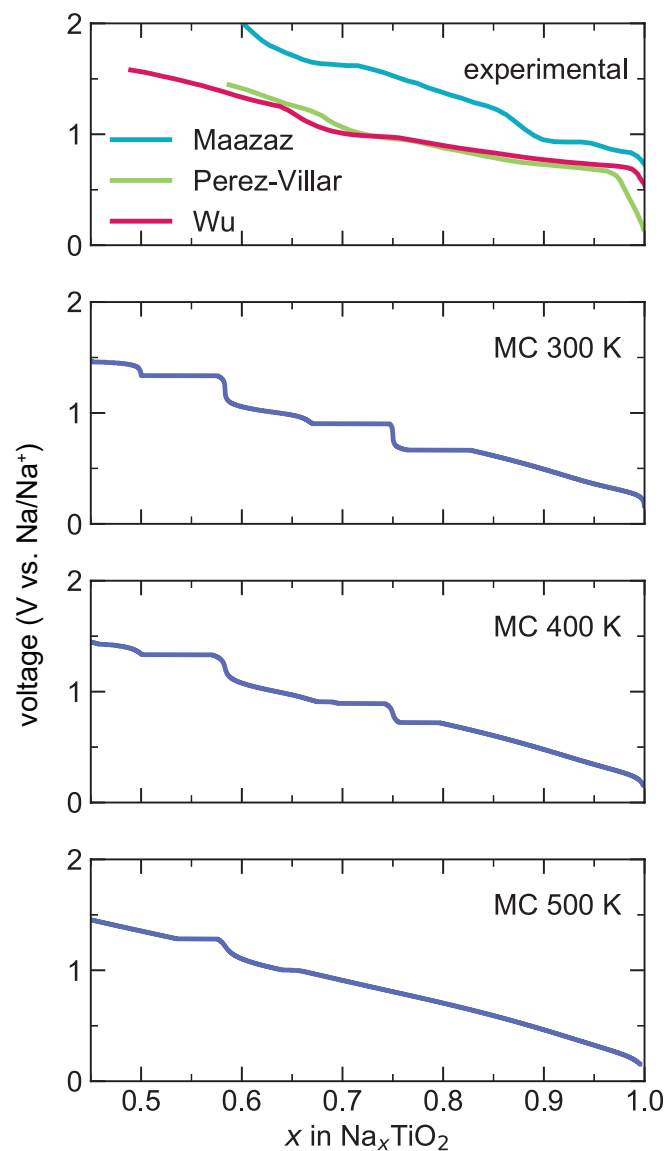
Figure 5.6: (top) Reported voltage curves for first charge of NaTiO$_2$. Curves have been digitized from Maazaz [92], Pérez-Villar [93], and Wu [55]. (bottom three) Voltage as a function of changing Na concentration in O3 NaTiO$_2$ as simulated using Monte Carlo (MC) and calculated from Gibbs free energy. Simulations at three different temperatures, as indicated.

separated by anti-phase boundaries (APBs). The APBs accommodate vacancies, so with increasing Na composition, the density of APBs decreases, eventually leading to the row ordering at $x = 3/4$. There appears to be a devil's staircase of orderings with decreasing APB density from $x = 2/3$ to $x = 3/4$. Although MC simulations indicate low energies for this series of orderings, they may be difficult to access continuously since they require the simultaneous rearrangement of many Na atoms as the concentration changes.

(a) x = 0.585 μ = 0.180   (b) x = 0.668 μ = 0.426   (c) x = 0.697 μ = 0.460

(d) x = 0.706 μ = 0.444   (e) x = 0.725 μ = 0.454   (f) x = 0.750 μ = 0.556

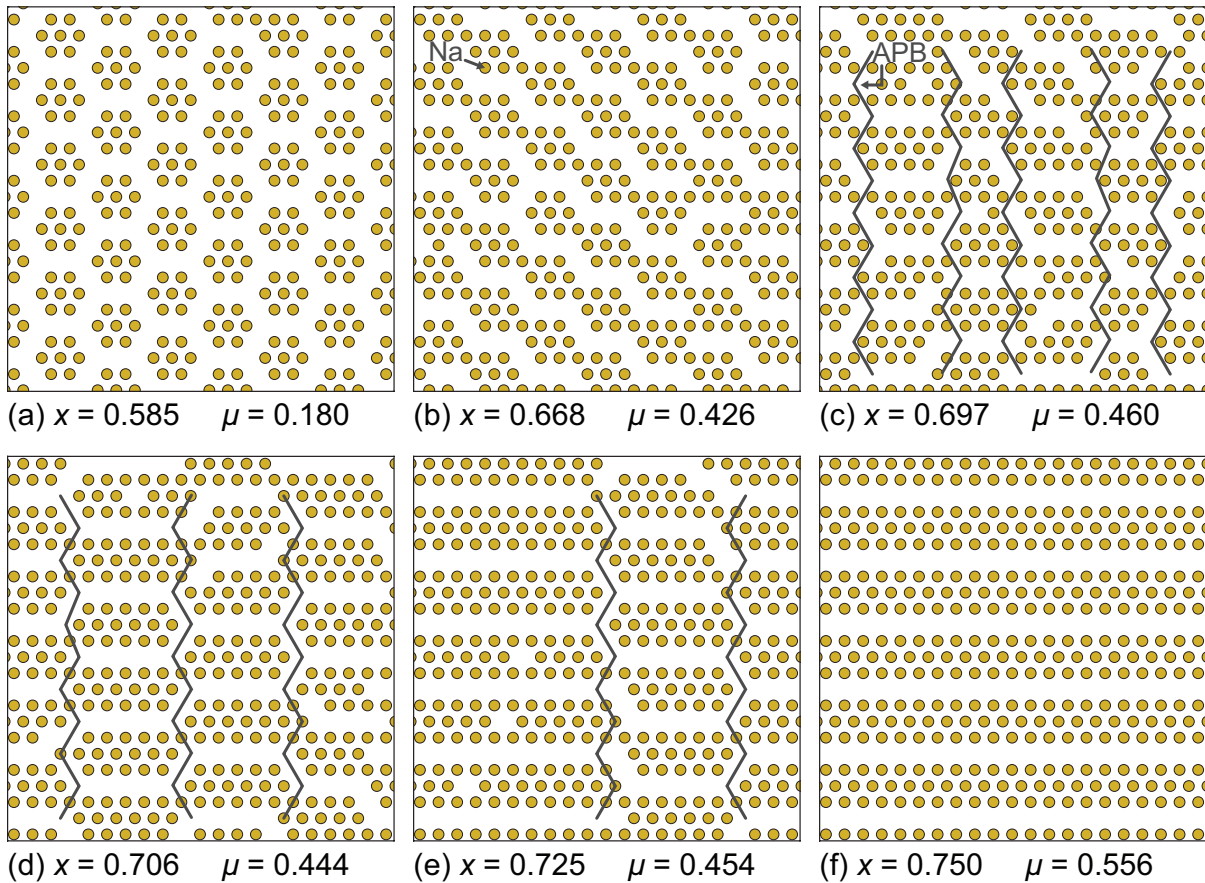Figure 5.7: Snapshots from MC at 400 K, looking down on a single layer of Na (yellow circles). All configurations are either on the hull or very close.

The MC voltage curve at 500 K reveals that the step at $x = 3/4$ is the first to disorder with increasing temperature, resulting in a single step at $x = 7/12$ with solid solution regions to either side. Of the three temperatures, the shape of the MC voltage curve at

500 K most closely resembles the experimental curves, and the plateau to the right of the step appears at the same voltage, around 1 V. One difference is that the MC solid-solution region at high Na concentration is more steep than those reported experimentally, though this could be an artifact of kinetics or other factors not captured by MC. Second, the composition at which the step occurs is different between the calculated and experimental results. If the voltage step observed experimentally does correspond to the $x = 7/12$ ordering, then the capacity reported is underpredicted by some 15%.

5.3.4   Structural characteristics

To further aid in the characterization of the voltage step, we have compared the structural characteristics of our calculated data set with reported experimentally measured values from Wu, et al. [55] We have calculated the interlayer spacing and in-plane lattice parameters of all configurations and have compared them to experimental results, as shown in Fig. 5.8. The red points are experimental measurements, while the colored points ranging yellow to blue are the calculated values from DFT relaxed structures with the color corresponding to the energy above the convex hull. Points corresponding to configurations on the calculated hull are outlined in black. The interlayer distance is the average distance between Ti layers. The in-plane lattice parameters are determined based on strains when the relaxed configurations are mapped onto the primitive (hexagonal) unit cell. The a and b in-plane lattice parameters diverge after the hexagonal to monoclinic phase transition, so we plot only the average of the two for all configurations but indicate both for ground-state configurations. At the $x = 1$ composition, the interlayer distance is overpredicted by about 1.2%, while the in-plane parameters are underpredicted by 2.4%. The difference between measured and predicted lattice parameters decreases with decreasing Na concentration.

Experimental results show a discontinuity in the interlayer spacing centered around $x = 0.75$. There is also a jump in interlayer spacing in our calculated structures between $x = 13/16 \approx 0.8$ and $x = 3/4$. In-plane lattice divergence in the high Na concentration range is irrelevant as disordering of Na at finite temperatures would affect the lattice parameters, likely resulting in a value close to the average of multiple configurations at that composition and retention of hexagonal symmetry. The average a and b lattice parameters diverge after $x = 3/4$, though the $x = 3/4$ does have the C2/m monoclinic symmetry. It is possible that this change in symmetry corresponds to the observed hexagonal to monoclinic phase transition if the DFT energy for this configuration is slightly overpredicted.
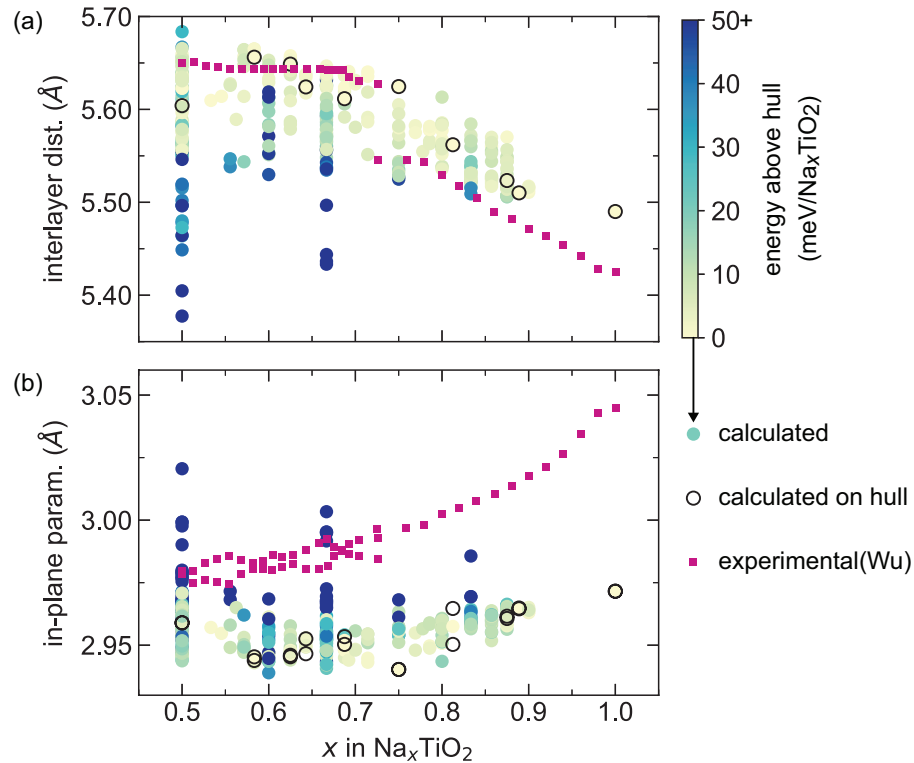

Figure 5.8: Comparing calculated interlayer spacing and in-plane lattice parameters of O3 Na$_x$TiO$_2$ with experimental measurements [55]. Interlayer spacing is defined here as the distance from one Ti layer to the next along a path orthogonal to the layer.

More accurate experimental measurements of the interlayer spacing in the monoclinic

region provided by Wu, et al. [55] surprisingly match the compositions of our ground states. Although the step at reported $x = 0.67$ appears to correspond to the calculated $x = 7/12$ configuration, a small change in curvature is present in the experimental voltage curve at $x = 0.58$, the composition corresponding to our hexagonal ordering. This surprising correspondence of the composition for the minor feature at $x = 0.58$ and the hexagonal configuration at $x = 7/12$ may suggest an alternative explanation. If the functional used in this work overpredicts the relative energy of the $x = 2/3$ hexagonal configuration relative to the ground states at $x = 7/12$ and $x = 3/4$, it is possible that the Na orderings formed along the composition range are still the same, but that the calculated step would shift from $x = 7/12$ to $x = 2/3$.

The experimental work by Wu, et al. [55] further characterized phase evolution upon charge using in situ X-ray diffraction (XRD), which we have simulated for our structures, shown in Fig. 5.9. We have labeled the calculated peaks (blue) based on the composition since voltage is often underpredicted with DFT. The experimental peaks (red) are identified based on the voltage at which they were measured, 0.7 V and 1 V, which correspond to the beginning of charge and the beginning of the hexagonal to monoclinic phase transition, respectively. Select regions with the largest peaks were chosen for comparison, and the dashed lines are included as a guide for the eye.

At the beginning of charge (Fig. 5.9(a) and (b)), the experimental and calculated peaks match well with respect to number and location. As can be expected, the peaks corresponding to the interlayer direction are slightly shifted to the left due to lattice parameter overprediction by DFT, while the opposite is true for the peaks that include in-plane directions. These shifts decrease at higher Na concentration where the predicted lattice parameters are more accurate to experiment. At the phase transition (Fig. 5.9(f)), the peaks at $2\theta = 7.5$ and 15.1 shift to the left corresponding to the drastic increase in interlayer distance. The two close peaks around $2\theta = 18.6$ further split as a result
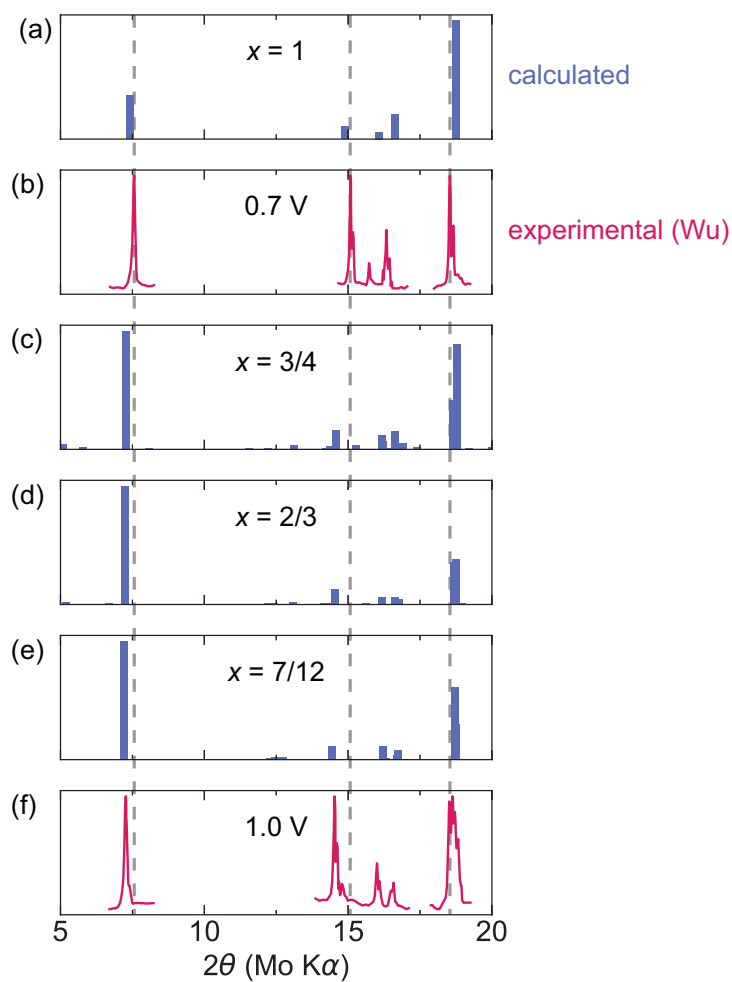
Figure 5.9: Simulated XRD patterns for DFT structures (blue) at $x = 1$, $x = 3/4$, $x = 2/3$, $x = 7/12$ and experimental XRD patterns from Wu, et. al [55] (red) at the beginning of charge (0.7 V) and at the plateau (1.0 V). The gray dashed lines are guides to the eye aligned with major experimental peaks of the pristine material.

of reduced symmetry in the monoclinic phase. In Fig. 5.9(c)-(e), we show simulated XRD patterns for three potential orderings that we have identified so far, namely the orderings at compositions $x = 3/4$, $2/3$, and $7/12$. The simulated XRD patterns all show the shift of $2\theta = 7.5$ and 15.1 peaks to the left and a slight split in the $2\theta = 18.6$ peak. The simulated patterns show the broad similarities between the different orderings and indicate that identifying the correct phases that participate in the transition may be difficult. Furthermore, disordering at any of these compositions would reduce peak splitting and shifts, resulting in XRD patterns that look more similar to the fully sodiated material.

5.4   Conclusions

With our calculations, we attempt to elucidate the origin of the phase transition observed when O3 NaTiO$_2$ is charged. Understanding this transition is important for several reasons. First, knowing the composition at which the transition occurs can allow for more accurate calculations of the electrode's capacity, state of charge, and perfor-mance. Second, identifying discrepancies between experimental and theoretical capacity can aid in identifying side reactions or reaction inefficiencies during synthesis, addressing either of which can help in improving performance and reducing cost. Finally, since the reversible capacity is quite drastically shortened by the transition to some other structure at intermediate Na concentrations, improving this material's performance as an electrode must undoubtedly involve identifying the destructive phase transition and determining methods to suppress it. Knowing the exact composition at which the transition occurs is instrumental in this respect.

While our results indicate that a particular Na ordering is likely responsible for the step observed in voltage, we cannot definitively identify whether the step is due to the

row ordering at $x = 3/4$, the hexagonal ordering at $x = 2/3$, or the hexagonal ordering at $x = 7/12$. Based on Monte Carlo, the $x = 7/12$ ordering appears to be the most likely candidate for the step as the simulated voltage curve at 500 K qualitatively matches those measured experimentally. Meanwhile, the $x = 2/3$ ordering best matches the experimental composition of the step and would explain the small change in slope of the c parameter shown experimentally. Lastly, the sudden increase in interlayer distance and the transition from hexagonal to monoclinic unit cell could be explained by the row ordering at $x = 3/4$. Unfortunately, XRD may not be an effective tool to distinguish between these orderings. Furthermore, the unique orderings of Na$_x$TiO$_2$, likely driven by the larger in-plane lattice parameters when compared to other transition metals in the same row, may have interesting kinetics. It may be especially interesting to study the solid-solution region of the hexagonal orderings and the devil's staircase transition to the row ordering at $x = 3/4$.

We provide a few low-energy structures that may be responsible for the irreversible phase transition above 1.6 V. However, without clear principles for avoiding the phase transition, the option of alloying Ti with other metals may be an interesting alternative. Alloying transition-metal oxides with Ti could have interesting consequences, both in terms of Na ordering and in suppressing the stacking-sequence change from O3 to P3 around $x = 1/2$ while at the same time stabilizing P3 at lower Na concentrations.

The Na$_x$TiO$_2$ system has many surprising properties and further work will be necessary to elucidate this unique system for battery applications.

Acknowledgments

Chapter 6

$\text{Li}_x MO_2$

One approach to increasing the capacity of Li-ion batteries is to expand the usable voltage range over which the battery is cycled by charging the cathode to higher voltages. Layered intercalation compounds commonly used as cathodes in Li-ion batteries, however, can become susceptible to irreversible structural changes at high states of charge due to cation migration to the emptied Li layers. Here we report on the discovery of a strong correlation between the position of the Fermi level and the energy barrier for cation migration to the Li layers of fully charged layered intercalation compounds [106]. Since the identity of the transition metal strongly influences the Fermi level, this discovery suggests that cation migration can be suppressed at high states of charge using targeted alloying strategies. First-principles calculations indicate that an increase in the concentration of Ni relative to Co or Mn should reduce, or even impede, interlayer migration in layered oxides. The insights of this study pave the way for the discovery of layered intercalation compounds that can approach their theoretical capacities in practice.

6.1 Introduction

Layered LiCoO$_2$ was first introduced as a cathode material for Li-ion batteries in 1991 [107, 108], and its derivatives remain the current standard in many applications. This is in spite of their practical reversible capacity being limited to 50-70% of their total theoretical capacity [109]. Capacities are in part limited due to structural changes that occur at high states of charge where the Li concentration of the host becomes very low [15]. Strategies that suppress these irreversible changes are necessary to realize the full theoretical capacities of layered intercalation compounds, thereby enabling higher energy densities and lower costs.

One approach to improve on LiCoO$_2$ is to alloy the Co sublattice of the LiCoO$_2$ host with different transition metals (M) or to dope it with non-redox active cations. For instance, NMC (Li$_x$Ni$_{1-y-z}$Mn$_y$Co$_z$O$_2$) employs a mixture of M elements (namely Ni, Mn, and Co) within the metal layers of the hot [110], while NCA (Li$_x$Ni$_{1-y-z}$Co$_y$Al$_z$O$_2$) combines a mixture of M elements with a non-redox active dopant (i.e. Al) [15]. Not only does this tend to increase reversible capacity, but it also reduces cost by utilizing more abundant elements [109]. We refer to non-transition-metal elements such as Al, Mg, or Li as dopants since their behavior within a layered intercalation compound differs from that of transition metals in that they lack d orbitals for bonding and therefore are not expected to participate in redox upon (dis)charge. Although non-transition-metal dopants are added at much higher concentrations than the classical use of the word may imply, their concentrations in layered intercalation compounds are usually sufficiently low that they do not interact with each other in any appreciable way and can be viewed as dilute from an alloying perspective. The combination of transition-metal alloying with non-transition-metal doping has also led to new classes of materials that promise high capacities. This includes Li-rich materials, which, while often having similar M

chemistries as NMC, also have an excess of Li that resides in the M layers [111]. Mg is also increasingly being investigated as a dopant in Na intercalation compounds [112].

While significant improvements have been achieved through doping and alloying [109, 113], very little is understood about the precise role that dopants play on battery performance. Some dopants such as Al [114–117] and Mg [117–121] appear to suppress undesirable phase transitions when added to Li$_x$CoO$_2$, such as the O3 to O1 structural transition at high states of charge [13, 14, 122–124] or the two-phase reaction due to the metal-insulator transition at high Li concentrations [125]. Since the dopants are not redox active, they retain some Li ions within the host to maintain charge neutrality at high states of charge, thereby preventing a significant contraction of the c-lattice parameter [124]. Layered electrode materials, however, are susceptible to irreversible structural changes at high states of charge due to the availability of many channels for interlayer cation migration that emerge when the Li-vacancy concentration is very high [113, 119, 126]. These irreversible changes usually lead to an overall degradation of electrochemical properties. Thus, though dopants may prevent some structural transformations, they can also cause capacity loss via irreversible migration.

As an illustration of the effect of dopants on electrochemical properties, Figs. 6.1(a) and (b) show the first charge and discharge voltage curves of Al doped Li$_x$NiO$_2$ and Li$_x$CoO$_2$ (i.e. Li$_x$Al$_y$Ni$_{1-y}$O$_2$ and Li$_x$Al$_y$Co$_{1-y}$O$_2$ for $y = 0, 0.05, 0.10,$ and 0.2). This is a small subset of a large number of Co, Ni, and Co/Ni host materials synthesized, cycled, and characterized in Ref [124], where more details of synthesis conditions, particle size, and characterization can be found (see also experimental methods section in Ref [106]). Electrode components and testing conditions were chosen to isolate irreversible capacity loss from kinetic factors and may not reflect commercial devices. The voltage window is sufficiently large (between 2.75 to 4.75 V) to ensure that the full theoretical capacity of each compound is accessed. As the concentration of Al increases, the initial charge

capacity decreases since fewer redox-active M atoms are available for oxidation at the end of charge. Dopants such as Al are viewed as beneficial because of their tendency to suppress detrimental structural phase transitions at high states of charge [114, 116]. This is evident in the voltage profiles of Figs. 6.1(a) and (b), which show a smearing out of phase transition steps and plateaus even at low Al concentrations.

Close inspection of the voltage profiles of Figs. 6.1(a) and (b) reveal a remarkable trend. While the initial capacity loss between first charge and discharge in the Ni compounds is large, it is relatively insensitive to Al concentration. The Co containing compounds, in contrast, exhibit a strong dependence of the first charge/discharge capacity loss on Al concentration. In fact, instead of reducing the first cycle capacity loss as expected, an increase in the Al concentration in Co hosts actually exacerbates it. This becomes clear when the capacity loss after the first cycle is plotted as a function of Al doping in the Ni and Co hosts as shown in Fig. 6.1(c). The electrochemical data of Fig. 6.1 shows not only that dopants can have a detrimental effect on capacity retention when a layered intercalation compound is charged to high voltages, but that its effect is also very sensitive to the host chemistry.

One possible explanation for the lost capacity after the first cycle is the irreversible migration of dopants out of the M layer and into the Li layer. For instance, Al migration can block sites and prevent a portion of the Li from reintercalating upon discharge. In fact, NMR evidence suggests the presence of Al in the Li layers of the Co hosts after the first discharge [124]. It is well known from studies of Li$_x$FePO$_4$ that M-Li anti-site defects can have a strong effect on Li conductivity [127–130].

Here we describe the results of a first-principles electronic structure study that predicts a strong dependence of the driving force for dopant migration to the Li layer on host chemistry. We find that the energy of a dopant along the migration path from the M layer to the Li layer is very sensitive to the position of the Fermi level. The susceptibility
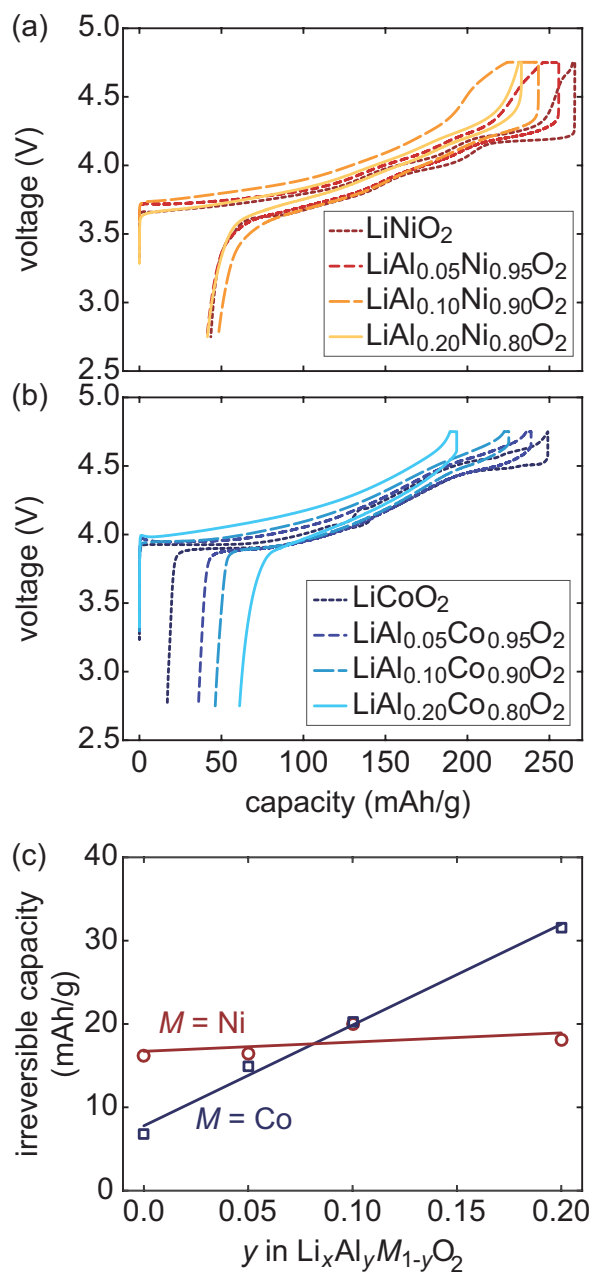
Figure 6.1: Experimental cycling data of an Al dopant in (a) Ni host and (b) Co host with varying concentration of Al. (c) Comparing the first cycle irreversible capacity loss with increasing Al concentration in Ni and Co hosts (markers are data, lines are least-square linear fits).

of dopants to migrate to the Li layer can, therefore, be controlled through modifications of the host chemistry, which determines the Fermi level. Our calculations predict that Ni-rich hosts will suppress dopant migration to the Li layer at high states of charge, while Co and Mn-rich hosts will not. Therefore, we expect Ni-rich hosts to experience smaller irreversible capacity losses upon cycling. Since many irreversible phase transitions that cause degradation require interlayer atom migration, understanding and suppressing this mechanism could increase reversible capacity and lengthen cathode lifetime. These insights suggest that important mechanisms of cathode degradation at high states of charge can be suppressed by alloying strategies that penalize dopant migration, thereby bringing us closer to realizing the full theoretical capacity of layered intercalation compounds.

6.2   Methods

Density functional theory (DFT) was utilized to calculate energies and electronic band structures using the Vienna Ab Initio Simulation Package (VASP) [24, 25] with the PAW method [70, 71] and the optb86b-vdw functional [72–75].

First, a 4×4 unit cell of NiO$_2$ was generated and one of the Ni atoms was replaced by a dopant, resulting in the formula $X_{1/16}$Ni$_{15/16}$O$_{32}$, where X = Al, Mg, Li, or vacancy. Electrons were artificially added to the system to enable a formal oxidation state of 4+ for all Ni, while the dopants could remain in their preferred formal oxidation states of Al^{3+}, Mg^{2+}, Li$^+$, or Va^0.

Second, 4×4 unit cells of MO$_2$ (M = Co, Mn, or Ni) were generated. In each case, one of the transition-metal atoms was replaced by a Li, Mg, or Al dopant. In addition, Li was added to the structures, with resulting compositions LiAlM_{15}O$_{32}$, Li$_2$MgM_{15}O$_{32}$, and Li$_4$$M_{15}O_{32}$ (M = Co, Mn, or Ni). In addition to keeping the dopant in the M layer, another set of similar cells was generated in which the dopant was moved to an adjacent

tetrahedral site in the Li layer, leaving behind a vacancy in the M layer. In both cases, many configurations were sampled using the CASM software [27–30] and lowest energy configurations were used for determining dumbbell formation energy.

More details on the computational methods are provided in the ESI accompanying Ref [106].

6.3   Tendency of ions to migrate

To understand interlayer migration within the layered O3 crystal structure, we first describe a path that dopants likely follow as they move from the M layer into the Li layer. The pristine synthesized material consists of transition-metal oxide (M-O) sheets separated by filled layers of octahedrally coordinated Li. The dopant usually replaces about 5% of the transition metals in the M layer, as illustrated in Fig. 6.2(a) with Li$_x$Mg$_y$Co$_{1-y}$O$_2$ ($x = 1$) [109, 117, 119, 121]. In the fully lithiated state, cations in the M layer cannot easily migrate to the Li layer since all of the octahedral Li sites are filled. However, upon charge, Li vacancies are introduced, allowing cations in the M layer to hop into the emptying Li layer [113, 119, 126].

A cation in the M layer must pass through an adjacent tetrahedral site before it can continue to an octahedral site of the Li layer. Figs. 6.2(b)-(e) show a migration path by which the dopant can hop out of the M layer and away from its original site; we use Mg migrating in a Co host as an example. In the fully charged state, there are two residual Li ions for every Mg dopant to maintain charge neutrality (assuming that Mg has a formal oxidation state of 2+ and the surrounding transition-metal ions have a formal oxidation state of 4+). The dopant (D) is initially in an octahedral site in the M layer (D$_{oct}$ configuration) (Fig. 6.2(b)). Based on extensive DFT calculations of the energies of different Li-vacancy orderings, we found that Li prefers to cluster around
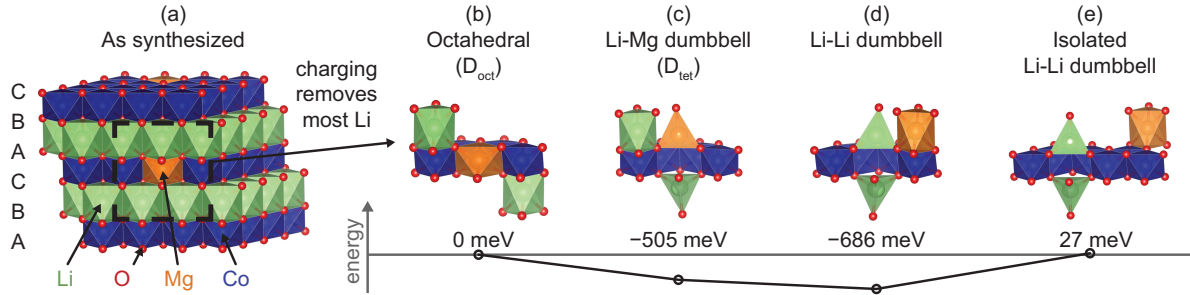
Figure 6.2: Possible path for dopant to move out of the M layer, into the Li layer, and away from the created vacancy upon delithiation; $Li_xMg_yCo_{1-y}O_2$ ($x = 2y$) illustrated, with relative energies of each snapshot along the path indicated below each image. (a) Structure is synthesized with Mg in M layer and filled Li layer. (b) Upon charge, Li is removed from the Li layer, resulting in the D_{oct} configuration. (c) Mg then migrates into the Li layer via Li-Mg dumbbell, eventually forming (d) a Li-Li dumbbell with an adjacent Mg. (e) Once the Li-Li dumbbell forms, a barrier exists for Mg to migrate away from the defect site. Images made using VESTA software [10].

the dopant as illustrated in Fig. 6.2(b) and (c). The vacancies in the Li layer, formed upon charging, open a pathway for the dopant to hop into an adjacent tetrahedral site in the Li layer. Fig. 6.2 also shows the energies of structures (b)-(e) relative to the D_{oct} configuration, as calculated with DFT. A low energy configuration that has Mg in the tetrahedral site is a Li-Mg dumbbell, D_{tet}, as illustrated in Fig. 6.2(c). While we have not calculated migration barriers, a reduction in energy of 500 meV when going from D_{oct} to D_{tet} (i.e. from Fig. 6.2 (b) to (c)) constitutes a very large driving force for Mg migration out of the M layer in the fully charged state. For migration between octahedral and tetrahedral sites, the hop barrier is dominated by the difference in energy between the two end states, with a considerably smaller contribution from intermediate positions, especially when the adjacent octahedral sites are vacant [41, 67, 131–133].

If Li were re-intercalated into the structure when the dopant is in the D_{tet} configuration, the dopant would likely return to the M layer and the reversible migration would have little effect on material degradation. If Mg did not return to the M layer, the Li-Mg dumbbell would block some Li sites from reintercalation. However, if the dopant moves

away from the vacancy in the M layer, an energetically favorable Li-Li dumbbell will rapidly form [134] as illustrated in Fig. 6.2 (d). Based on the Boltzmann distribution of the energy difference between configurations (c) and (d) at 300 K, Li-Li dumbbells would be about three orders of magnitude more probable than Li-Mg dumbbells. The stable Li-Li dumbbell is, therefore, likely to block the Mg from returning to its original site in the M layer thereby keeping it in the Li layer. This scenario results in an irreversible structural change of the host that will affect capacity and the voltage profile of subsequent cycles.

The example of Fig. 6.2 shows that Mg dopants in O3 Li$_x$CoO$_2$ experience a thermodynamic driving force to migrate to the Li layer towards the end of charge. Considering the irreversible and detrimental structural changes that such cation migration can inflict on the host, the question emerges: which other dopants and host chemistries exhibit a similar tendency for dopant migration to the Li layer in the fully charged state? Common dopants added to layered intercalation compounds include Al, Mg, and Li (the latter in Li-excess cathodes). Any cation that migrates to the Li layer will invariably form an intermediate Li-dopant dumbbell configuration, D$_{tet}$, as illustrated in Fig. 6.2(c) [135,136]. The difference in energy between the D$_{tet}$ configuration and the initial D$_{oct}$ state determines whether or not a dopant experiences a driving force to migrate to the Li layer at the end of charge. In the remainder of this work, we focus on these two configurations.

Fig. 6.3 compares the stability of the D$_{tet}$ configuration relative to D$_{oct}$ for Al, Mg, and Li dopants in the O3 forms of fully charged Ni, Co, and Mn hosts. The energies of many Li orderings were calculated for each system in the D$_{oct}$ and D$_{tet}$ configurations, and the lowest energy for each dopant configuration was used to calculate the energy differences of Fig. 6.3. Negative energies indicate that the Li-dopant dumbbell is more stable and that the dopant therefore has a tendency to migrate to the Li layer. The formation energies become more negative as the oxidation state of the dopant decreases

(i.e. $Al^{3+} \rightarrow Mg^{2+} \rightarrow Li^+$; moving down the chart for the same host). The lower the dopant's oxidation state, the more stable the D$_{tet}$ configuration becomes. More surprisingly, however, is the peculiar trend with respect to the host chemistry. The Co and Mn hosts exhibit similar energy differences for the same dopant and tend to prefer D$_{tet}$ configurations. The Ni host, in contrast, appears to penalize Li-dopant dumbbells. The implication of Fig. 6.3 is that the Ni host will suppress dopant migration to the Li layer in the fully charged state since the crucial first step of the migration process results in an increase in energy. In the next sections, we explore the role that the electronic structure of the host plays in determining the susceptibility of dopant migration to the Li layer in these three hosts.

6.4 Transition metal substitution

In this section, we determine the effect of dopants having different oxidation states on the electronic structure of a fully delithiated transition-metal oxide. We replace one of the Ni atoms in a supercell of NiO$_2$ containing 16 primitive unit cells with either Al, Mg, Li, or a vacancy (Va). The choice of dopants is motivated not only by their technological importance, but also by the fact that their formal oxidation state differs from each other and from that of the 4+ charge of the transition-metal cations: Al^{3+}, Mg^{2+}, and Li^+. We also consider a vacant M site since a vacancy donates zero electrons to the host. By varying the dopant, we are effectively changing the local electrostatic potential experienced by the six O atoms adjacent to the defect. Since each dopant has a formal oxidation state that is lower than the 4+ oxidation of the transition metals, there must be residual Li ions in the Li layer to maintain charge neutrality in the fully charged state; one, two, three, and four Li must remain in the host for each Al, Mg, Li, and Va dopant, respectively. We will consider the explicit effect of these residual Li ions later.
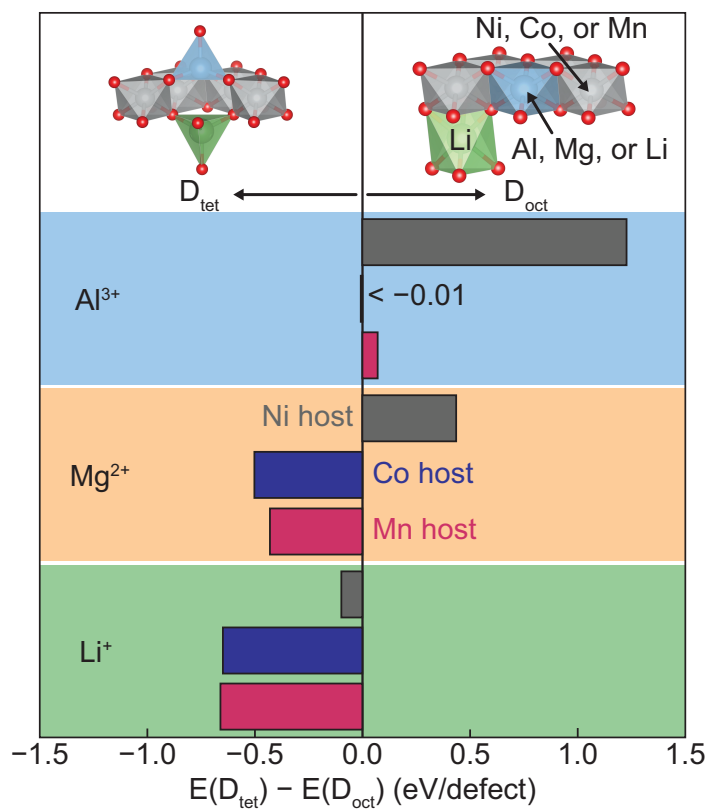
Figure 6.3: Difference in energy between D_{oct} and D_{tet} configurations. Extra Li ions are added as necessary for charge compensation. Dumbbells are relatively more stable as dopant oxidation state decreases and more stable in Co and Mn hosts than in the Ni host. Portions of image made using VESTA software [10].

However, to qualitatively determine the effect of dopants on the electronic structure, we first perform calculations in the absence of explicit residual Li ions, instead adding their valence electrons to the host and compensating the excess negative charge with a uniform positive background charge.

The density of states (DOS) for each dopant in NiO$_2$ are shown in Fig. 6.4 and are aligned based on the bottom of the deep O s states (below the states shown in the figure). Though spin-polarized calculations were performed, the spin channels were identical and only one of them is shown. Localized peaks at the top of the t$_{2g}$ and e$_g$ blocks not present in the DOS of pure NiO$_2$ appear in the other four panels and are highlighted in red. We refer to these localized states as defect states because they form as a result of transition metal substitution by a vacancy or non-transition-metal atom. All of the t$_{2g}$ states are filled in NiO$_2$ and therefore significantly contribute to the overall energy unlike the defect states in the empty e$_g$ block. Therefore, references to defect states in this work largely concern the localized t$_{2g}$ states. Fig. 6.4 shows that as the oxidation state of the dopant decreases from left to right, the defect states become more prominent and increase in energy. Since the defect states are occupied in NiO$_2$, their rise also results in an increase in the Fermi level (relative to the deep O s states).

Fig. 6.4 shows the electronic charge density associated with the defect states when the dopant is a vacancy (i.e. Va$_{1/16}$Ni$_{15/16}$O$_{32}$). The figure is oriented looking down on a single layer of the M oxide, and the yellow lobes are an isosurface of electron charge density. The majority contribution comes from the O and Ni atoms that immediately surround the vacancy. The high-energy defect states consist of six O p orbitals that point towards the vacancy and six Ni d orbitals that point between the oxygen ions. The O p and Ni d orbitals are aligned for π bonding. The defect states for the other dopants exhibit similar electronic charge densities around the dopant site.
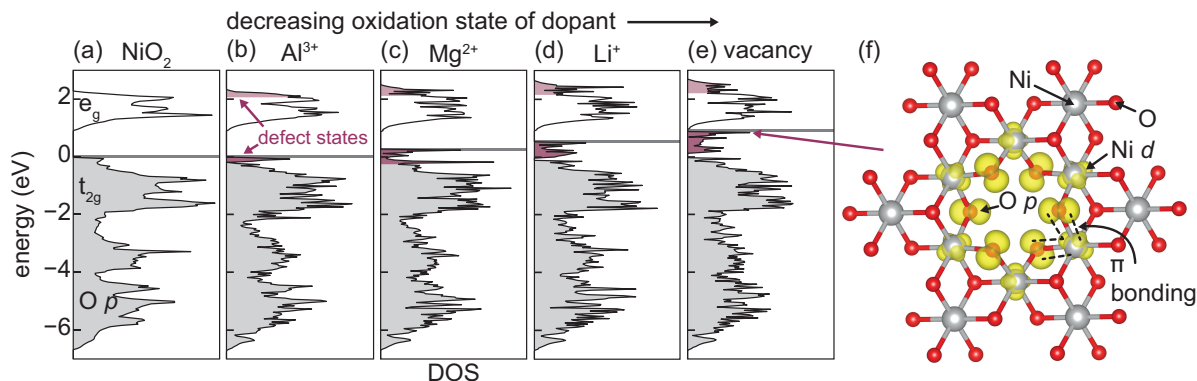
Figure 6.4: (a-e) DOS of pristine NiO$_2$ and $D_{1/16}$Ni$_{15/16}$O$_{32}$ for D = Al, Mg, Li, or vacancy. The oxidation state of the dopant decreases from left to right and is compensated by a background electronic charge. Bands with major contribution from orbitals around the defect (i.e. defect states) are highlighted in red. Occupied defect states just below the Fermi level increase in energy with decreasing oxidation state of dopant. (f) Partial charge density of the highest occupied band looking down on a layer of Ni$_{15/16}$O$_{32}$. Large O p and Ni d orbitals are localized around the atoms near the vacancy and appear to be π bonding. Portion of image made using VESTA software [10].

6.5 Dumbbell formation

Having determined that dopants generate high-energy defect states, we next consider the changes in electronic structure as the dopant migrates from the M layer (D$_{oct}$ configuration) into a dumbbell (D$_{tet}$ configuration). In this section, we explicitly treat the residual Li ions that must remain in the Li layer to maintain charge neutrality in the fully charged state. For cases where multiple Li arrangements were possible, the lowest-energy configuration was used (of the ones calculated, details in ESI of Ref [106]). In general, it was found that configurations that cluster Li around the defect have the lowest energy. We begin by considering dopants in the Ni host and then determine how the electronic structure changes when the same dopants were added to Co and Mn hosts.

Fig. 6.5 compares the calculated DOS for NiO$_2$ with DOS for Li-Al in D$_{oct}$ and D$_{tet}$ configurations. Fig. 6.5 (b) shows that the replacement of one octahedral Ni by Al results in defect states immediately below the Fermi level that are qualitatively similar
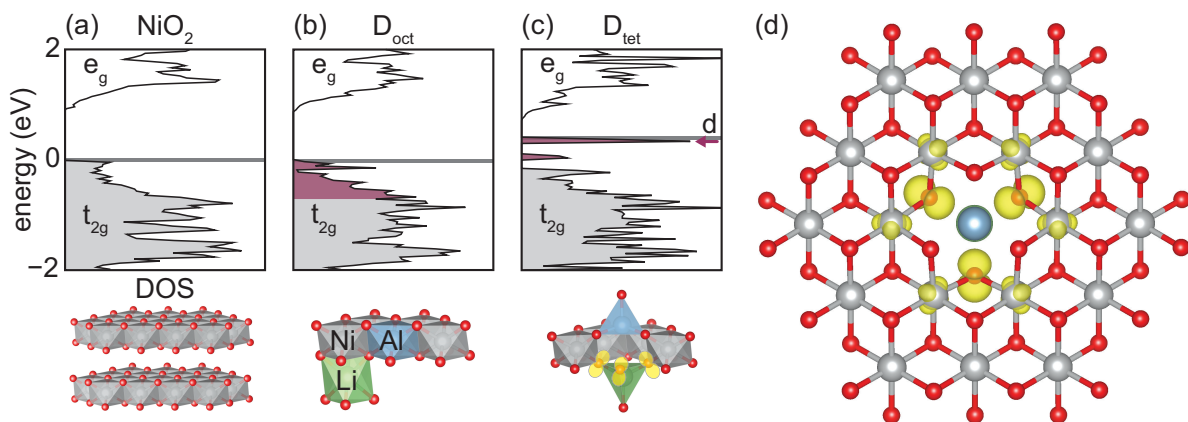
Figure 6.5: DOS of (a) layered bulk NiO$_2$, (b) octahedral Al dopant in the M layer with Li for charge balance in the Ni host, and (c) Li-Al dumbbell in the Ni host. Defect states are highlighted in red. (d) The partial charge density of the highest occupied band of the D$_{tet}$ configuration. The O p lobes in (d) are on the O next to Li, as indicated in yellow on the structure in (c). Portions of image made using VESTA software [10].

to those around a vacancy as described in the previous section. One Li remains in the host for each Al dopant to maintain charge neutrality in the fully charged state. The lowest energy state has Li residing in an octahedron that shares a corner with the Al octahedron. Site projected DOS (figure in ESI of Ref [106]) shows that the defect states comprise of O p and Ni d orbitals from O and Ni that neighbor the Al dopant. Not all O p states that point to the Al, however, contribute to the high energy defect states. Only those O that are not coordinated by a Li in the Li layer participate in the defect states. These O atoms are surrounded by less positive charge and therefore have a higher energy.

The Li-Al D$_{tet}$ configuration produces defect states at even higher energies (Fig. 6.5 (c)). The electronic charge density associated with the highest energy defect state is shown in Fig. 6.5 (d). The defect state is again primarily composed of π bonded O p orbitals and Ni d orbitals. Only the O p orbitals that belong to the base of the tetrahedron occupied by Li and that point to the octahedral vacancy participate in bonding. These particular O p levels have a high energy as they are coordinated by the low positive

charge of Li. The similar O p orbitals of the base of the tetrahedron occupied by Al are surrounded by substantially higher positive charge and therefore have a lower energy. The D$_{tet}$ configuration results in a significant increase of the Fermi level since the defect states in the Ni host remain occupied. As shown in Fig. 6.3, the D$_{tet}$ configuration is 1.2 eV/dopant higher in energy than the D$_{oct}$ configuration. At room temperature, few dumbbells are therefore expected to form.

It is also instructive to consider the change in electronic structure when Li serves as a dopant in the M layer as it has a much lower oxidation state. Four Li must be present in the structure for every transition metal that is removed to maintain charge neutrality in the fully charged state. The lowest energy D$_{oct}$ and D$_{tet}$ configurations are ones that cluster Li around the defect, as illustrated in Fig. 6.6(b) and (c). In the D$_{oct}$ configuration (Fig. 6.6(b)), large spikes in DOS appear at the top of the occupied states, similar to ones seen for NiO$_2$ with a Li-Al dumbbell (Fig. 6.5(c)). Similar high energy defect states appear in the Li-Li D$_{tet}$ configuration (Fig. 6.6(c)). The highest energy states for D$_{tet}$ are associated with the O that have only one adjacent Li. The defect states that are slightly lower in energy derive from the O that are coordinated by two adjacent Li. This is shown in representative partial charge densities in Figs. 6.6(d) and (e). While the Fermi level does increase when going from the D$_{oct}$ configuration to the D$_{tet}$ configuration, the overall energy of the D$_{tet}$ configuration is lower than D$_{oct}$ by 100 meV/dopant. Li-Li dumbbells are therefore favored upon delithiation.

The electronic structures of the Co and Mn hosts are very different from those just described for NiO$_2$. Both Co and Mn have fewer electrons than Ni and therefore CoO$_2$ and MnO$_2$ only partially fill their t$_{2g}$ states. Furthermore, CoO$_2$ and MnO$_2$ exhibit a net magnetic moment when initialized in the ferromagnetic state (Fig. 6.7(a) and (e)). The CoO$_2$ system exhibits a relatively weak exchange splitting, with the spin-up and spin-down DOS only slightly offset from each other. One of the spin channels has the
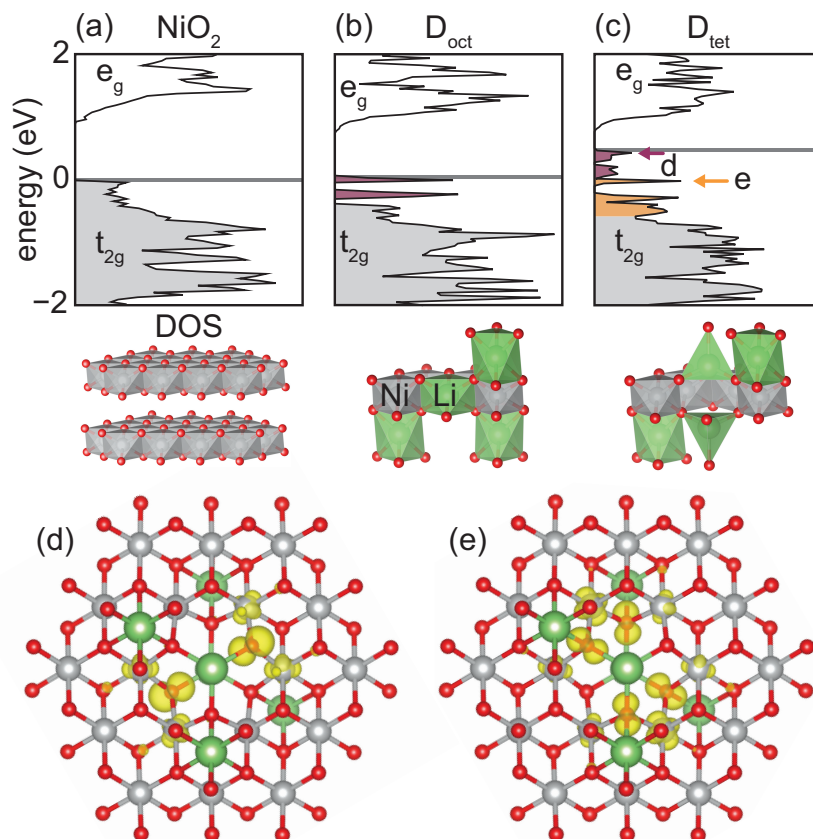
Figure 6.6: DOS of (a) layered bulk NiO$_2$, (b) octahedral Li dopant in the Ni host, and (c) Li-Li dumbbell in the Ni host. (d) Partial charge density of band at the top of the occupied bands with O p character on oxygen not adjacent to additional Li atoms, highlighted in red. (e) Partial charge density of a band slightly lower in energy with O p character on oxygen adjacent to an additional Li atom, highlighted in orange. Portions of image made using VESTA software [10].

t_{2g} states almost completely filled, while the other has more empty t_{2g} states. In MnO_2, the difference is more drastic; t_{2g} states of one of the spin channels fills completely while those of the other reside much higher in energy and therefore stay empty.

Fig. 6.7 shows the DOS for an Al dopant in Co and Mn hosts. The defect states are more delocalized in the D_{oct} configuration in these two hosts with the Al dopant than was the case in the Ni host and are therefore not easily distinguishable from the total DOS. The defect states are more pronounced in the D_{tet} configurations (highlighted red in Figs. 6.7(c) and (f)), exhibiting a significant increase in DOS at the top of the t_{2g} block. The distinction is based on O p pDOS (figure in ESI of Ref [106]), where the defect states are characterized by a spike in density for O atoms surrounded by the least positive charge (in this case, adjacent to tetrahedral Li). Since the defect states reside at the top of the t_{2g} block in both spin channels, not all of them need to be filled in the Co and Mn hosts. The energetic penalty for forming the D_{tet} relative to the D_{oct} configuration is, therefore, much lower in the Co and Mn hosts since some of the defect states can remain empty. In the Mn host, the Li-Al D_{oct} configuration is slightly more stable than the D_{tet} configuration by 65 meV/defect while the two configurations are essentially degenerate in the Co host. This is in stark contrast to the highly unfavorable Li-Al dumbbell in the Ni host. Similarly, for the Li-Mg and Li-Li defects, the D_{tet} configurations are favored more for Co and Mn hosts than for the Ni host.

With this new theoretical understanding, we return to the experimental results presented in Fig. 6.1. As the defect states are completely occupied in the Ni host but only partially filled in the Co host, our calculations predict that more Li-Al dumbbells will form in the latter due to entropic factors. Fig. 6.3 shows that there is essentially no energy difference between the D_{oct} and D_{tet} configurations in the Co host, but a sizable energy penalty for D_{tet} in the Ni host. Since the synthesized particles of the different compositions had comparable surface areas, surface interactions with the electrolyte are
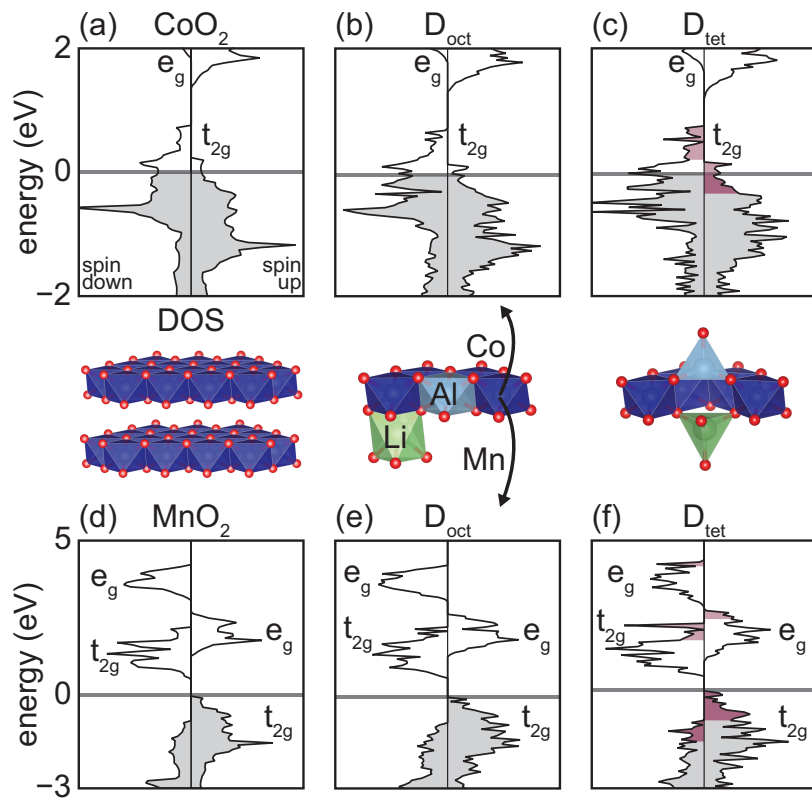
Figure 6.7: DOS of (a) layered bulk Co, (b) octahedral Li-Al defect in the Co host, (c) dumbbell Li-Al defect in Co host, (d) layered bulk MnO_2, (e) octahedral Li-Al defect in the Mn host, and (f) dumbbell Li-Al defect in the Mn host. Defect states overlap strongly with the rest of the t_{2g} bands in the D_{oct} configurations, but are highlighted in red for the D_{tet} configurations. Portions of image made using VESTA software [10].

unlikely to result in the stark difference in capacity loss behavior between Ni and Co hosts [124]. Furthermore, Nuclear Magnetic Resonance (NMR) findings strongly support that Al does migrate into tetrahedral sites in the Co host and not in the Ni host [124]. The experimental conditions should allow for interlayer atom migration because the cells are cycled to very high voltages (upwards of 4.75 V) and are thus able to approach the limits of delithiation. Only at high voltages, when the only remaining Li in the material is that pinned by the redox inactive dopant, can the Al migrate into the Li layer of the Co host. Our calculations indicate that Mg-doped Co, Ni, and Mn hosts may also show a large discrepancy in capacity loss between the hosts, but comparable experiments at high voltage have yet to be performed on Mg-doped Co and Ni hosts. These experiments are beyond the scope of this study.

6.6   Discussion

Layered transition metal oxide intercalation compounds remain the cathode material of choice in current Li-ion battery technologies. However, only 50-70 % of the theoretical capacity of these cathode materials is currently utilized due to the rapid degradation that occurs at high states of charge [15]. Many layered intercalation compounds tend to become highly metastable upon the complete removal of Li ions and are susceptible to structural changes due to transition metal and dopant migration to the emptied Li layers.

In this study, we used electronic structure calculations to determine the effects of chemistry on the susceptibility of dopant migration in O3 layered transition-metal oxides. A dopant that migrates from the M layer to the Li layer must first pass through an intermediate tetrahedral site. The most stable intermediate configuration is one in which the dopant forms a dumbbell with a residual Li. Our calculations have shown that

the stability of Li-dopant dumbbells in the fully charged state is highly sensitive to the identity of transition-metal cations surrounding the dopant site: a Ni host tends to suppress Li-dopant dumbbell formation while Co and Mn hosts favor their formation. This remarkable result suggests that targeted alloying of layered transition-metal oxides can serve as an effective strategy to suppress dopant migration at high states of charge.

The stark difference in the susceptibility of dopants to migrate to the Li layer between the Ni host on the one hand and Co and Mn hosts on the other has its origin in electronic structure. Fig. 6.8 schematically summarizes the essential features of the DOS of pure and doped transition metal oxides as distilled from the detailed electronic structure calculations of the previous sections. The electronic structure of the pure hosts, in the absence of dopants, consists of three major blocks: low energy states having predominantly O p character; t$_{2g}$-like states made up of π bonded transition-metal d orbitals and O p orbitals; and anti-bonding e$_g$-like states. In NiO$_2$, the Fermi level resides between the e$_g$ block and the t$_{2g}$ block. In CoO$_2$ and MnO$_2$, in contrast, the Fermi level resides in the t$_{2g}$ block. Some of the higher energy t$_{2g}$-like states that are made up of π bonded M d orbitals and O p orbitals are empty in Co- and Mn-rich compounds.

The emergence of localized defect states and their high energy are closely linked to the fact that the dopant oxidation states are lower than 4+ and that they do not have d orbitals. A lower amount of coordinating positive charge lifts the energy of the O p orbitals near the defect such that they form localized states. This ionic interaction is illustrated by the rise in the energy of the defect states with the reduction in the oxidation state of an octahedral dopant in Fig. 6.4. Hybridization between the O p and M d orbitals also plays a role in the origin of the defect states. The O p orbitals involved in the defect states just above the t$_{2g}$ block are orbitals that in the pristine material would exhibit a σ interaction with the d orbitals of the missing M, making them dangling bonds. Although such states are often referred to as orphaned states in
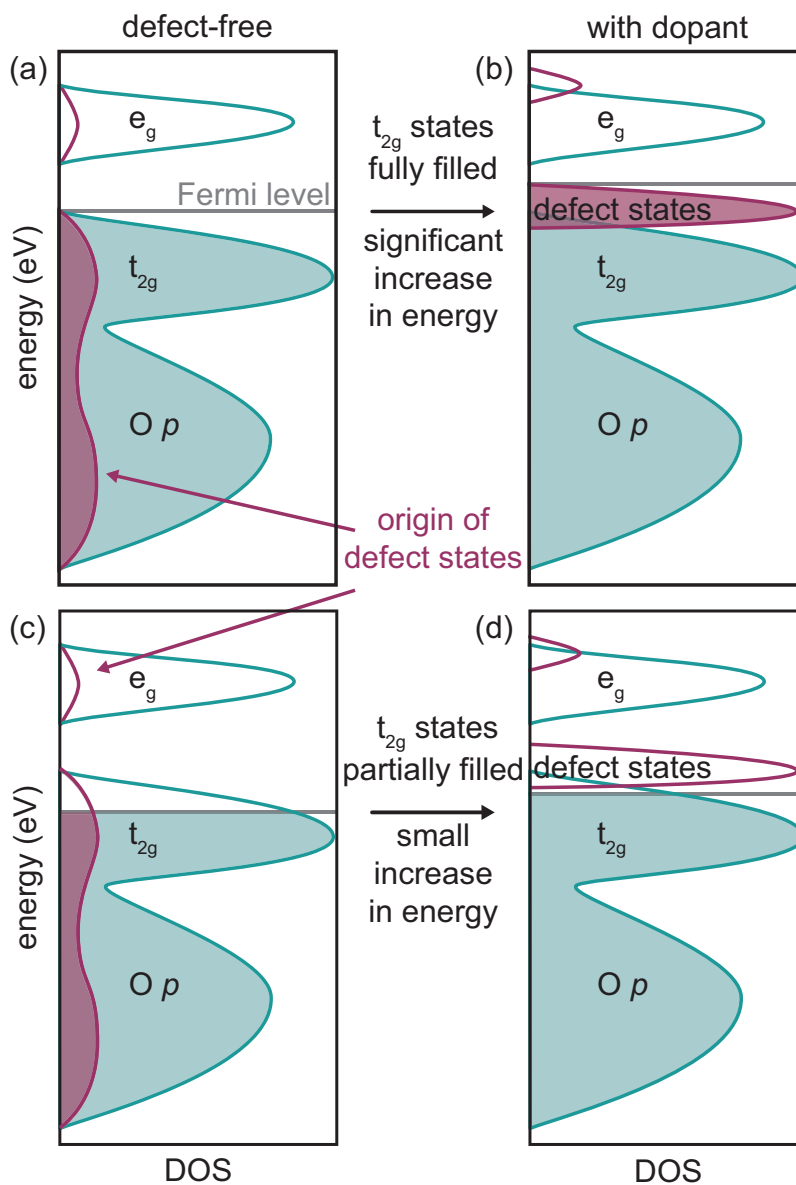
Figure 6.8: Schematic representation of DOS for defect-free and doped layered oxides. (a) Defect-free layered oxide with all t$_{2g}$ states filled, as in NiO$_2$ and (b) that layered oxide doped with a lower oxidation-state ion, such as Al in the Ni host. Defect states increase the overall energy of the system. (c) Defect-free layered oxide where the M has fewer electrons, for instance CoO$_2$, and (d) that layered oxide doped with a lower oxidation state ion, for instance Al in the Co host. The high-energy defect states do not have to be filled, so the energy increases less than for the case above.

the context of Li-excess materials [137, 138], they nevertheless exhibit π bonds with the surrounding transition-metal ions. This π interaction can be seen in Figs. 6.4, 6.5, and 6.6, which show that the defect states have significant contributions not only from O but also from the remaining neighboring transition-metal cations.

Since the defect states appear at the top of the t$_{2g}$ block, the position of the Fermi level determines the extent to which they are occupied. In systems where the M has sufficient electrons to fill all of the t$_{2g}$ states, the defect states are completely filled and significantly contribute to the overall energy (Figs. 6.8(a) and (b)). In systems with fewer electrons, where the Fermi level resides within the t$_{2g}$ block, at least some of the defect states may remain empty, reducing their contribution to the overall energy (Figs. 6.8(c) and (d)). Therefore, systems that do not fully fill the t$_{2g}$ bands are less affected by dopant inclusion and have a smaller penalty for dumbbell formation.

In addition to M identity, Fig. 6.3 shows that the identity of the migrating species has a strong effect on the stability of the D$_{tet}$ configurations. Dopants with a lower oxidation state, like Li, are more likely to form dumbbells than cations like Al, which has a higher oxidation state. Cation size alone cannot explain this trend as Li and Mg both have very similar sizes, but Li has lower dumbbell formation energies in all three hosts. Instead, there is likely a smaller penalty from the defect states for D$_{tet}$ configurations when the dopant has a lower oxidation state. Dumbbell formation energy is the difference in energy between the D$_{oct}$ and D$_{tet}$ configurations. This energy is high for dopants like Al because the difference between the electrostatic potential for certain O atoms changes drastically when the Al moves from the M layer into the tetrahedral site. However, the local environment around the O is similar for D$_{oct}$ and D$_{tet}$ when Li is the dopant. The defect states are already very high in energy when the Li is in the M layer, as evidenced by the DOS in Fig. 6.6(b), so that a change to the tetrahedral site does not raise the energy of the defect states.

We completed additional calculations to confirm that differences in the lattice param-eters of the hosts were not responsible for the difference in dumbbell formation energies. We performed static calculations of the D$_{oct}$ and D$_{tet}$ configurations using the relaxed lattice parameters of the other two hosts (e.g. we imposed the Ni and Co host lattice parameters on the Mn host and vice versa) to determine if the particular lattice param-eters were responsible for the trend in dumbbell formation energies (details and results in the ESI for Ref [106]). Even when the lattice parameters of the Co or Mn hosts were imposed on LiAlNi$_{15}$O$_{32}$, the dumbbell formation energy was around 1 eV/Al. Al-ternatively, the Ni host lattice parameters did not make the dumbbell significantly less stable in LiAlCo$_{15}$O$_{32}$ and LiAlMn$_{15}$O$_{32}$. We also found that when the atomic positions were kept constant, Li was still more likely to form dumbbells than Al. Therefore, the qualitative dumbbell formation trends seen in Fig. 6.3 cannot be ascribed to size effects.

The trends described so far are not restricted to dopant migration. They also apply to transition metal migration. We performed calculations to determine the change in energy when a Ni or Co atom migrates from the M layer to an adjacent tetrahedral site of an empty Li layer in both a Ni and Co host. The barriers are lower bounds in the fully charged state when all of the transition metals are in a formal 4+ oxidation state. The tetrahedral defect formation energies were predicted to be 2.75 and 2.61 eV/defect for a Ni and Co in the Ni host, respectively, while they were 1.34 and 1.29 eV/defect for Ni and Co in the Co host, respectively. All four energies are high and positive, indicating a high kinetic barrier for transition metal migration to the empty Li layers of fully charged Co or Ni hosts. Similar to the dopant-dumbbell formation energies, however, the calculated energies only marginally depend on the identity of the migrating cation, but instead depend strongly on the host chemistry. The barrier for M migration to empty Li layers is substantially higher in the Ni host than in the Co host, differing by over 1 eV. We emphasize that these trends are predicted for the fully delithiated Ni host. It is well

known that Li$_x$NiO$_2$ usually contains a small percentage of Ni in the Li layer [118, 139]. However, these extra Ni are introduced during high temperature synthesis in the fully lithiated state.

All first-principles results reported in this study were based on density functional theory using a PBE functional as described in the Methods section. It is generally accepted that a DFT+U approach [140, 141] is necessary to accurately describe the electronic structure of M oxides [142]. Here we found that the predictions are both qualitatively and in large part quantitatively insensitive to approximations to DFT. Values of $+U$ corrections ranging between 0 and 5 were used to calculate the energies of Li-Al D$_{oct}$ and D$_{tet}$ configurations in Ni and Mn hosts (use of $+U$ in Co oxides has been shown to result in incorrect ground state configurations [143, 144]). Dumbbell formation energies and the qualitative shape of the DOS were very similar for all values of the Hubbard U (see figures in ESI for Ref [106]). The invariance of the predicted energy differences to the value of $+U$ is likely due to the fact that all transition metals are in their 4+ oxidation state and remain in that state for each dopant configuration.

The correlations revealed in this study between electronic structure and the susceptibility for interlayer migration in M oxides can be utilized in cathode design. Alloying strategies that maximize the filling of the t$_{2g}$ states, and therefore all localized defect states, when the battery is fully charged will penalize dumbbell formation and hence cation migration to the Li layer. In general, an increase in the Ni concentration can be a simple solution for systems where dumbbell formation must be suppressed to improve kinetics and cycleability. The favorable cycling behavior of Ni-rich NCA compounds (Li$_x$(Ni$_{1-y-z}$Co$_y$Al$_z$)O$_2$) is consistent with the predictions of this work [124]. Our study suggests that dopant migration is likely to contribute significantly to cathode degradation at high states of charge in Co-rich chemistries. Mg, for example, is used as a dopant in Li$_x$CoO$_2$ to suppress the two-phase region between $x = 0.93$ and 0.75 [125]. The

predictions of this study indicate that Mg dopants will experience a driving force to migrate to the Li layer in the fully charged state, thereby causing irreversible changes to the host crystal structure. An increase in the Ni content will suppress these tendencies, while the addition of Mn will not. Of course, other factors will also need to be taken into consideration when varying transition-metal chemistry, including the effect of such variations on the intrinsic electronic conductivity of the compound.

The results presented here also suggest that certain dopants could promote the degradation of the cathode through oxygen evolution. In cases where defect states are unoccupied (such as the Li-Al dumbbell in the Co host), the O p states near the defect are significantly depleted. Prior calculations suggest that this depletion of O p states could enable the dimerization of oxygen and subsequent formation of O$_2$ molecules, leading to irreversible degradation of the material [145]. This suggests that the tetrahedral migration of dopants may negatively impact the reversibility of electrodes not only by causing a redistribution of cations but also by triggering oxygen loss.

Lastly, while the experimental cycling results shown in Fig. 6.1 correlate well with conclusions from our computational work, more direct observations of dopant migration would enhance our understanding of this mechanism. NMR measurements have already indicated the presence of Al in the Li layer of Co rich hosts but not in the Ni rich hosts [124]. Though the positions of disordered dopants can be difficult to characterize with common methods such as X-ray diffraction (XRD), other spectroscopic techniques including X-ray absorption spectroscopy (XAS) and resonant inelastic X-ray scattering (RIXS) could be used to characterize differences in electronic structure between Al doped Ni-rich and Co-rich hosts [146,147]. Signatures of the electronic defect states will provide information as to whether or not dumbbells form. It is important, however, to recognize that any ex situ probes have their limitations as these materials are highly metastable at high states of charge and may readily decompose upon removal from the battery [15].

6.7   Conclusions

Irreversible structural changes in the cathode at the end of charge are a significant hurdle that inhibits further capacity utilization in current battery materials. In order to surmount this challenge, a better understanding of cation migration as a function of cathode composition is critical. Using first-principles calculations, we have demonstrated a strong correlation between the identity of the transition metal and the energy barrier for cation migration to empty Li layers of fully charged layered intercalation compounds. We show that oxides with higher concentrations of Co or Mn are likely to experience enhanced rates of interlayer atom migration, while an increase in the Ni concentration should suppress migration and stabilize the layered structure at high states of charge. The origins of this sensitivity to chemistry are rooted in electronic structure. We speculate that the behavior in battery materials having other crystal structures or utilizing different intercalants leads to similar electronic structure effects. The implications of our work can be extended to better understand oxygen dimerization and gas evolution, which is also detrimental for battery performance. Considering that interlayer migration can result in irreversible capacity loss, these new insights suggest a clear path to the discovery of cathode chemistries that can achieve practical capacities approaching their theoretical values.

Acknowledgments

Chapter 7

Concluding remarks

In this thesis, we have explored structural evolution in a range of layered electrode chemistries. Since these processes often lead to material degradation, capacity loss, and lifetime reduction, it is important to understand the underlying causes of the observed behavior. As many mechanisms that lead to structural changes occur in the bulk material on the atomic scale, we have employed first-principles methods to identify and understand the changes that occur in layered materials upon cycling. This fundamental knowledge aids in interpreting observed phenomena during battery cycling and can guide design principles for avoiding damaging mechanisms.

In Ch. 4 and 5, we focused on stacking-sequence changes and Na ordering upon charging the materials. For the $Na_x TiS_2$ system, we confirmed the thermodynamic driving force for a phase transition from O3 to P3 at intermediate Na concentrations and reported staged hybrid stackings upon further desodiation. The ordering of Na in the P3 structure showed a unique devil's staircase marked by varying sizes of triangular islands. We then turned to $Na_x TiO_2$ in which the P3 structure is suppressed near the $x = 1/2$ composition. There is some indication that the P3 phase is more stable than O3 at lower compositions, which could have implications for alloying other transition-metal oxides

with Ti. Through a thorough analysis of Na orderings in O3 Na_xTiO_2 as well as structural considerations, we propose several Na orderings that may be responsible for the experimentally observed voltage step. Furthermore, the unique orderings in P3 Na_xTiS_2 and O3 Na_xTiO_2 may have interesting consequences for Na diffusion in these and similar materials. Though not explicitly explored in these studies, the topic can be studied with future work involving kinetic Monte Carlo.

In Ch. 6, we looked at the changes that occur in Li-ion cathodes at high voltages, when most of the Li has been removed. We found that the thermodynamic drive for atoms to move into the mostly empty layers is dictated not only by the identity of the migrating ion itself, but also by the identity of the surrounding transition metals. Our calculations suggest that the electronic structure of Ni may suppress the migration of its neighbors, whereas cations next to Co or Mn would be more likely to hop into the Li layer. Mitigation of interlayer migration would be an important step in increasing reversible capacity in current battery materials.

Although our work centers on specific materials, our findings can be expanded beyond the chemistries in these studies. While we have mentioned various shuttling ions (Li, Na), transition metals (Ti, Co, Mn, Ni), non-active metals (Mg, Al), and anions (O, S) in this work, there are many more compositions not discussed here that exhibit layered structures. Layered transition-metal oxides and sulfides share many general characteristics like prominence of stacking-sequence changes, certain phase transitions (especially involving interlayer migration), and diffusion pathways, which provides an amazing opportunity to explore overarching trends in how changes in chemistry within the same structure determines cycling properties. This is the goal of continued research in the topic and the pathway to improving battery materials.

Bibliography

[1] K. E. Trenberth, *Changes in precipitation with climate change*, Clim. Res. **47** (2011), no. 1 123–138.

[2] A. L. Westerling, H. G. Hidalgo, D. R. Cayan, and T. W. Swetnam, *Warming and earlier spring increase Western U.S. forest wildfire activity*, Science **313** (2006), no. 5789 940–943.

[3] S. C. Doney, V. J. Fabry, R. A. Feely, and J. A. Kleypas, *Ocean acidification: The other CO_2 problem*, Ann. Rev. Mar. Sci. **1** (2009), no. 1 169–192.

[4] T. L. Root, J. T. Price, K. R. Hall, S. H. Schneider, C. Rosenzweig, and J. A. Pounds, *Fingerprints of global warming on wild animals and plants*, Nature **421** (2003), no. 6918 57–60.

[5] J. Cook, N. Oreskes, P. T. Doran, W. R. L. Anderegg, B. Verheggen, E. W. Maibach, J. S. Carlton, S. Lewandowsky, A. G. Skuce, S. A. Green, D. Nuccitelli, P. Jacobs, M. Richardson, B. Winkler, R. Painting, and K. Rice, *Consensus on consensus: A synthesis of consensus estimates on human-caused global warming*, Environ. Res. Lett. **11** (2016), no. 4.

[6] G. B. Bonan, *Forests and climate change: Forcings, feedbacks, and the climate benefits of forests*, Science **320** (2008), no. 5882 1444–1449.

[7] Y. Malhi, J. T. Roberts, R. A. Betts, T. J. Killeen, W. Li, and C. A. Nobre, *Climate change, deforestation, and the fate of the Amazon*, Science **319** (2008), no. 5860 169–172.

[8] M. Z. Jacobson and M. A. Delucchi, *Providing all global energy with wind, water, and solar power, Part I: Technologies, energy resources, quantities and areas of infrastructure, and materials*, Energy Policy **39** (2011), no. 3 1154–1169.

[9] C. Budischak, D. Sewell, H. Thomson, L. Mach, D. E. Veron, and W. Kempton, *Cost-minimized combinations of wind power, solar power and electrochemical storage, powering the grid up to 99.9% of the time*, J. Power Sources **225** (2013) 60–74.

[10] K. Momma and F. Izumi, *VESTA 3 for three-dimensional visualization of crystal, volumetric and morphology data*, J. Appl. Crystallogr. **44** (2011), no. 6 1272–1276.

[11] M. S. Whittingham and F. R. Gamble, *The lithium intercalates of the transition metal dichalcogenides*, Mater. Res. Bull. **10** (1975), no. 5 363–371.

[12] C. Delmas, J. Braconnier, C. Fouassier, and P. Hagenmuller, *Electrochemical intercalation of sodium in Na_xCoO_2 bronzes*, Solid State Ion. **3–4** (1981) 165–169.

[13] A. Van der Ven, M. K. Aydinol, G. Ceder, G. Kresse, and J. Hafner, *First-principles investigation of phase stability in Li_xCoO_2*, Phys. Rev. B **58** (1998), no. 6 2975–2987.

[14] Z. Chen, Z. Lu, and J. R. Dahn, *Staging phase transitions in Li_xCoO_2*, J. Electrochem. Soc. **149** (2002), no. 12 A1604–A1609.

[15] M. D. Radin, S. Hy, M. Sina, C. Fang, H. Liu, J. Vinckeviciute, M. Zhang, M. S. Whittingham, Y. S. Meng, and A. Van der Ven, *Narrowing the gap between theoretical and practical capacities in Li-ion layered oxide cathode materials*, Adv. Energy Mater. **7** (2017), no. 20 1602888.

[16] J. Asenbauer, T. Eisenmann, M. Kuenzel, A. Kazzazi, Z. Chen, and D. Bresser, *The success story of graphite as a lithium-ion anode material–fundamentals, remaining challenges, and recent developments including silicon (oxide) composites*, Sustain. Energy Fuels (2020).

[17] D. Scholl and J. Steckel, *Density Functional Theory: A Practical Introduction*. Wiley, 2009.

[18] W. Kohn, *Nobel lecture: Electronic structure of matter - Wave functions and density functional*, Rev. Mod. Phys. **71** (1999), no. 5 1253–1266.

[19] E. Schrödinger, *An undulatory theory of the mechanics of atoms and molecules*, Phys. Rev. **28** (1926), no. 6 1049–1070.

[20] M. Born and R. Oppenheimer, *Zur quantentheorie der molekeln*, Ann. Phys. **389** (1927), no. 20 457–484.

[21] P. Hohenberg and W. Kohn, *Inhomogeneous electron gas*, Phys. Rev. **136** (1964), no. 3B B864–B871.

[22] W. Kohn and L. J. Sham, *Self-consistent equations including exchange and correlation effects*, Phys. Rev. **140** (1965), no. 4A A1133–A1138.

[23] A. E. Mattsson, *Density functional theory: In pursuit of the divine functional*, Science **298** (2002), no. 5594 759–760.

[24] G. Kresse and J. Furthmüller, *Efficient iterative schemes for ab initio total-energy calculations using a plane-wave basis set*, Phys. Rev. B **54** (1996), no. 16 11169–11186.

[25] G. Kresse and J. Furthmüller, *Efficiency of ab-initio total energy calculations for metals and semiconductors using a plane-wave basis set*, Comput. Mater. Sci. **6** (1996), no. 1 15–50.

[26] A. Van der Ven, B. Puchala, and T. Nagase, *Ti- and Zr-based metal-air batteries*, J. Power Sources **242** (2013) 400–404.

[27] "CASM v0.2.0." https://github.com/prisms-center/CASMcode.

[28] J. C. Thomas and A. Van der Ven, *Finite-temperature properties of strongly anharmonic and mechanically unstable crystal phases from first principles*, Phys. Rev. B **88** (2013), no. 21 214111.

[29] B. Puchala and A. Van der Ven, *Thermodynamics of the Zr-O system from first-principles calculations*, Phys. Rev. B **88** (2013), no. 9 094108.

[30] A. Van der Ven, J. C. Thomas, Q. Xu, and J. Bhattacharya, *Linking the electronic structure of solids to their thermodynamic and kinetic properties*, Math. Comput. Simulat. **80** (2010), no. 7 1393–1410.

[31] N. Metropolis, A. W. Rosenbluth, M. N. Rosenbluth, A. H. Teller, and E. Teller, *Equation of state calculations by fast computing machines*, J. Chem. Phys. **21** (1953), no. 6 1087–1092.

[32] W. K. Hastings, *Monte Carlo sampling methods using Markov chains and their applications*, Biometrika **57** (1970), no. 1 97–109.

[33] A. A. Markov, *An example of statistical investigation of the text Eugene Onegin concerning the connection of samples in chains*, Bull. Imp. Acad. Sci. St. Petersbg. **7** (1913), no. 3 153–162.

[34] J. Vinckevičiūtė, M. D. Radin, and A. Van der Ven, *Stacking-sequence changes and Na ordering in layered intercalation materials*, Chem. Mater. **28** (2016) 8640–8650.

[35] M. H. Han, E. Gonzalo, G. Singh, and T. Rojo, *A comprehensive review of sodium layered oxides: Powerful cathodes for Na-ion batteries*, Energy Environ. Sci. **8** (2015), no. 1 81–102.

[36] D. Kundu, E. Talaie, V. Duffort, and L. F. Nazar, *The emerging chemistry of sodium ion batteries for electrochemical energy storage*, Angew. Chem. Int. Ed. **54** (2015), no. 11 3431–3448.

[37] C. Delmas, C. Fouassier, and P. Hagenmuller, *Stabilite relative des environnements octaedrique et prismatique triangulaire dans les oxydes lamellaires alcalins A_xMO_2 ($x \leq 1$), Mat. Res. Bull.* **11** (1976), no. 4 1483–1488.

[38] J. Rouxel, *Sur un diagramme ionicité-structure pour les composes intercalaires alcalins des sulfures lamellaires, J. Solid State Chem.* **17** (1976), no. 3 223–229.

[39] M. S. Whittingham, *Lithium batteries and cathode materials, Chem. Rev.* **104** (2004), no. 10 4271–4301.

[40] N. Yabuuchi, K. Kubota, M. Dahbi, and S. Komaba, *Research development on sodium-ion batteries, Chem. Rev.* (2014), no. 23 11636–11682.

[41] A. Van der Ven, J. Bhattacharya, and A. A. Belak, *Understanding Li diffusion in Li-intercalation compounds, Acc. Chem. Res.* **46** (2013), no. 5 1216–1225.

[42] S. Miyazaki, S. Kikkawa, and M. Koizumi, *Chemical and electrochemical deintercalations of the layered compounds $LiMO_2$ (M = Cr, Co) and $NaM'O_2$ (M' = Cr, Fe, Co, Ni), Synth. Met.* **6** (1983), no. 2–3 211–217.

[43] I. Saadoune, A. Maazaz, , M. Ménétrier, and C. Delmas, *On the $Na_xNi_{0.6}Co_{0.4}O_2$ system: Physical and electrochemical studies, J. Solid State Chem.* **122** (1996), no. 1 111–117.

[44] S. Komaba, T. Nakayama, A. Ogata, T. Shimizu, C. Takei, S. Takada, A. Hokura, and I. Nakai, *Electrochemically reversible sodium intercalation of layered $NaNi_{0.5}Mn_{0.5}O_2$ and $NaCrO_2$, ECS Trans.* **16** (2009), no. 42 43–55.

[45] X. Ma, H. Chen, and G. Ceder, *Electrochemical properties of monoclinic $NaMnO_2$, J. Electrochem. Soc.* **158** (2011), no. 12 A1307–A1312.

[46] S. Komaba, N. Yabuuchi, T. Nakayama, A. Ogata, T. Ishikawa, and I. Nakai, *Study on the reversible electrode reaction of $Na_{1-x}Ni_{0.5}Mn_{0.5}O_2$ for a rechargeable sodium-ion battery, Inorg. Chem.* **51** (2012), no. 11 6211–6220.

[47] M. Yoncheva, R. Stoyanova, E. Zhecheva, E. Kuzmanova, M. Sendova-Vassileva, D. Nihtianova, D. Carlier, M. Guignard, and C. Delmas, *Structure and reversible lithium intercalation in a new P3-phase: $Na_{2/3}Mn_{1y}Fe_yO_2$ (y = 0, 1/3, 2/3), J. Mater. Chem.* **22** (2012) 23418–23427.

[48] H. Yoshida, N. Yabuuchi, and S. Komaba, *$NaFe_{0.5}Co_{0.5}O_2$ as high energy and power positive electrode for Na-ion batteries, Electrochem. Commun.* **34** (2013) 60–63.

[49] Y.-N. Zhou, J.-J. Ding, K.-W. Nam, X. Yu, S.-M. Bak, E. Hu, J. Liu, J. Bai, H. Li, Z.-W. Fu, and X.-Q. Yang, *Phase transition behavior of $NaCrO_2$ during sodium extraction studied by synchrotron-based X-ray diffraction and absorption spectroscopy*, *J. Mater. Chem. A* **1** (2013), no. 37 11130–11134.

[50] P. Vassilaras, X. Ma, X. Li, and G. Ceder, *Electrochemical properties of monoclinic $NaNiO_2$*, *J. Electrochem. Soc.* **160** (2013), no. 2 A207–A211.

[51] P. Vassilaras, A. J. Toumar, and G. Ceder, *Electrochemical properties of $NaNi_{1/3}Co_{1/3}Fe_{1/3}O_2$ as a cathode material for Na-ion batteries*, *Electrochem. Commun.* **38** (2014) 79–81.

[52] E. Lee, S. Sahgong, C. S. Johnson, and Y. Kim, *Comparative electrochemical sodium insertion/extraction behavior in layered Na_xVS_2 and Na_xTiS_2*, *Electrochim. Acta* **143** (2014) 272–277.

[53] M. H. Han, E. Gonzalo, M. Casas-Cabanas, and T. Rojo, *Structural evolution and electrochemistry of monoclinic $NaNiO_2$ upon the first cycling process*, *J. Power Sources* **258** (2014) 266–271.

[54] J. Ma, S.-H. Bo, L. Wu, Y. Zhu, C. P. Grey, and P. G. Khalifah, *Ordered and disordered polymorphs of $Na(Ni_{2/3}Sb_{1/3})O_2$: Honeycomb-ordered cathodes for Na-ion batteries*, *Chem. Mater.* **27** (2015), no. 7 2387–2399.

[55] D. Wu, X. Li, B. Xu, N. Twu, L. Liu, and G. Ceder, *$NaTiO_2$: A layered anode material for sodium-ion batteries*, *Energy Environ. Sci.* **8** (2015) 195–202.

[56] Y. Qi, Q. Xu, and A. Van der Ven, *Chemically induced crack instability when electrodes fracture*, *J. Electrochem. Soc.* **159** (2012), no. 11 A1838–A1843.

[57] W. H. Woodford, Y.-M. Chiang, and W. C. Carter, *Electrochemical shock in ion-intercalation materials with limited solid-solubility*, *J. Electrochem. Soc.* **160** (2013), no. 8 A1286–A1292.

[58] D. Chang, H. Huo, K. E. Johnston, M. Ménétrier, L. Monconduit, C. P. Grey, and A. Van der Ven, *Elucidating the origins of phase transformation hysteresis during electrochemical cycling of Li-Sb electrodes*, *J. Mater. Chem. A* **3** (2015), no. 37 18928–18943.

[59] S. Kim, X. Ma, S. P. Ong, and G. Ceder, *A comparison of destabilization mechanisms of the layered Na_xMO_2 and Li_xMO_2 compounds upon alkali de-intercalation*, *Phys. Chem. Chem. Phys.* **14** (2012), no. 44 15571–15578.

[60] C. Didier, M. Guignard, M. R. Suchomel, D. Carlier, J. Darriet, and C. Delmas, *Thermally and electrochemically driven topotactical transformations in sodium layered oxides Na_xVO_2*, *Chem. Mater.* **28** (2016), no. 5 1462–1471.

[61] D. Carlier, M. Blangero, M. Ménétrier, M. Pollet, J.-P. Doumerc, and C. Delmas, *Sodium ion mobility in Na_xCoO_2 (0.6 < x < 0.75) cobaltites studied by ^{23}Na MAS NMR*, Inorg. Chem. **48** (2009), no. 15 7018–7025.

[62] X. Li, X. Ma, D. Su, L. Liu, R. Chisnell, S. P. Ong, H. Chen, A. Toumar, J. Idrobo, Y. Lei, J. Bai, F. Wang, J. W. Lynn, Y. S. Lee, and G. Ceder, *Direct visualization of the Jahn-Teller effect coupled to Na ordering in $Na_{5/8}MnO_2$*, Nat. Mater. **13** (2014), no. 6 586–592.

[63] B. G. Silbernagel and M. S. Whittingham, *The physical properties of the Na_xTiS_2 intercalation compounds: A synthetic and NMR study*, Mat. Res. Bull. **11** (1976), no. 1 29–36.

[64] D. A. Winn, J. M. Shemilt, and B. C. H. Steele, *Titanium disulphide: A solid solution electrode for sodium and lithium*, Mat. Res. Bull. **11** (1976), no. 5 559–566.

[65] T. Hibma, *Ordering of the alkali-ions in Na_xTiS_2 and Li_xTiS_2*, Physica B+C **99** (1980), no. 1–4 136–140.

[66] A. Van Der Ven, J. C. Thomas, Q. Xu, B. Swoboda, and D. Morgan, *Nondilute diffusion from first principles: Li diffusion in Li_xTiS_2*, Phys. Rev. B **78** (2008), no. 10 104306.

[67] A. Emly and A. Van der Ven, *Mg intercalation in layered and spinel host crystal structures for Mg batteries*, Inorg. Chem. **54** (2015), no. 9 4394–4402.

[68] J. Kanamori, *Infinite series of ground states of the ising model on the honeycomb lattice*, J. Phys. Soc. Japan **53** (1984), no. 1 250–260.

[69] Y. Wang, Y. Ding, and J. Ni, *Ground-State phase diagram of Na_xCoO_2 : Correlation of Na ordering with CoO_2 stacking sequences*, J. Phys.: Condens. Matter **21** (2009) 035401.

[70] G. Kresse and J. Hafner, *Norm-conserving and ultrasoft pseudopotentials for first-row and transition elements*, J. Phys.: Condens. Matter **6** (1994), no. 40 8245–8257.

[71] G. Kresse and D. Joubert, *From ultrasoft pseudopotentials to the projector augmented-wave method*, Phys. Rev. B **59** (1999), no. 3 1758–1775.

[72] J. Klimeš, D. R. Bowler, and A. Michaelides, *A critical assessment of theoretical methods for finding reaction pathways and transition states of surface processes*, J. Phys.: Condens. Matter **22** (2010), no. 7 074203.

[73] M. Dion, H. Rydberg, E. Schröder, D. C. Langreth, and B. I. Lundqvist, *Van der Waals density functional for general geometries*, Phys. Rev. Lett. **92** (2004), no. 24 246401.

[74] G. Román-Pérez and J. M. Soler, *Efficient implementation of a van der Waals density functional: Application to double-wall carbon nanotubes*, Phys. Rev. Lett. **103** (2009), no. 9 096102.

[75] J. Klimeš, D. R. Bowler, and A. Michaelides, *Van der Waals density functionals applied to solids*, Phys. Rev. B **83** (2011), no. 19 195131.

[76] G. Ceder, *A derivation of the Ising model for the computation of phase diagrams*, Comput. Mater. Sci. **1** (1993) 144–150.

[77] J. M. Sanchez, F. Ducastelle, and D. Gratias, *Generalized cluster description of multicomponent systems*, Physica **128A** (1984), no. 1–2 334–350.

[78] D. De Fontaine, *Cluster approach to order-disorder transformations in alloys*, Solid State Phys. **47** (1994) 33–176.

[79] G. L. W. Hart, V. Blum, M. J. Walorski, and A. Zunger, *Evolutionary approach for determining first-principles hamiltonians*, Nat. Mater. **4** (2005), no. 5 391–394.

[80] A. S. Dalton, A. A. Belak, and A. Van der Ven, *Thermodynamics of lithium in $TiO_2(B)$ from first principles*, Chem. Mater. **24** (2012), no. 9 1568–1574.

[81] J. Rouxel, M. Danot, and J. Bichon, *Les composés intercalaires $Na_x TiS_2$. Étude structurale générale des phases $Na_x TiS_2$ et $K_x TiS_2$*, Bull. Soc. Chim. Fr. **53** (1971) 3930–3935.

[82] A. J. Toumar, S. P. Ong, W. D. Richards, S. Dacek, and G. Ceder, *Vacancy ordering in O3-type layered metal oxide sodium-ion battery cathodes*, Phys. Rev. Applied **4** (2015) 064002.

[83] J. N. Reimers and J. R. Dahn, *Electrochemical and insitu X-ray diffraction studies of lithium intercalation in $Li_x CoO_2$*, J. Electrochem. Soc. **139** (1992), no. 8 2091–2097.

[84] E. Lee, W. C. Lee, N. M. Asl, D. Kim, M. Slater, C. Johnson, and Y. Kim, *Reversible $NaVS_2$ (de)intercalation cathode for Na-ion batteries*, ECS Electrochem. Lett. **1** (2012), no. 5 A71–A73.

[85] M. D. Radin and A. Van der Ven, *The stability of prismatic and octahedral coordination in layered oxides and sulfides intercalated with alkali and alkaline-earth metals*, Chem. Mater. **28** (2016), no. 21 7898–7904.

[86] H. Gabrisch, R. Yazami, and B. Fultz, *The Character of dislocations in LiCoO$_2$*, *Electrochem. Solid-State Lett.* **5** (2002), no. 6 A111–A114.

[87] S. Komaba, W. Murata, T. Ishikawa, N. Yabuuchi, T. Ozeki, T. Nakayama, A. Ogata, K. Gotoh, and K. Fujiwara, *Electrochemical Na insertion and solid electrolyte interphase for hard-carbon electrodes and application to Na-ion batteries*, *Adv. Funct. Mater.* **21** (2011), no. 20 3859–3867.

[88] R. C. Asher, *A lamellar compound of sodium and graphite*, *J. Inorg. Nucl. Chem.* **10** (1959), no. 3–4 238–249.

[89] D. P. DiVincenzo and E. J. Mele, *Cohesion and structure in stage-1 graphite intercalation compounds*, *Phys. Rev. B* **32** (1985), no. 4 2538–2553.

[90] R. Alcántara, J. M. Jiménez-Mateos, P. Lavela, and J. L. Tirado, *Carbon black: A promising electrode material for sodium-ion batteries*, *Electrochem. Commun.* **3** (2001), no. 11 639–642.

[91] P. Hagenmuller, A. Lecerf, and M. Onillon, *Chimie minérale - Un nouveau composé oxygéné du titane trivalent: NaTiO$_2$*, *Cr. Hebd. Acad. Sci.* **255** (1962), no. 5 928–930.

[92] A. Maazaz, C. Delmas, and P. Hagenmuller, *A study of the Na$_x$TiO$_2$ system by electrochemical deintercalation*, *J. Inclusion Phenom.* **1** (1983), no. 1 45–51.

[93] S. Pérez-Villar, E. Castillo-Martínez, J. M. López del Amo, T. Rojo, and M. Armand, *Electrochemical performance of novel O3 layered Al,Mg doped titanates as anode materials for Na-ion batteries*, *Mat. Res. Bull.* **94** (2017) 199–207.

[94] J. L. Kaufman and A. Van Der Ven, *Na$_x$CoO$_2$ phase stability and hierarchical orderings in the O3/P3 structure family*, *Phys. Rev. Mater.* **3** (2019), no. 1 015402.

[95] S. J. Clarke, A. J. Fowkes, A. Harrison, R. M. Ibberson, and M. J. Rosseinsky, *Synthesis, structure, and magnetic properties of NaTiO$_2$*, *Chem. Mater.* **10** (1998), no. 1 372–384.

[96] M. Dhariwal, T. Maitra, I. Singh, S. Koley, and A. Taraphder, *Orbital order in NaTiO$_2$: A first principles study*, *Solid State Commun.* **152** (2012), no. 20 1912–1916.

[97] S.-D. Ouyang, Y.-M. Quan, D.-Y. Liu, and L.-J. Zou, *A comparative investigation on the JT effect in triangular compounds of NaMnO$_2$, NaNiO$_2$ and NaTiO$_2$*, *Chin. Phys. Lett.* **28** (2011), no. 6 067102.

[98] A. Vasileiadis and M. Wagemaker, *Thermodynamics and kinetics of Na-ion insertion into hollandite-TiO_2 and O3-layered $NaTiO_2$: An unexpected link between two promising anode materials for Na-ion batteries*, Chem. Mater. **29** (2017), no. 3 1076–1088.

[99] A. Jain, S. P. Ong, G. Hautier, W. Chen, W. D. Richards, S. Dacek, S. Cholia, D. Gunter, D. Skinner, G. Ceder, and K. A. Persson, *The Materials Project: A materials genome approach to accelerating materials innovation*, APL Mater. **1** (2013), no. 1 011002.

[100] J. Akimoto and H. Takei, *Synthesis and crystal structure of $NaTi_2O_4$: A new mixed-valence sodium titanate*, J. Solid State Chem. **79** (1989), no. 2 212–217.

[101] M. Y. Toriyama, J. L. Kaufman, and A. Van Der Ven, *Potassium ordering and structural phase stability in layered K_xCoO_2*, ACS Appl. Energy Mater. **2** (2019), no. 4 2629–2636.

[102] C. Didier, M. Guignard, C. Denage, O. Szajwaj, S. Ito, I. Saadoune, J. Darriet, and C. Delmas, *Electrochemical Na-deintercalation from $NaVO_2$*, Electrochem. Solid-State Lett. **14** (2011), no. 5 A75–A78.

[103] S. Komaba, C. Takei, T. Nakayama, A. Ogata, and N. Yabuuchi, *Electrochemical intercalation activity of layered $NaCrO_2$ vs. $LiCrO_2$*, Electrochem. Commun. **12** (2010), no. 3 355–358.

[104] N. Yabuuchi, H. Yoshida, and S. Komaba, *Crystal structures and electrode performance of alpha-$NaFeO_2$ for rechargeable sodium batteries*, Electrochemistry **80** (2012), no. 10 716–719.

[105] S. Kikkawa, S. Miyazaki, and M. Koizumi, *Deintercalated $NaCoO_2$ and $LiCoO_2$*, J. Solid State Chem. **62** (1986), no. 1 35–39.

[106] J. Vinckevičiūtė, M. D. Radin, N. V. Faenza, G. G. Amatucci, and A. Van Der Ven, *Fundamental insights about interlayer cation migration in Li-ion electrodes at high states of charge*, J. Mater. Chem. A **7** (2019), no. 19 11996–12007.

[107] K. Mizushima, P. C. Jones, P. J. Wiseman, and J. B. Goodenough, *Li_xCoO_2 ($0 < x \leq 1$): A new cathode material for batteries of high energy density*, Mat. Res. Bull. **15** (1980), no. 6 783–789.

[108] M. Thackeray, C. Wolverton, and E. Isaacs, *Electrical energy storage for transportation–approaching the limits of, and going beyond, lithium-ion batteries*, Energy Environ. Sci. **5** (2012), no. 7 7854–7863.

[109] N. Nitta, F. Wu, J. T. Lee, and G. Yushin, *Li-ion battery materials: Present and future*, Mater. Today **18** (2015), no. 5 252–264.

[110] F. Schipper, E. M. Erickson, C. Erk, J.-Y. Shin, F. F. Chesneau, and D. Aurbach, *Review–Recent advances and remaining challenges for lithium ion battery cathodes*, J. Electrochem. Soc. **164** (2017), no. 1 A6220–A6228.

[111] S. Hy, H. Liu, M. Zhang, D. Qian, B.-J. Hwang, and Y. S. Meng, *Performance and design considerations for lithium excess layered oxide positive electrode materials for lithium ion batteries*, Energy Environ. Sci. **9** (2016), no. 6 1931–1954.

[112] N. Tapia-Ruiz, W. M. Dose, N. Sharma, H. Chen, J. Heath, J. W. Somerville, U. Maitra, M. S. Islam, and P. G. Bruce, *High voltage structural evolution and enhanced Na-ion diffusion in P2-$Na_{2/3}Ni_{1/3x}Mg_xMn_{2/3}O_2$ ($0 \leq x \leq 0.2$) cathodes from diffraction, electrochemical and abinitio studies*, Energy Environ. Sci. **11** (2018), no. 6 1470–1479.

[113] H. Liu, H. Liu, I. D. Seymour, N. Chernova, K. M. Wiaderek, N. M. Trease, S. Hy, Y. Chen, K. An, M. Zhang, O. J. Borkiewicz, S. H. Lapidus, B. Qiu, Y. Xia, Z. Liu, P. J. Chupas, K. W. Chapman, M. S. Whittingham, C. P. Grey, and Y. S. Meng, *Identifying the chemical and structural irreversibility in $LiNi_{0.8}Co_{0.15}Al_{0.05}O_2$ âĂŞ a model compound for classical layered intercalation*, J. Mater. Chem. A **6** (2018), no. 9 4189–4198.

[114] T. Ohzuku, A. Ueda, and M. Kouguchi, *Synthesis and characterization of $LiAl_{14}Ni_{34}O_2$ ($R\bar{3}m$) for lithium-ion (shuttlecock) batteries*, J. Electrochem. Soc. **142** (1995), no. 12 4033–4039.

[115] T. Ohzuku, T. Yanagawa, M. Kouguchi, and A. Ueda, *Innovative insertion material of $LiAl_{1/4}Ni_{3/4}O_2$ ($R\bar{3}m$) for lithium-ion (shuttlecock) batteries*, J. Power Sources **68** (1997), no. 1 131–134.

[116] S. Madhavi, G. V. Subba Rao, B. V. R. Chowdari, and S. F. Y. Li, *Effect of aluminium doping on cathodic behaviour of $LiNi_{0.7}Co_{0.3}O_2$*, J. Power Sources **93** (2001), no. 1–2 156–162.

[117] C. Vogler, B. Löffler, W. Weirather, M. Wohlfahrt-Mehrens, and J. Garche, *Doped lithium nickel cobalt mixed oxides for the positive electrode in lithium ion batteries*, Ionics **8** (2002), no. 1-2 92–99.

[118] C. Delmas, M. Ménétrier, L. Croguennec, I. Saadoune, A. Rougier, C. Pouillerie, G. Prado, M. Grüne, and L. Fournès, *An overview of the $Li(Ni,M)O_2$ systems: syntheses, structures and properties*, Electrochim. Acta **45** (1999), no. 1–2 243–253.

[119] C. Pouillerie, L. Croguennec, P. Biensan, P. Willmann, and C. Delmas, *Synthesis and characterization of new $LiNi_{1y}Mg_yO_2$ positive electrode materials for lithium-ion batteries*, J. Electrochem. Soc. **147** (2000), no. 6 2061–2069.

[120] C.-C. Chang, J. Y. Kim, and P. N. Kumta, *Synthesis and electrochemical characterization of divalent cation-incorporated lithium nickel oxide*, J. Electrochem. Soc. **147** (2000), no. 5 1722–1729.

[121] T. Sasaki, V. Godbole, Y. Takeuchi, Y. Ukyo, and P. Novák, *Morphological and structural changes of Mg-substituted Li(Ni,Co,Al)O$_2$ during overcharge reaction*, J. Electrochem. Soc. **158** (2011), no. 11 A1214–A1219.

[122] G. G. Amatucci, J. M. Tarascon, and L. C. Klein, *CoO$_2$, the end member of the Li$_2$CoO$_2$ solid solution*, J. Electrochem. Soc. **143** (1996), no. 3 1114–1123.

[123] A. Van der Ven, M. K. Aydinol, and G. Ceder, *First-principles evidence for stage ordering in Li$_x$CoO$_2$*, J. Electrochem. Soc. **145** (1998), no. 6 2149–2155.

[124] N. V. Faenza, N. Pereira, D. M. Halat, J. Vinckeviciute, L. Bruce, M. D. Radin, P. Mukherjee, F. Badway, A. Halajko, F. Cosanday, C. P. Grey, A. Van der Ven, and G. G. Amatucci, *The phase evolution and degradation modes of R$\bar{3}$m Li$_x$Ni$_{1-y-z}$Co$_y$Al$_z$O$_2$ electrodes cycled near complete delithiation*, Chem. Mater. **30** (2018), no. 21 7545–7574.

[125] H. Tukamoto and A. R. West, *Electronic conductivity of LiCoO$_2$ and its enhancement by magnesium doping*, J. Electrochem. Soc. **144** (1997), no. 9 3164–3168.

[126] C. P. Grey, W.-S. Yoon, J. Reed, and G. Ceder, *Electrochemical activity of Li in the transition-metal sites of O3 Li[Li$_{(12x)/3}$Mn$_{(2x)/3}$Ni$_x$]O$_2$*, Electrochem. Solid-State Lett. **7** (2004), no. 9 A290–A293.

[127] M. S. Islam, D. J. Driscoll, C. A. Fisher, and P. R. Slater, *Atomic-scale investigation of defects, dopants, and lithium transport in the LiFePO$_4$ olivine-type battery material*, Chem. Mater. **17** (2005), no. 20 5085–5092.

[128] R. Amin and J. Maier, *Effect of annealing on transport properties of LiFePO$_4$: Towards a defect chemical model*, Solid State Ion. **178** (2008), no. 35–36 1831–1836.

[129] J. Chen and J. Graetz, *Study of antisite defects in hydrothermally prepared LiFePO$_4$ by in situ X-ray diffraction*, ACS Appl. Mater. Inter. **3** (2011), no. 5 1380–1384.

[130] R. Malik, D. Burch, M. Bazant, and G. Ceder, *Particle size dependence of the ionic diffusivity*, Nano Lett. **10** (2010), no. 10 4123–4127.

[131] M. S. Islam and C. A. J. Fisher, *Lithium and sodium battery cathode materials: computational insights into voltage, diffusion and nanostructural properties*, Chem. Soc. Rev. **43** (2014), no. 1 185–204.

[132] Z. Rong, R. Malik, P. Canepa, G. Sai Gautam, M. Liu, A. Jain, K. Persson, and G. Ceder, *Materials design rules for multivalent ion mobility in intercalation structures*, Chem. Mater. **27** (2015), no. 17 6016–6021.

[133] J. Bhattacharya and A. Van der Ven, *First-principles study of competing mechanisms of nondilute Li diffusion in spinel $Li_x TiS_2$*, Phys. Rev. B **83** (2011), no. 14 144302.

[134] A. Van der Ven and G. Ceder, *Ordering in $Li_x(Ni_{0.5}Mn_{0.5})O_2$ and its relation to charge capacity and electrochemical behavior in rechargeable lithium batteries*, Electrochem. Commun. **6** (2004), no. 10 1045–1050.

[135] J. Reed, G. Ceder, and A. Van Der Ven, *Layered-to-spinel phase transition in $Li_x MnO_2$*, Electrochem. Solid-State Lett. **4** (2001), no. 6 A78–A81.

[136] J. Reed and G. Ceder, *Role of electronic structure in the susceptibility of metastable transition-metal oxide structures to transformation*, Chem. Rev. **104** (2004), no. 10 4513–4534.

[137] D.-H. Seo, J. Lee, A. Urban, R. Malik, S. Kang, and G. Ceder, *The structural and chemical origin of the oxygen redox activity in layered and cation-disordered Li-excess cathode materials*, Nat. Chem. **8** (2016), no. 7 692–697.

[138] G. Assat and J.-M. Tarascon, *Fundamental understanding and practical challenges of anionic redox activity in Li-ion batteries*, Nat. Energy **3** (2018), no. 5 373–386.

[139] C. Delmas, J. Pérès, A. Rougier, A. Demourgues, F. Weill, A. Chadwick, M. Broussely, F. Perton, P. Biensan, and P. Willmann, *On the behavior of the $Li_x NiO_2$ system: an electrochemical and structural overview*, J. Power Sources **68** (1997), no. 1 120–125.

[140] V. I. Anisimov, F. Aryasetiawan, and A. I. Lichtenstein, *First-principles calculations of the electronic structure and spectra of strongly correlated systems: the LDA + U method*, J. Phys.: Condens. Matter **9** (1997), no. 4 767–808.

[141] S. L. Dudarev, G. A. Botton, S. Y. Savrasov, C. J. Humphreys, and A. P. Sutton, *Electron-energy-loss spectra and the structural stability of nickel oxide: An LSDA+U study*, Phys. Rev. B **57** (1998), no. 3 1505–1509.

[142] F. Zhou, M. Cococcioni, C. A. Marianetti, D. Morgan, and G. Ceder, *First-principles prediction of redox potentials in transition-metal compounds with LDA+U*, Phys. Rev. B **70** (2004), no. 23 235121.

[143] Y. S. Meng, Y. Hinuma, and G. Ceder, *An investigation of the sodium patterning in $Na_x CoO_2$ ($0.5 \leq x \leq 1$) by density functional theory methods*, J. Chem. Phys. **128** (2008), no. 10 104708.

[144] E. B. Isaacs and C. A. Marianetti, *Compositional phase stability of strongly correlated electron materials within DFT+U*, *Phys. Rev. B* **95** (2017), no. 4 045141.

[145] H. Chen and M. S. Islam, *Lithium extraction mechanism in Li-rich Li_2MnO_3 involving oxygen hole formation and dimerization*, *Chem. Mater.* **28** (2016), no. 18 6656–6663.

[146] K. Luo, M. R. Roberts, R. Hao, N. Guerrini, D. M. Pickup, Y.-S. Liu, K. Edström, J. Guo, A. V. Chadwick, L. C. Duda, and P. G. Bruce, *Charge-compensation in 3d-transition-metal-oxide intercalation cathodes through the generation of localized electron holes on oxygen*, *Nat. Chem.* **8** (2016), no. 7 684–691.

[147] Z. Zhuo, C. D. Pemmaraju, J. Vinson, C. Jia, B. Moritz, I. Lee, S. Sallies, Q. Li, J. Wu, K. Dai, Y. D. Chuang, Z. Hussain, F. Pan, T. P. Devereaux, and W. Yang, *Spectroscopic signature of oxidized oxygen states in peroxides*, *J. Phys. Chem. Lett.* **9** (2018), no. 21 6378–6384.